



PONTIFICIA UNIVERSIDAD CATOLICA DE CHILE
SCHOOL OF ENGINEERING

SEISMIC MICROZONING OF ARICA AND IQUIQUE, CHILE

ALIX PAULINA BECERRA TÉLLEZ

Thesis submitted to the Office of Research and Graduate Studies
in partial fulfillment of the requirements for the degree of
Master of Science in Engineering

Advisor:

ESTEBAN PATRICIO SÁEZ ROBERT

Santiago de Chile, May, 2014

© MMXIV, ALIX PAULINA BECERRA TÉLLEZ



PONTIFICIA UNIVERSIDAD CATOLICA DE CHILE
SCHOOL OF ENGINEERING

SEISMIC MICROZONING OF ARICA AND IQUIQUE, CHILE

ALIX PAULINA BECERRA TÉLLEZ

Members of the Committee:

ESTEBAN PATRICIO SÁEZ ROBERT

GONZALO ALEJANDRO YAÑEZ CARRIZO

FELIPE ORLANDO LEYTON FLORES

DIEGO JAVIER CELENTANO

Thesis submitted to the Office of Research and Graduate Studies
in partial fulfillment of the requirements for the degree of
Master of Science in Engineering

Santiago de Chile, May, 2014

© MMXIV, ALIX PAULINA BECERRA TÉLLEZ

*'The noblest pleasure is the art of
understanding' - Leonardo da Vinci*

ACKNOWLEDGEMENTS

I do not have enough pages to thank everyone I would like to. You have all been crucial in this process and I will never forget your continuous support. Foremost, I would like to express my sincere gratitude to my advisor Professor Esteban Sáez for his patience, motivation, enthusiasm and immense knowledge. His guidance was fundamental in all the time of research and writing of this thesis.

I want to thank the members of my thesis committee: Professor Felipe Leyton, for his insightful comments and significant contribution to my research. To Professors Gonzalo Yáñez and Diego Celentano, for their encouragement, their help by viewing my research from different perspectives and guiding me through my academic development.

Special thanks to Antonio, for rescuing me when I was stuck for days in the same problems, for his patience and knowledge. Also many thanks to everyone in the DIEG office and the 'geopeople' for cheering up my working days, encouraging me and giving useful insights for my research.

My gratitude to everyone who helped during the fieldwork period of this research and to the students from the Diego Portales University who collaborated with data for this project. Also thanks to all the teachers that have contributed to my academic formation and to the administrative personnel in the DIEG department.

Thanks to my beloved friends for supporting me in this journey, for keeping our beautiful friendship and for this amazing bond we have developed throughout the years.

I would like to thank my family for their love and unconditional support in this and every process, I would not be writing any of this if it were not for them. I love you and there are no words to express how grateful I am.

Finally, I would like to thank the Chilean National Commission For Scientific and Technological Research (CONICYT) for funding this research under FONDEF + ANDES award number D10I1027 and the National Office of Emergency (ONEMI) for contributing with the records of the A01-2014 earthquake.

GENERAL INDEX

ACKNOWLEDGEMENTS	IV
LIST OF FIGURES	VIII
LIST OF TABLES	XIV
RESUMEN	XV
ABSTRACT	XVI
1. INTRODUCTION	1
2. GEOLOGICAL SETTING	4
2.1. Geomorphology of Arica and Iquique	4
2.1.1. Arica	4
2.1.2. Iquique and Alto Hospicio	7
3. SEISMIC CHARACTERIZATION OF A SITE	8
3.1. Seismic waves	8
3.2. F-K method	10
3.2.1. Passive source approach	10
3.2.2. Active source approach	12
3.3. RoadSide Multichannel analysis of surface waves	14
3.3.1. Spatial Autocorrelation Method	15
3.3.2. H/V Spectral ratio	18
3.4. Vs profile and HVSR computation	21
3.5. Combination of dispersion curves and surface wave velocity profile inversion	22
3.6. Limitations of surface wave methods	24
4. DATA ACQUISITION	27
4.1. Geophysical surveys	27

4.2. Boreholes	29
5. MICROZONING	33
5.1. Arica	33
5.1.1. El Morro Hill	35
5.1.2. San Jose alluvial fan	36
5.1.3. El Chuño Hill	37
5.1.4. Northern Side	38
5.1.5. Urban Northern Limit	39
5.1.6. Microzoning Definition	40
5.2. Iquique	43
5.2.1. ZOFRI Area	46
5.2.2. Town Center	47
5.2.3. Dragon Hill	49
5.2.4. Southern limit	49
5.2.5. Port of Iquique	51
5.2.6. Alto Hospicio	51
5.2.7. Microzoning Definition	53
5.3. Microzoning Discussion	54
5.3.1. Comparison to A01-2014 earthquake	57
5.4. Discussion	60
6. 3D MODELLING OF SITE AMPLIFICATION. THE CASE OF ARICA	61
6.1. Introduction to Spectral element method	61
6.1.1. Model problem	62
6.1.2. Weak form	63
6.1.3. Definition of the mesh	64
6.1.4. Time integration scheme	65
6.1.5. Recent approaches for non conforming domains	68
6.2. Description of zone of study	68

6.3. Homogeneous soil mesh	72
6.4. Source and Time scheme definition	73
6.5. Results	75
6.6. Validation of the model	75
6.7. Evaluation of 3D effects	76
7. CONCLUSIONS	79
7.1. Future work	80
Bibliography	81
8. APPENDIX A	87
9. APPENDIX B	91

LIST OF FIGURES

1.1. (a) Seismic context of Northern Chile. To the left, historical records show the seismic gap of 136 years that had affected this zone between 1877 and 2014. The image to the right illustrates the seismic coupling of over 75 % in the orange area and a comparison between the moment deficit accumulated since 1877 and the seismic moment released for the April 1 st 2014 event. The rupture area of the earthquake is marked in a blue line, obtained from the USGS Earthquake Data Report. Modified from Scholz and Campos (2012) and Chlieh et al. (2011).	2
2.1. Major geographical units surrounding Arica and Iquique. The Chilean Coastal Range borders both cities towards the coast. To the east, the Intermediate Depression is the valley between the Coastal Range and the Andes Mountains that can be found further to the east. Past the Andes, the Andean Plateau is located in Bolivian territory. Modified from García et al. (2004).	5
2.2. Geology maps of (a) Arica and (c) Iquique. The black dotted lines indicate urban extensions, while the red ones denote fault lines. Simplified from Marquardt et al. (2008), Maldonado (2014).	6
3.1. Types of seismic waves (Sauter, 1989).	9
3.2. Plane wave front crossing a seismic array (Ohrnberger et al., 2012).	10
3.3. Combination of the record of each geophone to find the array response (Ohrnberger et al., 2012).	11
3.4. Example of an f-k analysis over one time window (left) at a frequency of 15 Hz for the computation of the dispersion curve (right) (Humire, 2013).	12

3.5. Response function for a circular array with a radius of 9.56 meters. The first image (a) shows the response function with a global peak in the center, and other local peaks. Image (b) shows response functions for different azimuths (wave front incidence direction), the central lobe denotes the capacity of the array to differentiate two wave fronts with similar wavenumbers.	12
3.6. Vertical motion of a typical record used for the active F-K approach, in this case the shot is located at 10 meters from receiver R012.	13
3.7. Dispersion graphs for an active source at different shot locations. The pink area represents the concentration of maximum energy of the array, and the black line is the final dispersion curve selected from stacking the previous 5 graphs.	14
3.8. Different types of possible wave propagation employing a 1-D linear receiver array parallel to a road (Park and Miller, 2008).	16
3.9. Typical dispersion curve obtained through the RoadSide MASW analysis. In this case it was possible to extract information between 5 and 15 Hz. The theoretical exploration limits are displayed in black lines.	17
3.10. Rings of paired distances between geophones for a circular array with a radius of 9.56 meters.	17
3.11. Record of the velocities in the 3 components registered by a Tromino, North-South, East-West, and Vertical motion.	20
3.12. HVSR results for one site. The first image (bottom) shows the results of the averaged standard deviation of the H/V Spectral Ratio in each window, indicating the amplitude that the associated fundamental frequency reaches in its peak. The second image (center) is the statistic median of the spectrum, grouping the windows that have a similar frequency and eliminating those that are too far away from the average. Finally, the third image (top) indicates frequency associated to the previous 2 graphs by time window, in other words, it is an indicator of the stability of the result.	21
3.13. Flowchart of the procedure followed to obtain a final S wave velocity profile. . .	22

3.14. Combination of dispersion curves for one site. From left to right: in green the curve obtained from the autocorrelation coefficients, then in orange the dispersion curve obtained through the MASW RoadSide method implemented in SeisImager. In the middle the dispersion curve of a passive circular F-K method, and to the right, the dispersion curve obtained from an active linear test, analysed also through the F-K methodology.	24
3.15. Inversion process carried out from the experimental data, the figures show all the possible combinations of proposed dispersion curves (a) and shear wave velocity profile (b), based on the adjustment value to the previously obtained dispersion curve. Usually a misfit that is considered acceptable should be below 0.2.	25
4.1. Geometry of the seismic arrays for its maximum size, circles (left) have a maximum radius of 9.56 m, and lines (right) can be as long as 55 meters.	28
4.2. Spatial distribution of the explored sites in Arica, Iquique and Alto Hospicio. HVSR and Vs surveys are shown in yellow circles, while drilled boreholes are shown in red stars.	28
4.3. (a) Location of boreholes drilled in Arica. (b) to (d) Boreholes log.	30
4.4. (a) Location of boreholes drilled in Iquique. (b) to (e) Boreholes log. Boreholes IQ_S_1 to IQ_S_3 were drilled during this investigation, whereas IQ_S_4 was provided by a local consultant.	31
4.5. Comparison of shear wave velocity profiles between available downhole tests and SWM surveys in Iquique.	32
4.6. Comparison of shear wave velocity profiles between available downhole tests and SWM surveys in Arica.	32
5.1. Map with the computed F_0 through HVSR technique in Arica, the size of the circles represents the amplitude of the result, and the colorbar denotes the fundamental frequencies of each site.	34
5.2. Map with the computed V_s^{30} in each site of study in Arica. The intervals are inspired on the current Chilean seismic guidelines.	35

5.3. Values of V_s^{30} and F_0 near El Morro. Typical results of V_s profiles and HVSR computations are shown for the area marked in orange.	36
5.4. Values of V_s^{30} and F_0 located near the alluvial fan of the San Jose river. Typical results of V_s profiles and HVSR computations are shown for the area marked in orange.	37
5.5. Values of V_s^{30} and F_0 in the outskirts of the El Chuño Hill. Typical results of V_s profiles and HVSR computations are shown for the area marked in orange.	38
5.6. Values of V_s^{30} and F_0 in the northern suburbs of Arica. Typical results of V_s profiles and HVSR computations are shown for the area marked in orange.	39
5.7. Values of V_s^{30} and F_0 towards the northern limit of Arica. Typical results of V_s profiles and HVSR computations are shown for the area marked in orange.	40
5.8. Preliminary microzonation of Arica defined by Monetta (2013).	41
5.9. Final seismic microzoning of Arica. The colors indicate the susceptibility of soil amplification in the area, from green denoting no or low amplification, yellow is medium site-effects and red indicating high expected site effects. The blue represents artificial landfills, where a more detailed study should be performed.	43
5.10. Map with the computed F_0 through HVSR technique in Iquique, the size of the circles represents the amplitude of the result, and the colorbar denotes the fundamental frequencies of each site.	45
5.11. Map with the computed V_s^{30} in each site of study in Iquique. The classification is based on the DS 61.	46
5.12. Values of V_s^{30} and F_0 towards the northern limit of Iquique (ZOFRI). The dotted blue line denotes the ZOFRI fault, while the orange line marks the referenced area of study	47
5.13. Values of V_s^{30} and F_0 in the town center of Iquique. Typical results are shown for the red marked area and the orange marked area. The dotted blue lines represent the existing faults, in this case, the Cavanca fault.	48
5.14. Values of V_s^{30} and F_0 in the southern residential area of Iquique, near the Dragon hill.	50

5.15. Map with the computed results in the southern limit of Iquique.	51
5.16. Map with the computed results in the port of Iquique.	52
5.17. Map with the computed results in Alto Hospicio.	53
5.18. Preliminary microzonation performed by Podestá (2013).	54
5.19. Proposed microzonation of Iquique. The colors indicate the susceptibility of motion amplification in the area, from green denoting no or low amplification, yellow is medium expected site effect and red indicating high susceptibility to site effects. The peak ground accelerations (PGA) of the A01-2014 event are also displayed. .	55
5.20. Acceleration records for the 01A-2014 Earthquake.	58
5.21. Acceleration spectra in stations T05A and T06A for the 01A-2014 Earthquake. .	59
5.22. Acceleration spectra in stations T03A and T08A for the 01A-2014 Earthquake. The text on the Figures denote the HVSR results for the closest site.	60
6.1. Finite soil model with total volume Ω . The free surface is denoted by Γ_{ff} , and the boundaries are Γ_D and Γ_{NR} . The unit outward normal to all boundaries is denoted by \underline{n}	62
6.2. Control nodes for one element for a polynomial degree of 3. (a) shows the 2-D case with 9 control points while the 3-D element (b) has a total of 27 control points, the empty squares indicate the nodes that locate at the middle sides of the element's faces and the empty triangle lies at the center of the element (Komatitsch et al., 1999).	66
6.3. Lagrange interpolants through the LGL control points for $N = 2$ (left) and $N = 6$ (right). All Lagrange polynomials are equal to 1 or 0 at each point (Van de Vosse and Minev, 1996).	66
6.4. Selection of zone of study marked in blue. The sites where shear wave velocity profiles and predominant frequencies have been acquired are marked in black dots ("monitors"). The boreholes are displayed with yellow stars.	69
6.5. Topography of Arica and detail of study site.	70
6.6. Vs profile for one site, the figure shows the extension of the profile until the estimated depth to bedrock.	71

6.7. 3-D shear wave velocity model for the site of study in Figure 6.4.	72
6.8. Homogeneous soil mesh for the proposed problem. Note that the North-South and East-West directions coincide with the axis Y and X, respectively.	74
6.9. Ricker wavelet with $f_0 = 3.5Hz$ and $t_0 = 0.4s$	75
6.10. Comparison of transfer functions between a 3D horizontally layered model and an equivalent 1D profile computed in time domain.	76
6.11. Comparison between displacements for ARI40 control point (Figure 6.5) between surface and bedrock.	77
6.12. Transfer functions for 2 control sites using the 3D Homogeneous soil model. (a) ARI08 control point (west); (b) ARI28 control point (east).	78

LIST OF TABLES

3.1. Number of analysis carried out in each city.	22
5.1. Detailing of the zones delimited by Figure 5.9.	44
5.2. Detailing of the zones delimited by Figure 5.19.	56
6.1. Elastic properties of each material. ρ denotes the density of the material, λ and μ are the Lamé parameters, and γ is the damping ratio.	73
8.1. Results of V_s^{30} and HVSR in Arica and their corresponding coordinates. The coordinate system is UTM WGS84.	87
8.2. Results of V_s^{30} and HVSR in Arica and their corresponding coordinates. The coordinate system is UTM WGS84.	88
8.3. Results of V_s^{30} and HVSR in Iquique and their corresponding coordinates. The coordinate system is UTM WGS84.	89
8.4. Results of V_s^{30} and HVSR in Iquique and their corresponding coordinates. The coordinate system is UTM WGS84.	90

RESUMEN

La subducción entre las placas de Nazca y Sudamericana sitúa a Chile como uno de los países con mayor actividad sísmica del mundo. El acoplamiento sismogénico y el gap sísmico de 136 años anunciaban el inminente movimiento sísmico que podría afectar al norte del país. De este escenario nace la necesidad de evaluar zonas de las ciudades del extremo norte donde el movimiento se podría ver más o menos amplificado según las condiciones locales del suelo. Esta investigación se concentra en el análisis geofísico y dinámico de los suelos de fundación de las ciudades de Arica e Iquique.

En ambas ciudades, 102 sitios fueron seleccionados para realizar ensayos geofísicos basados en ondas superficiales. De la inversión de registros de vibraciones ambientales se derivó el perfil de velocidad de onda S y la frecuencia predominante de cada sitio. Adicionalmente, siete sondajes fueron ejecutados para complementar los datos adquiridos. Combinando los datos disponibles se generó una microzonificación sísmica para cada ciudad. Los resultados demuestran la consistencia de este tipo de ensayo geofísico con la geología superficial. La información determina que las zonas más propensas a efectos de amplificación sísmica son el norte de Arica, el sureste de Iquique, el límite norte de Iquique (en la zona ZOFRI), y el relleno artificial del puerto de Iquique.

Adicionalmente, se seleccionó una zona de estudio al norte de Arica para construir un modelo 3D de propagación de ondas. Las propiedades del modelo fueron derivadas de la interpolación de los perfiles de velocidad S en conjunto con la técnica de Nakamura para obtener la profundidad al basamento en los puntos de control. Con esta información se simuló el movimiento del suelo por medio del método de elementos espectrales. La simulación de una onda tipo Ricker muestra que el modelo tridimensional es capaz de evaluar la variabilidad espacial de las propiedades del suelo, la profundidad de la roca y la topografía. Los resultados se comparan con la metodología 1D tradicional.

Palabras Claves: Microzonificación sísmica, Métodos de ondas superficiales, Arica, Iquique, elementos espectrales.

ABSTRACT

The subduction of the Nazca plate under the Southamerican plate places Chile as a one of the most seismic countries in the world. The large seismogenic coupling and the 136 years seismic gap predict the eventual seismic activity affecting the north of the country. This sismotectonic framework urges the assessment of earthquake hazards in urban domains. In this context, seismic microzoning emerges as a tool to identify areas that are more susceptible to site effects. The following research focused on a geophysical-based analysis of the soils in Arica and Iquique, both principal cities in northern Chile.

In both cities, 102 sites were chosen to perform geophysical surveys based on surface wave methods (SWM). By inverting the measurements, local shear wave velocity profiles and predominant frequencies were derived in each site, in order to determine the site's properties. Besides geophysical surveys, seven boreholes were available to further complement the gathered data. With the results, the cities were subdivided into zones with similar properties in terms of the average shear wave velocity profile on the upper 30 m (V_s^{30}) and the predominant site's frequency F_0 , which were consistent with the surface geology setting of each city. The maps suggests the zones more prone to ground motion amplification are the north side of Arica, the south-east area of Iquique, north of Iquique, by the ZOFRI industrial zone and in the northern part of Iquique's port.

Furthermore, a zone in the north of Arica was chosen to construct a 3D wave propagation model of the soil. The properties of the model were derived from interpolating the surface wave velocity profiles and combining this profile with the HV technique to obtain the depth to bedrock in all the control points. Simulations of strong motion within the study site were performed by means of the spectral element method (SEM). The simulations of a Ricker waveform shows that the 3D model is capable to appropriately introduce soil heterogeneity, topography and bedrock depth variability to calculate the soil amplification in the control points. Results were compared with the standard 1D approach.

Keywords: Seismic microzoning, surface wave methods, Arica, Iquique, spectral element method.

1. INTRODUCTION

It has been widely accepted by the seismic engineering community that the local soil conditions and the effects of surface geology on seismic motion can amplify the movement perceived by the structures, inducing, in several cases, significant and negative consequences in urban areas (Seed and Idriss, 1969). For countries with high seismic activity, such as Chile, actions to prevent human and infrastructure losses due to earthquakes are mandatory.

Chile is a country characterized for having high and intense seismic activity, Figure 1.1 shows all the major interplate events that have occurred since the sixteenth century. In the north of Chile, the last big earthquake occurred the past April 1st 2014 (01A-2014) with 8.2 Mw and a rupture zone of about 200 km of length. Prior to this motion, this region had not shown any major activity in the past years. Near Arica and Iquique, there are seismic intervals to big motions between 1615 and 1768, between 1768 and 1868, and between 1877 and 2014, from which can estimate a recurrence interval of 111 ± 33 years (Comte and Pardo, 1991). Furthermore, the 01A-2014 event released only 1/6 of the expected energy accumulated (Figure 1.1), which suggests that other large events are likely to occur in a near future.

To assess earthquake hazards, several studies were conducted in the north of Chile past years. Among the different approaches followed, seismic microzoning emerged as an effective strategy to assess the eventual impact of earthquakes, and for predicting seismic susceptibility within a city.

Seismic microzoning provides information regarding the soil conditions in specific areas within a city that may be more or less prone to site effects during an earthquake. Nonetheless, there are several ways to perform this microzoning. One of the most common approaches is the use of surface wave based methods (SWM) to estimate dynamic soil properties in representative sites. This has been applied in many cities and proven to be reliable to assess site effects (Leyton et al., 2010, Tuladhar et al., 2004, Scott et al., 2006, Chavez-Garcia and Cuenca, 1998), it is also low-cost and easy to carry out. In this investigation, microtremor recordings will be used to estimate surface wave dispersive characteristics and generate 1-D profiles of dynamic soil properties along 3 cities, Arica, Iquique and Alto Hospicio, located in the North of Chile, aiming to find areas that are susceptible to site effects. Additionally, with the purpose of constructing a 3D model from the collected data, a series of strong motion indicators were generated numerically.

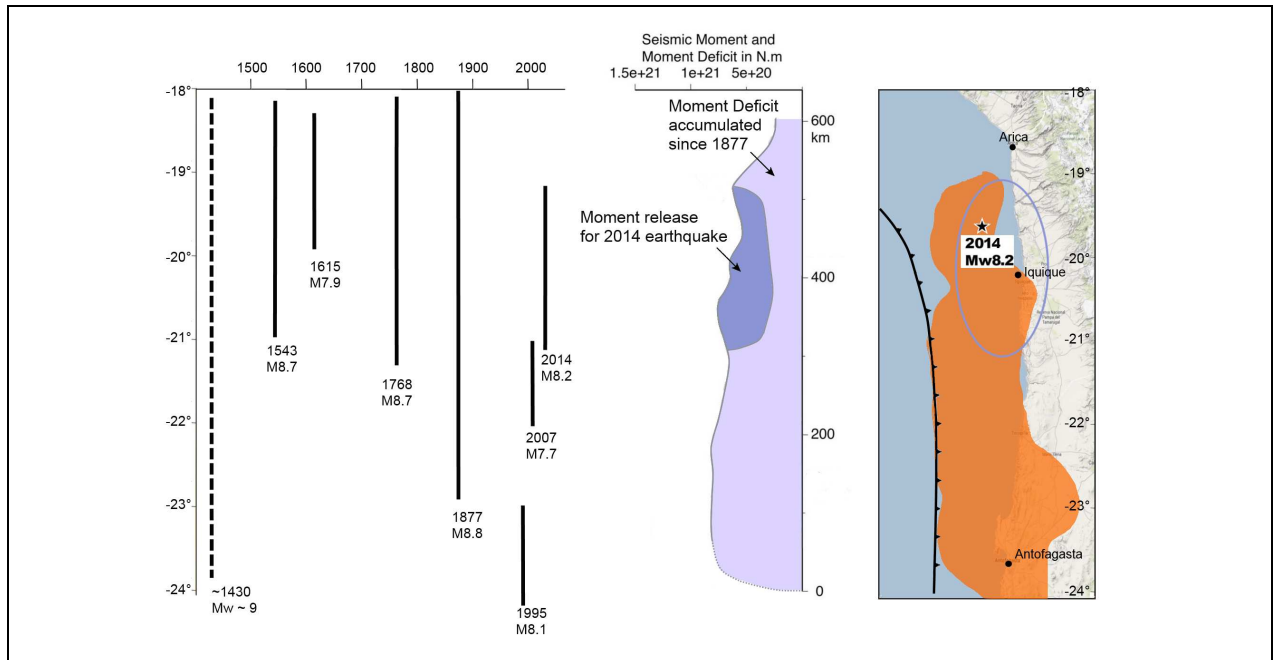


FIGURE 1.1: (a) Seismic context of Northern Chile. To the left, historical records show the seismic gap of 136 years that had affected this zone between 1877 and 2014. The image to the right illustrates the seismic coupling of over 75 % in the orange area and a comparison between the moment deficit accumulated since 1877 and the seismic moment released for the April 1st2014 event. The rupture area of the earthquake is marked in a blue line, obtained from the USGS Earthquake Data Report. Modified from Scholz and Campos (2012) and Chlieh et al. (2011).

In this regard, the government's funded project FONDEF + ANDES D10I1027 is developing a platform of seismic hazard for the north of Chile. The historic seismic gap that exists in this part of the country is large and the seismic risk in the zone is considered very high. In this respect, Arica, Iquique and Alto Hospicio, three of the main cities in the north, account for 79 % of the population in their regions, turning them into the focus of the following research.

In summary, this investigation will focus on the seismic characterization of the foundation soils in the cities of Arica and Iquique, the objectives can be enumerated as:

1. Applying geophysical surface wave based techniques to evaluate geotechnical dynamical properties of the sites in urban areas in order to identify zones more prone to site effects.
2. Evaluation of the microzoning reliability regarding the observed site effects of the A01-2014 earthquake.

3. Comparison between a standard 1D (horizontally layered) and 3D wave propagation models on homogeneous media, based on measured soils elastic properties.

In the following sections a brief description of the geological setting in the Northern Chile will be carried out to contextualize the problem. Subsequently, the theoretical framework used to determine a proper site characterization will follow, mainly focused on geophysical surveys. Afterwards, the next chapter will outline the fieldwork performed in each city. The chapter Microzoning will focus on the interpretation of the results and the construction of maps with the focus on the zones most prone to ground motion amplification. With the available information a zone of study will be chosen in the next chapter, and it will be used to perform a 3D wave propagation model in order to numerically estimate site effects. The final chapter will provide the conclusions of the investigation and the work ahead.

2. GEOLOGICAL SETTING

Chile is a country situated on the subduction zone of the Nazca plate under the South American plate, making it a zone exposed to high seismic activity. This contact extends along the west coast down to the Taitao peninsula, it has a convergence rate of 6.6 centimeters per year (Kendrick et al., 2003), which is the main reason of the seismic activity that affects the region, producing earthquakes with a magnitude M_w over 8 and mean rupture length of 400 km within this 3500km subduction boundary. These events happen with a recurrence of 10 to 15 years.

2.1. Geomorphology of Arica and Iquique

Arica and Iquique are two major provinces in the north of Chile. They include the cities of Arica, Iquique and Alto Hospicio. Together, they account for a population of over 350.000 inhabitants, which makes them three of the most important urban zones in the North, hence the interest of this research. They are located in the coast, to the west of the Chilean Coastal Range, which ends in the southern urban limit of Arica (Figure 2.1). Following sections will detail the surface geology of each city, in order to have a better understanding of the of the soil and bedrock setting, and at the same time be able to compare the consistency of the investigation.

2.1.1. Arica

Arica is a city located on the coastal plain west of the Coastal Range, conformed to a great extent by the San Jose's river delta. The city is situated above a sedimentary basin that extends from El Morro Hill to the El Lluta's alluvial fan. The basement is composed of Jurassic and Paleogene formations of volcano-sedimentary rocks (Maldonado, 2014). This author constructed a map of the surface geology in the city of Arica (Figure 2.2a), where it can be identified the different lithological units in the zone, consisting mainly of sedimentary and residual soil from the hills surrounding the city and the deposition of the rivers. It is also important to note the presence of artificial landfills near the port of Arica, west of El Morro hill. Figure 2.2a shows the main Quaternary and Neogene deposits recognized in the zone, although 11 of them are described, they can be grouped into 3 main deposit types that shape the geomorphology of the city. To the south, the city is limited

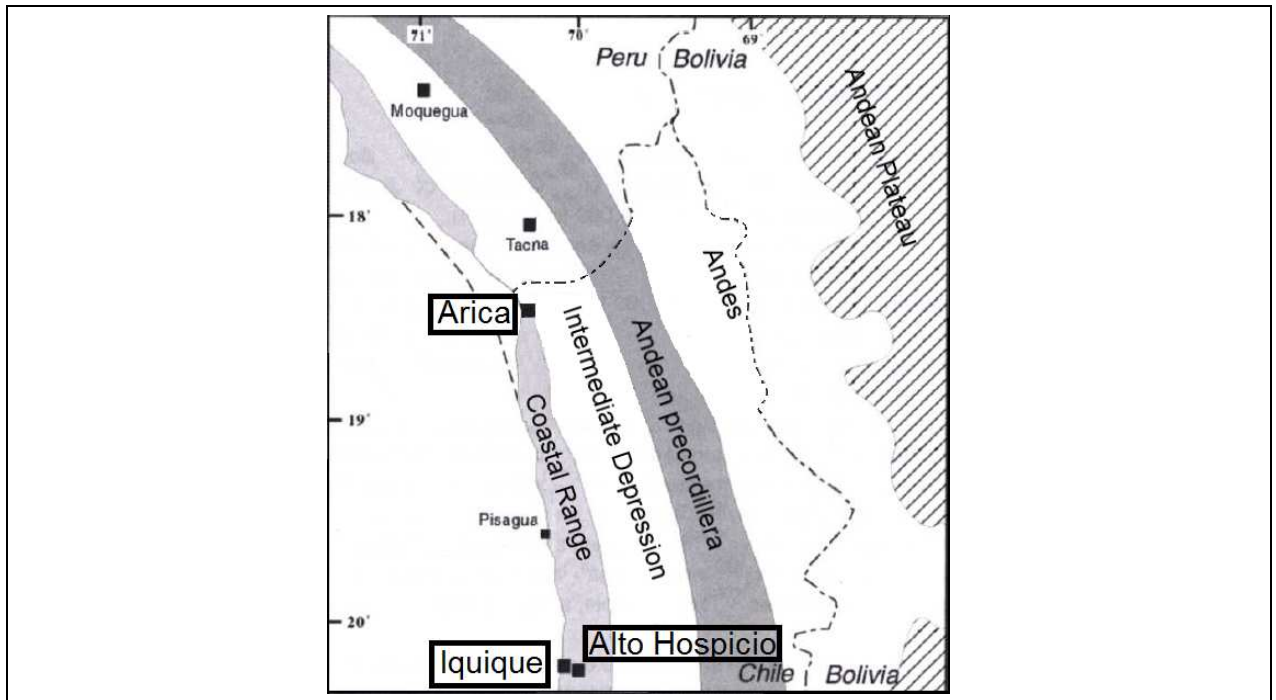
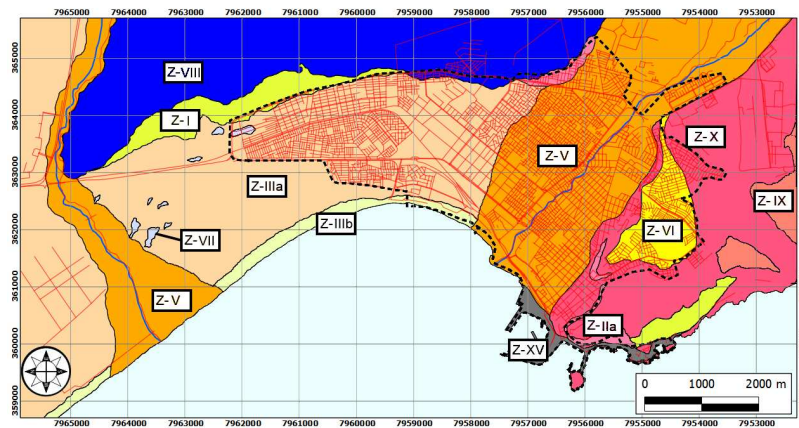
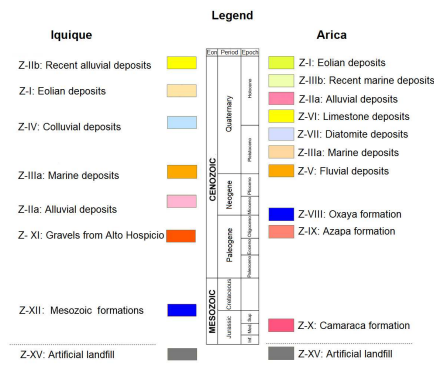


FIGURE 2.1: Major geographical units surrounding Arica and Iquique. The Chilean Coastal Range borders both cities towards the coast. To the east, the Intermediate Depression is the valley between the Coastal Range and the Andes Mountains that can be found further to the east. Past the Andes, the Andean Plateau is located in Bolivian territory. Modified from García et al. (2004).

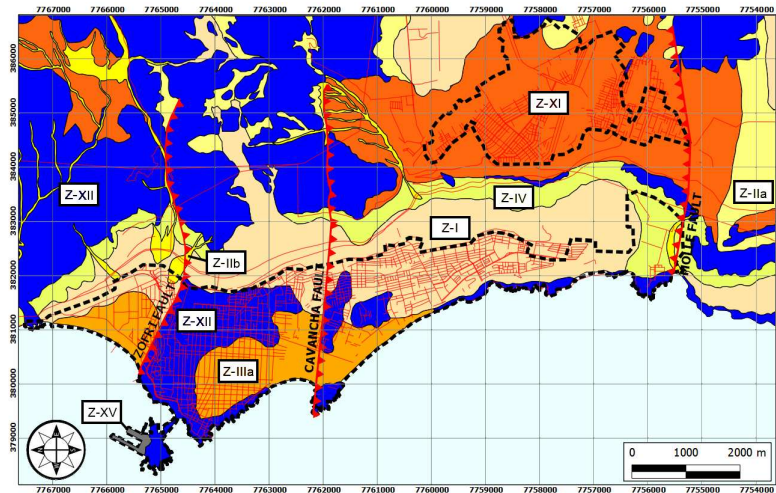
by the debris of the El Morro and La Cruz hills. The alluvial fan of San Jose's river is located north of the named hills. To the north-east, there is a composition of the debris from the El Chuño hill. And the northern area is characterized by eolian and marine deposits. The geographical and climatic conditions of the zone have formed a sedimentary basin throughout the years, constituted by fluvial depositions, debris and the continuous sea transgressions and regressions (David, 2013). The topography is fairly regular, except in the south where the hills El Morro y La Cruz raise up to 140 meters above sea level.



(A) Arica



(B) Legend



(c) Iquique

FIGURE 2.2: Geology maps of (a) Arica and (c) Iquique. The black dotted lines indicate urban extensions, while the red ones denote fault lines. Simplified from Marquardt et al. (2008), Maldonado (2014).

2.1.2. Iquique and Alto Hospicio

Unlike Arica, Iquique's geology is very heterogeneous. The city of Iquique comprehends the urban areas of Alto Hospicio and Iquique, both of them are located within the Atacama fault system, considered one of the oldest and largest fault systems in the country. This places Iquique in a zone crossed by several faults. The main ones that cut the urban area are the ZOFRI Fault, Cavancha Fault and Molle Fault, which can be noticed in Figure 2.2c. Most of the faults have a predominant E-W strike and a dip of about 60°S, except for the Molle Fault, with a dip of 30°N (Marquardt et al., 2008).

The city is characterized by the presence of Cenozoic sediments and overlying a medium to upper Jurassic igneous basement, composed of intrusive and pyroclastic rock. Figure 2.2c shows the main units inside the city. North of the ZOFRI Fault, marine deposits predominate in the area with a relatively shallow depth to bedrock. To the south, the town center is characterized by outcrops with a random distribution of thin layers of marine deposits. Furthermore, the Cavancha fault trace shows a clear separation between the different units. Towards the south of the city there is mostly eolian deposits from El Dragon hill intercalated with marine deposits. By the southern urban limit and near the Molle Fault, mostly marine deposits have been identified.

Alto Hospicio is located to the south-east of Iquique, above the great escarpment limiting the Coastal Range, at about 550 meters above sea level. The city's geology is defined by the presence of gravels consolidated with halite, commonly known as rock salt Marquardt et al. (2008). Several fault lines have been identified along the city but have not been properly defined, except for El Molle fault that is continuous from the coast.

3. SEISMIC CHARACTERIZATION OF A SITE

There are several techniques to evaluate the geotechnical dynamic properties of soils. Geotechnical in situ seismic active testing relies upon dynamic sources created from either an impulsive or harmonic source (Zywicki, 1999). These active experiments could be combined with ambient noise-based techniques to reach deeper layers. For the purpose of this investigation, an approach involving mainly the analysis of seismic surface waves shall be used.

3.1. Seismic waves

Seismic waves are generated by perturbations in the earth's crust and propagate along the crust all the way to the surface through elastic media. There are two main categories; body waves and surface waves.

1. Body waves: this type of waves propagates through the interior of a body, there are two kinds of body waves: P or compressional waves, which propagation direction coincides with the particle movement, and S or shear wave, which propagation direction is perpendicular to the particle movement.
2. Surface waves: these waves are the product of the interaction between body waves and the earth's surface, their main feature is that they propagate along the earth's surface and between the layers near the surface, and they are slower than body waves. These waves can be separated in two main classes: Love and Rayleigh. The former are produced through the perpendicular movement between the particle motion and the propagation direction, while in the latter, the particle motion follows an elliptic trajectory, and can be induced by a vertical source in the surface (impulsive or harmonic).

Figure 3.1 illustrates the particle motion of the main seismic waves previously described. For geotechnical purposes, the shear wave velocity profile in depth is a key parameter for evaluating dynamic response characteristics of a site (Tokimatsu, 1997). Generally, in-situ direct tests to evaluate shear wave velocities require boreholes and hence they can be inconvenient in terms of cost and time. Nonetheless, during the past decades, non-invasive tests based on surface waves have become very popular because they have proven to be reliable in characterizing site effects (Tokimatsu, 1997), while at the same time low-cost and easy to perform.

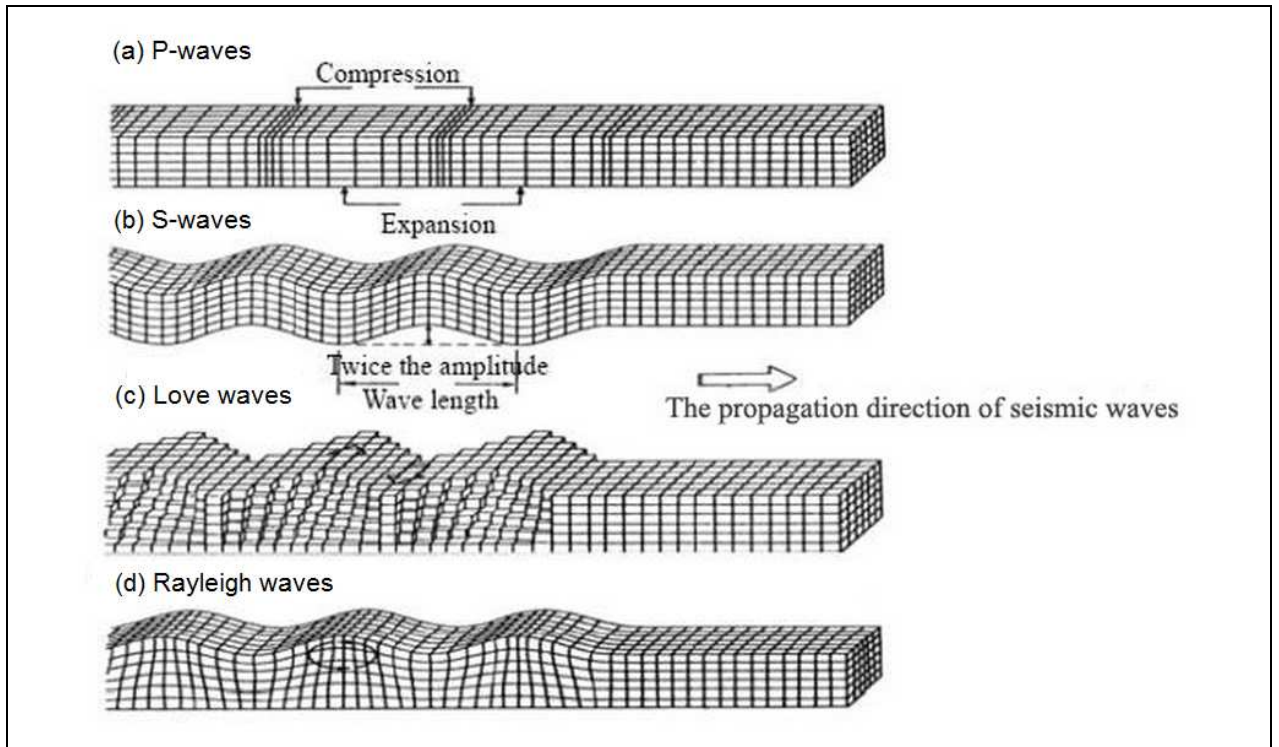


FIGURE 3.1: Types of seismic waves (Sauter, 1989).

There exist two classes of tests based on surface wave methods, the first consists of an active surface wave test, and uses an impulsive point source to create a seismic wave field, whereas passive sources benefit of ambient noise propagating along the surface, such as traffic, ocean vibrations, and microtremors. The former allows to identify soil characteristics for a high frequency range (usually between 10 to 40 Hz using a sledgehammer as controlled source), and the latter is used for low frequencies (typically between 1 to 25 Hz). Considering these characteristics, Humire (2013) proposed a combination of both kinds of tests in order to obtain an accurate characterization of the soil. With this combination, it is possible to identify the shallow wave velocity profile of the soil using the standard refraction equipment with 4.5 Hz geophones. Note that for this kind of tests, several sensors are required to record the waves field.

Besides the shear wave velocity profile, Nakamura (1989) proposes a methodology based on surface waves to determine the predominant period of the soil using a local three-component measurement. In the following sections, a more detailed description about these methods will be provided.

3.2. F-K method

The spectral frequency-wavenumber method, or simply F-K (Kvaerna and Ringdahl, 1986, Lacoss et al., 1969) is based on the identification of Rayleigh surface waves crossing the array so it may be applied successfully on urban areas with high ambient noise (passive source), or with an active source (Tokimatsu, 1997). To perform this test, a set of seismographs must be placed with a known geometry, so that wave forms arriving in each sensor may be properly combined. This will be called 'seismic array' from now on. In this methodology, 1D and 2D seismic arrays may be used, depending on the approach of the test.

3.2.1. Passive source approach

For a passive source, 2D arrays may be used. This method assumes that the array of geophones is crossed by a plane wave front with a frequency F and a wavenumber K (Figure 3.2). The recorded signal in each geophone is formed by the combination of the wave front crossing the array and by other ambient noise. Then, the signals are delayed according to the geometry. Incidence directions for the arrival times are assumed in which the wave front may coincide for all geophones, so they can be combined. The response of the array is the stacking of the delayed signals of all sensors (Figure 3.3).

A Fourier transformation allows to analyse the data in the F-K domain, so an energy spectrum

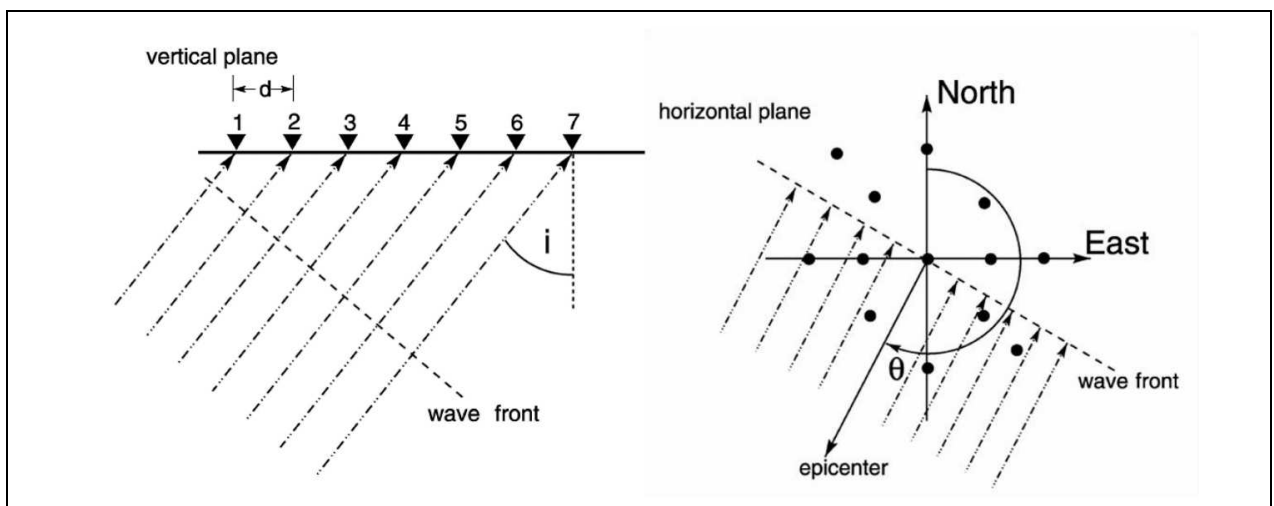


FIGURE 3.2: Plane wave front crossing a seismic array (Ohrnberger et al., 2012).

may be constructed according to the studied waveforms. Based on the recognition of the peak values of this spectrum, it is possible to identify a dispersion curve for each combination of frequency, phase velocity and incidence direction. Usually, the information obtained from this methodology is reliable for reasonably low frequencies (up to 15 Hz), however, this may vary depending on the stiffness of the soil and the geometry of the array (maximum and minimum observable wavelength). From the inversion of this curve, an estimation of a 1D surface wave velocity profile may be obtained in the more shallow layers of soil.

In this work, the passive approach of the F-K analysis was carried out on the circular arrays.

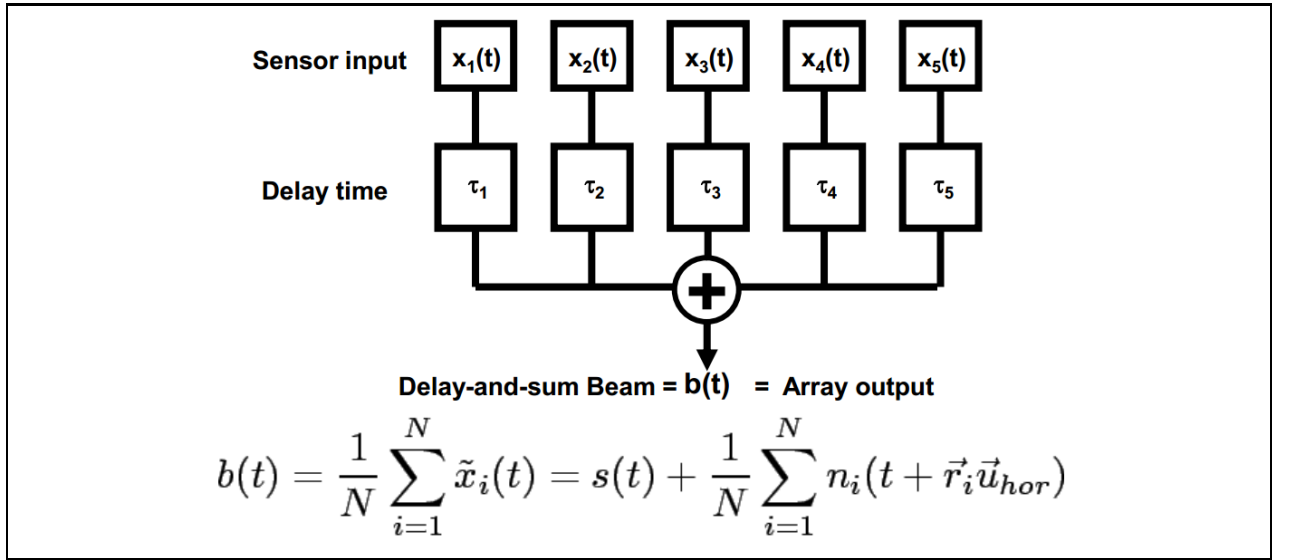


FIGURE 3.3: Combination of the record of each geophone to find the array response (Ohrnberger et al., 2012).

In order to do this, time windows were selected and analysed separately. An energy spectrum is obtained for each one, where the energy concentration could be identified. The dispersion graph is obtained by a normal adjustment to the results obtained in the different time windows (Figure 3.4).

One of the features of this approach is the F-K limits in which the array response is reliable (Wathelet, 2005a). These limits depend on the array configuration (size and geophones spacing), which define the maximum wavelength in which the methodology is effective (Figure 3.5). Generally, the F-K passive approach provides reliable dispersion curves that vary between 5 to 25 Hz depending on the soil stiffness and its corresponding wavelength, that permits to explore larger

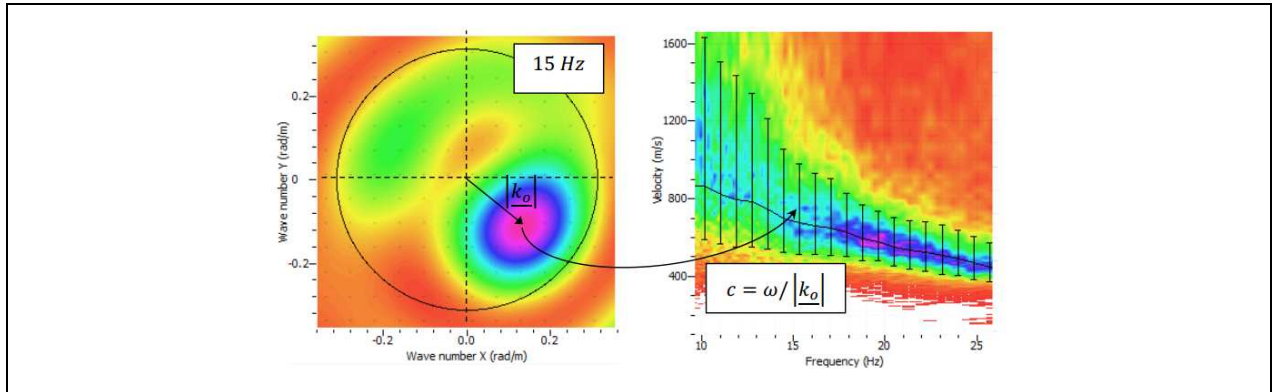


FIGURE 3.4: Example of an f-k analysis over one time window (left) at a frequency of 15 Hz for the computation of the dispersion curve (right) (Humire, 2013).

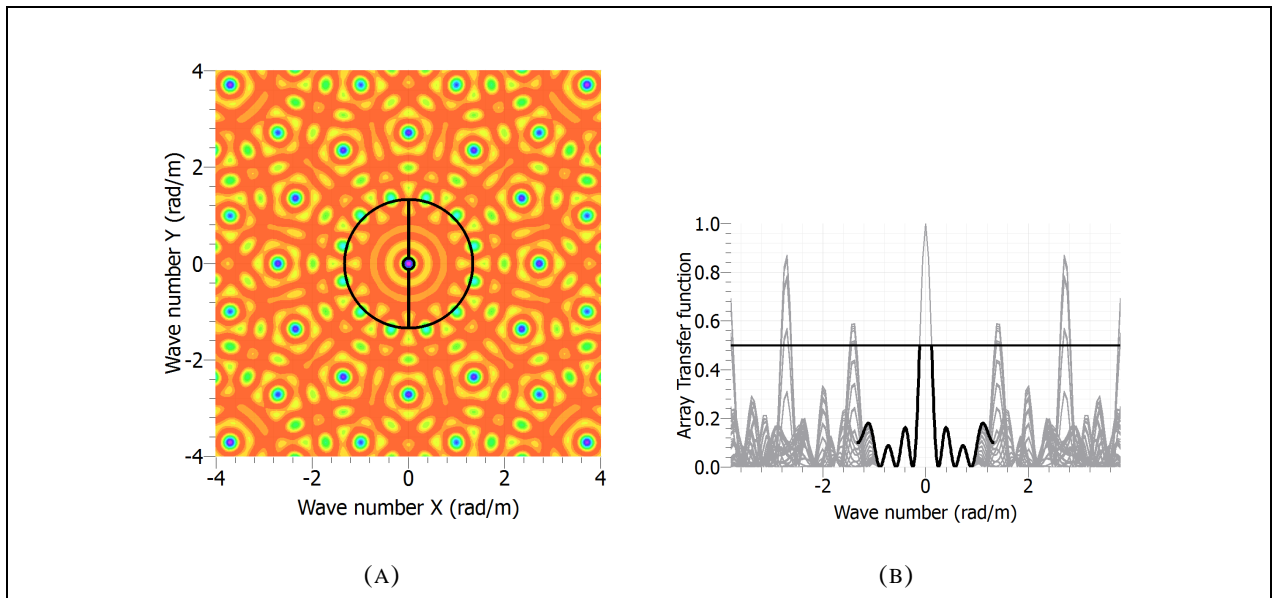


FIGURE 3.5: Response function for a circular array with a radius of 9.56 meters. The first image (a) shows the response function with a global peak in the center, and other local peaks. Image (b) shows response functions for different azimuths (wave front incidence direction), the central lobe denotes the capacity of the array to differentiate two wave fronts with similar wavenumbers.

depths compared to the active approach.

3.2.2. Active source approach

In this case, this approach uses 1D (linear) arrays for its implementation. The analytic procedure for the active source is analogue to the one previously explained, but the advantage is that the

source's position and direction of the wavefront is known. Nonetheless, the attenuation caused by the wavefront must be taken into account because the source is relatively close, hence, a geometrical attenuation factor is added to the process. Several expressions have been proposed for this factor, the most common is $\frac{1}{\sqrt{x}}$ (Foti et al., 2000), where x denotes the distance of each sensor to the source.

After this factor is applied, it is possible to combine the contribution of all signals so that the F-K spectrum for different wavenumber and frequency combinations may be calculated. The transformation, known as slant stack, allows to decompose the incident field in plain waves to filtrate the non-plain wavefront generated by the source, in order to obtain an accurate dispersion graph. Note that, unlike the dispersion curve for the passive approach, the active approach is very efficient for identifying a dispersion curve for higher frequencies (10 Hz or more).

Once the active data is ready to analyse, the waveform should look like Figure 3.6. At least

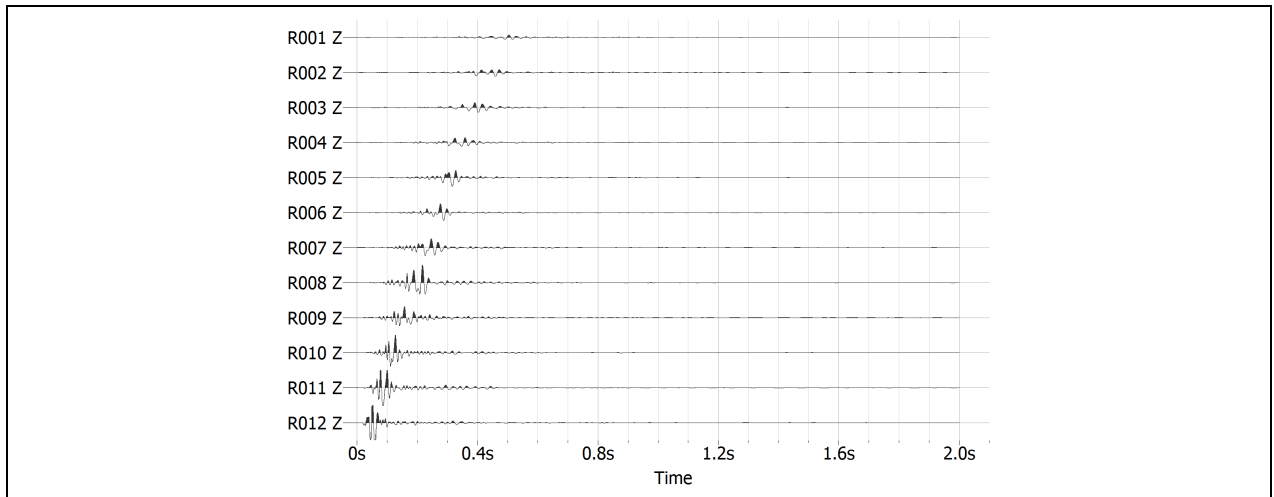


FIGURE 3.6: Vertical motion of a typical record used for the active F-K approach, in this case the shot is located at 10 meters from receiver R012.

three shots are carried out in every location to increase source to noise ratio. Generally these locations are 5, 10, 15 and 20 meters from the closest receiver. Hence, a total of 12 to 15 shots are recorded. For each one, a dispersion graph is generated. All of them are carefully analysed and combined for a common source location (time and/or frequency stacking). Once a group of consistent curves is selected for different source locations, they are stacked in the frequency domain

to form a final dispersion graph. Afterwards a curve is selected, representing the dispersive properties of the site (Figure 3.7). Usually, dispersion curves for active sources have a resolution of 10 to 40 Hz. This restriction is based on the maximum wavelength the arrays are able to acquire and the energy and frequency content delivered by the source. Note that the quality of this analysis is

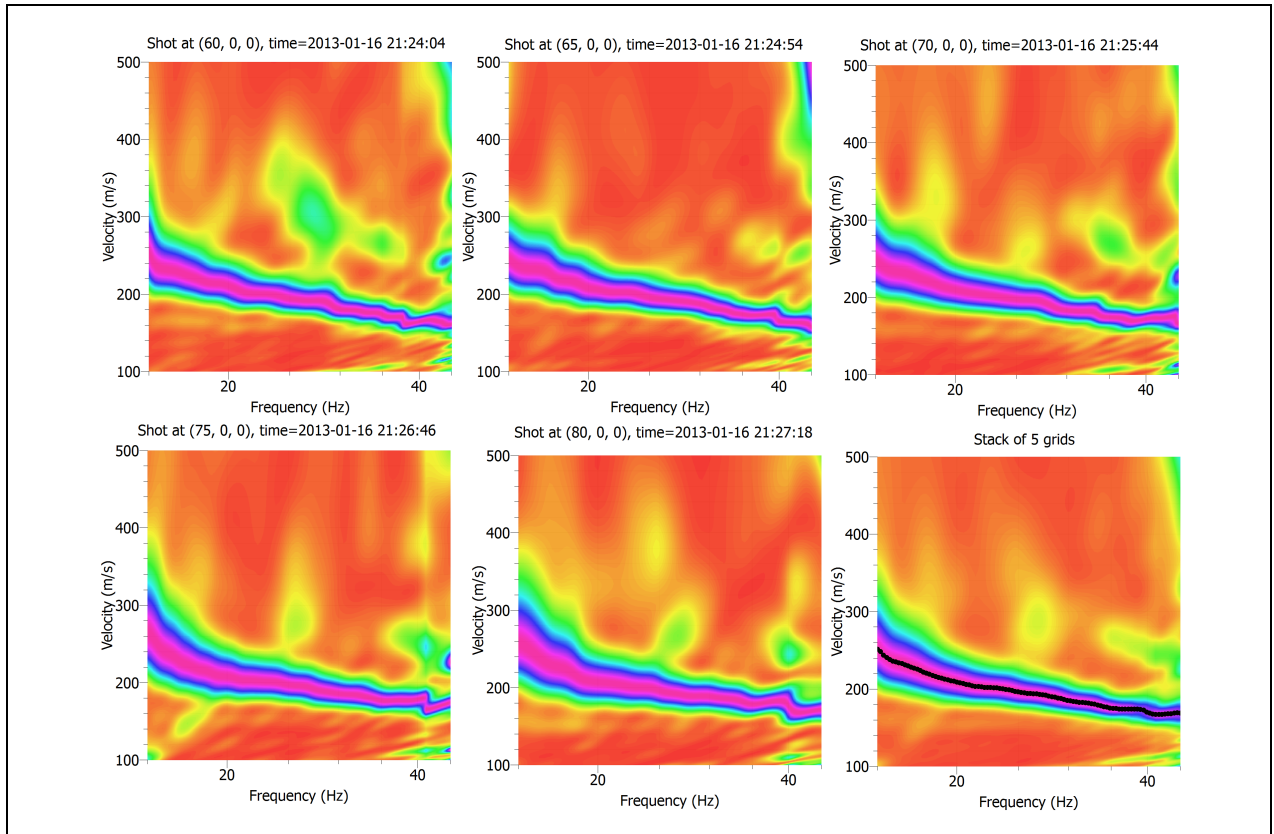


FIGURE 3.7: Dispersion graphs for an active source at different shot locations. The pink area represents the concentration of maximum energy of the array, and the black line is the final dispersion curve selected from stacking the previous 5 graphs.

highly related to the ambient noise, the stiffness of the soil underneath and the energy applied in the shot, among others (Humire, 2013). Hence, it is important to treat the data carefully and select the graphs that are consistent between each other.

3.3. RoadSide Multichannel analysis of surface waves

The RoadSide Multichannel analysis of surface waves (Roadside MASW) is a methodology derived from the common MASW method (Park et al., 1999). It allows the execution of passive

surveys through the use of 1D linear arrays. Like the F-K method, the RoadSide MASW defines a dispersion curve for each combination of frequency and phase velocity. One of the greatest advantages of this method is the use of vehicular traffic as passive source (Park and Miller, 2008), so it is very convenient for urban areas.

The solution of this method is very similar to the wellknown ReMi, or refraction microtremor (Louie, 2001), however, the initial hypothesis have a significant difference. ReMi assumes that the wavefront reaches the array with the same orientation as this one. So, the method interprets the progress of the wavefront as the separation between sensors while the effective distance could be different, which results in a higher phase velocity compared to the real one. RoadSide MASW recognizes that the wavefront may cross the array from any direction.

Park and Miller (2008) uses three different approaches to evaluate the dispersive properties of a site, based on the different directions the wavefront may take (Figure 3.8). For all three of them, a dispersion curve is obtained and combined. According to the authors, higher phase velocities for lower frequencies are obtained when the wavefront advances in a perpendicular direction to the 1D array, reaching up to a 10 % difference in the velocity model.

The software SeisImager/SW, developed by Geometrics[®], has an implementation of this analysis, and the dispersive curve obtained is generally consistent to the other analysis performed (active and passive tests). Once the data has been fixed, the only parameters the software needs are the frequency range in which the dispersion graph needs to be computed. After this is configured, the software computes the dispersion curve (Figure 3.9). Finally, the software allows to export this curve in a format recognizable by other softwares, which makes this procedure very convenient.

3.3.1. Spatial Autocorrelation Method

The Spatial Autocorrelation Method, or SPAC, uses the theory developed by Aki (1957), which relates the spatial and temporal correlation between seismic waves. The main hypothesis associated to this methodology is that the wavefield generated by ambient noise is an stochastic process, stationary in time and space, and it is composed mainly by Rayleigh surface waves. This principle allows to obtain the dispersive properties through the calculation of a spatial autocorrelation coefficient.

The application of this method normally requires 2D arrays of geophones (often circular), but

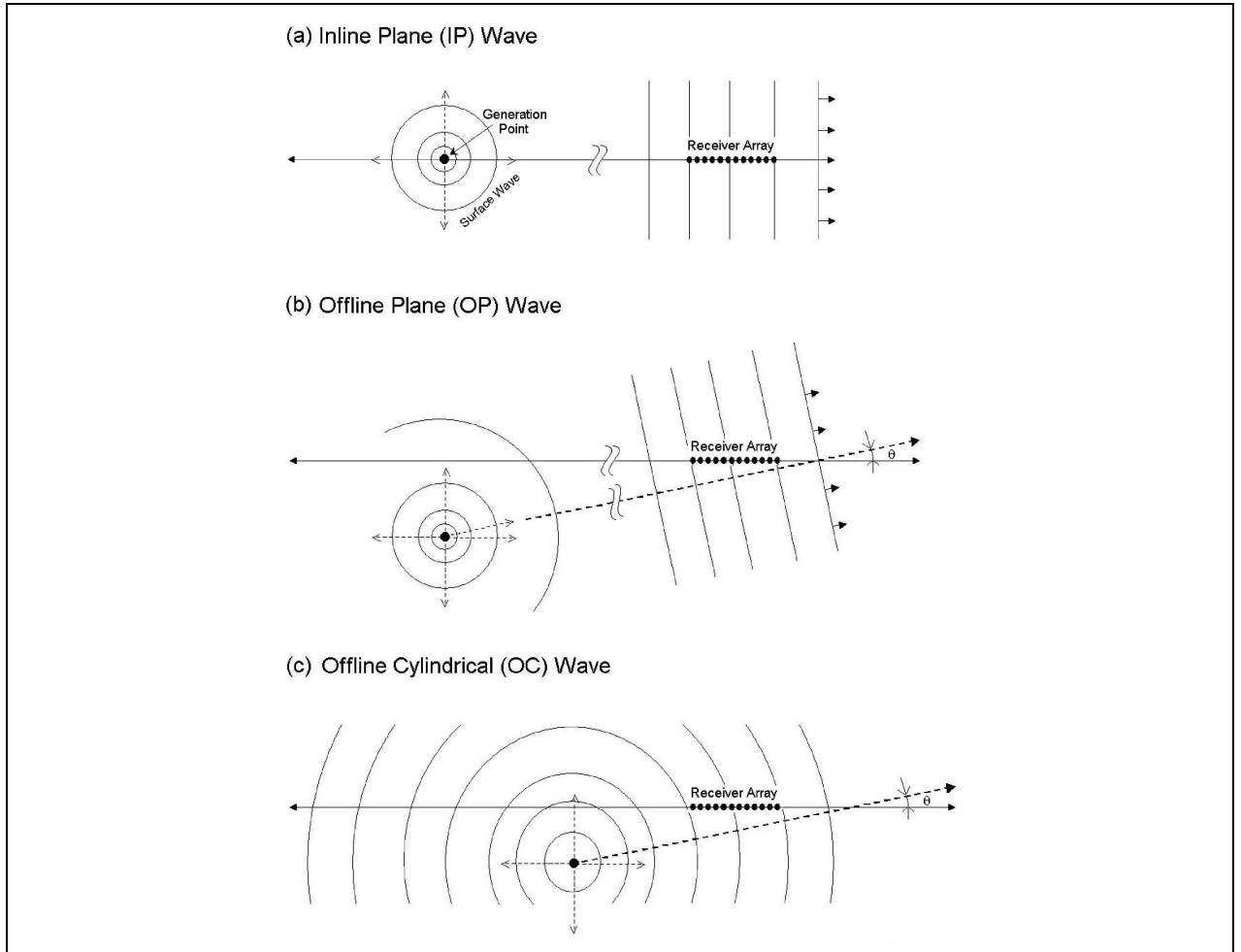
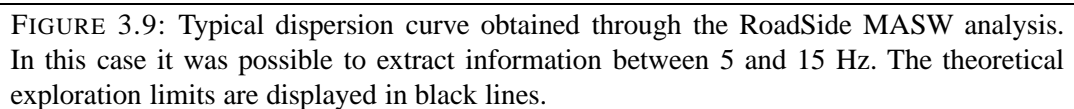


FIGURE 3.8: Different types of possible wave propagation employing a 1-D linear receiver array parallel to a road (Park and Miller, 2008).

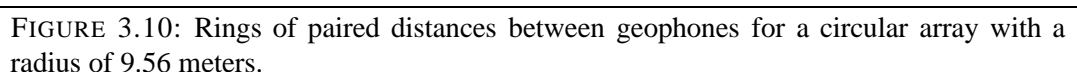
it has the advantage that it does not require so many geophones, like the F-K method, so it is possible to apply in large areas with fewer sensors.

The recorded signals can be reproduced by the spectral representation of a stochastic process for a specific time and position, which defines a spatial autocorrelation function between 2 points for a given time (Okada and Suto, 2003). Using Bessel's functions, the inversion of the autocorrelation function allows to find the dispersive properties of the layers underneath the seismic array, and hence construct a phase velocity profile for the site.

After preparing the data, groups of distances between geophones must be paired in rings in order to compute each autocorrelation curves (Figure 3.10). Once this is done, one autocorrelation



The main advantages of this analysis are (1) the ability to explore low frequencies compared



17

et al., 2006) and 2-D arrays. Nonetheless, the use on 1-D arrays is a bit more difficult because the dispersion curve is less accurate and requires a trained eye (Humire, 2013). In the present study, only 60 % of cases analysed by SPAC 1-D were successful, the rest would not compute consistent curves, and in many cases it tended to overestimate phase velocities.

3.3.2. H/V Spectral ratio

The previous described methods use multiple sensors to describe the dispersive properties of a site. The H/V Spectral Ratio (HVSR), however, only needs one triaxial sensor. This analysis was developed by Nakamura (1989), which compares the Fourier Spectrum of the horizontal and vertical components of the microtremor record at the surface. This method has been widely used in the past years and it allows to obtain the predominant frequency of a site, F_0 .

The first hypothesis (Nakamura, 1989) is that microtremors are mainly associated to Rayleigh waves, and the site effect amplification is due to the presence of a soft soil layer overlying a half-space (Chavez-Garcia, F. J.; Lermo, 1993). We may obtain from this hypothesis four components of ground movement, vertical and horizontal movement of the half-space, and vertical and horizontal movement in the surface. The amplitude effect of the source may be estimated as the ratio between the amplitude spectrums of the vertical component of motion in the surface (V_S) and the half-space (V_B).

$$A_S = \frac{V_S}{V_B} \quad (3.1)$$

Another parameter of interest is the ratio between the amplitude spectrums of the horizontal component of motion in the surface H_S and the half-space H_B .

$$S_E = \frac{H_S}{H_B} \quad (3.2)$$

Both parameters may be combined to compute a modified site effect function, S_M , as

$$S_M = \frac{S_E}{A_S} \quad (3.3)$$

if the ratio $\frac{H_b}{V_b}$ is equal to unity (considering ambient vibrations in the bedrock do not have a predominant direction of propagation). According to this hypothesis, the site effect function, may be approximated as

$$S_M = \frac{H_S}{V_S} \quad (3.4)$$

When the signals are recorded, this function is evaluated in many different time windows for such record, obtaining many spectral ratios that are then compared between each other and averaged.

Several authors (Chavez-Garcia, F. J.; Lermo, 1993, Tokimatsu, 1997, Bonnefoy-Claudet et al., 2009) have proved the correlation between the predominant frequency of a site and the peak of the HVSR. The amplitude of the HVSR is related to the contrast of impedances between the different materials, but it has not been fully understood (Pilz et al., 2010). Based on this amplitude, the peak of the HVSR may be more or less easily to identify.

The shape of the curve also has several interpretations. Bonnefoy-Claudet (2009) shows that flat H/V curves or with a low amplitude in its peak are related to sites with lower impedance contrast, while as broad H/V peaks might indicate the presence of a dipping underground interface between softer and harder layers, which is associated to significant 2D-3D effects. Another important interpretation of this ratio is that flat curves, where it is not possible to identify the peak of the H/V curve, is typical in rigid soils such as gravel deposits (Leyton et al., 2010).

This ratio may also provide significant information about the depth of the bedrock in a site. Following SESAME guidelines (Bard et al., 2004), if the 1D surface wave velocity profile is known, the depth to the bedrock may be estimated as

$$\overline{H} = \frac{V_S}{4F_0} \quad (3.5)$$

where V_S is the averaged 1-D shear wave velocity profile, F_0 is the predominant frequency obtained by the HVSR, and \overline{H} is the estimation of the depth to the bedrock.

A typical record of a triaxial geophone used for H/V analysis is shown in Figure 3.11. The software used to process this data is a script developed by Leyton (2010), one of the features of

this script is the selection of variable time windows. In the first place, time windows are selected so that there is major amount of free vibrations caused by artificial perturbations that may alter the estimation of the fundamental frequency. Then, the rest of the time windows are selected and analysed as explained previously.

A continuous Fourier transformation is then applied to see the results in the frequency do-

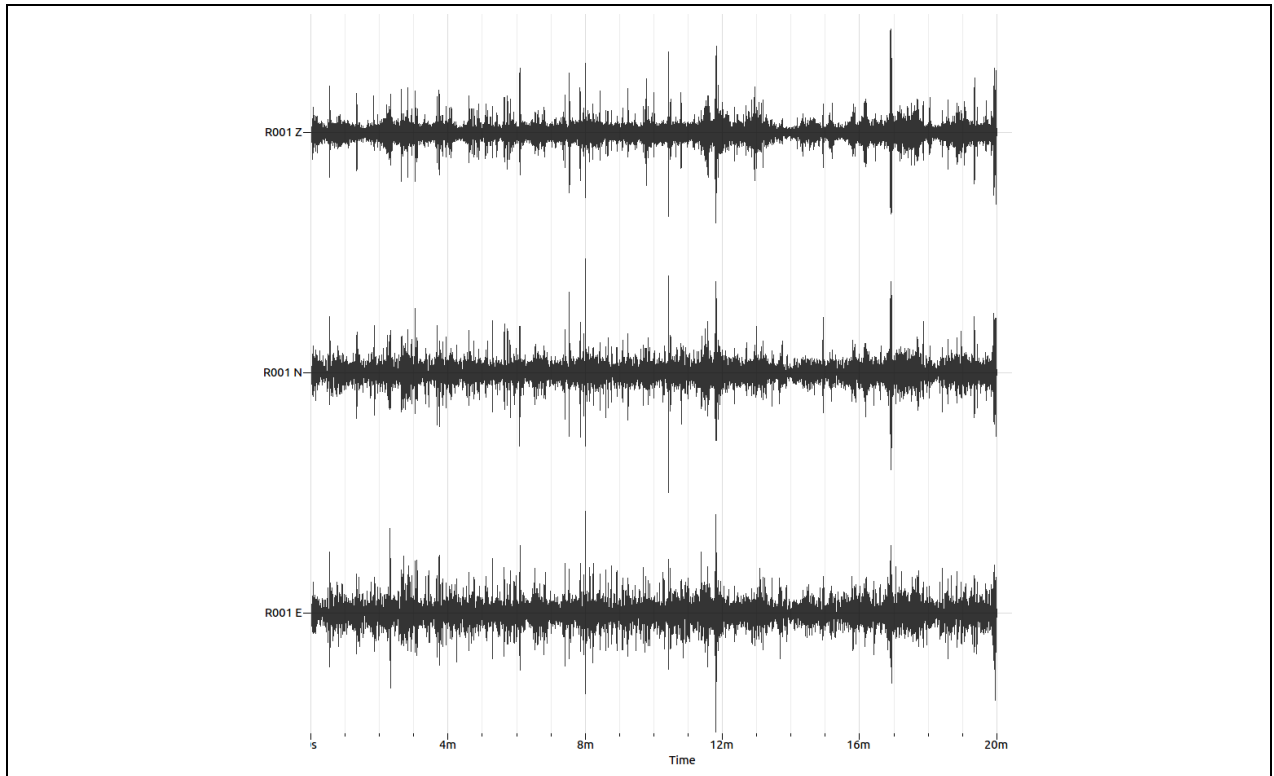


FIGURE 3.11: Record of the velocities in the 3 components registered by a Tromino, North-South, East-West, and Vertical motion.

main, and be able to visualize the peaks and evaluate the predominant frequency of the site in study. Typical results are shown in Figure 3.12.

Note that in many cases a peak such as the one shown in Figure 3.12 will not be so clear. In this investigation, evaluation of the reliability of the curves will follow SESAME Guidelines (Bard et al., 2004).

In each site, at least three recordings of 20 minutes each were carried out with the triaxial geophone, and one result out of them is selected for each site to characterize the soil below, generally, the one with higher amplitude or a clear peak is chosen.

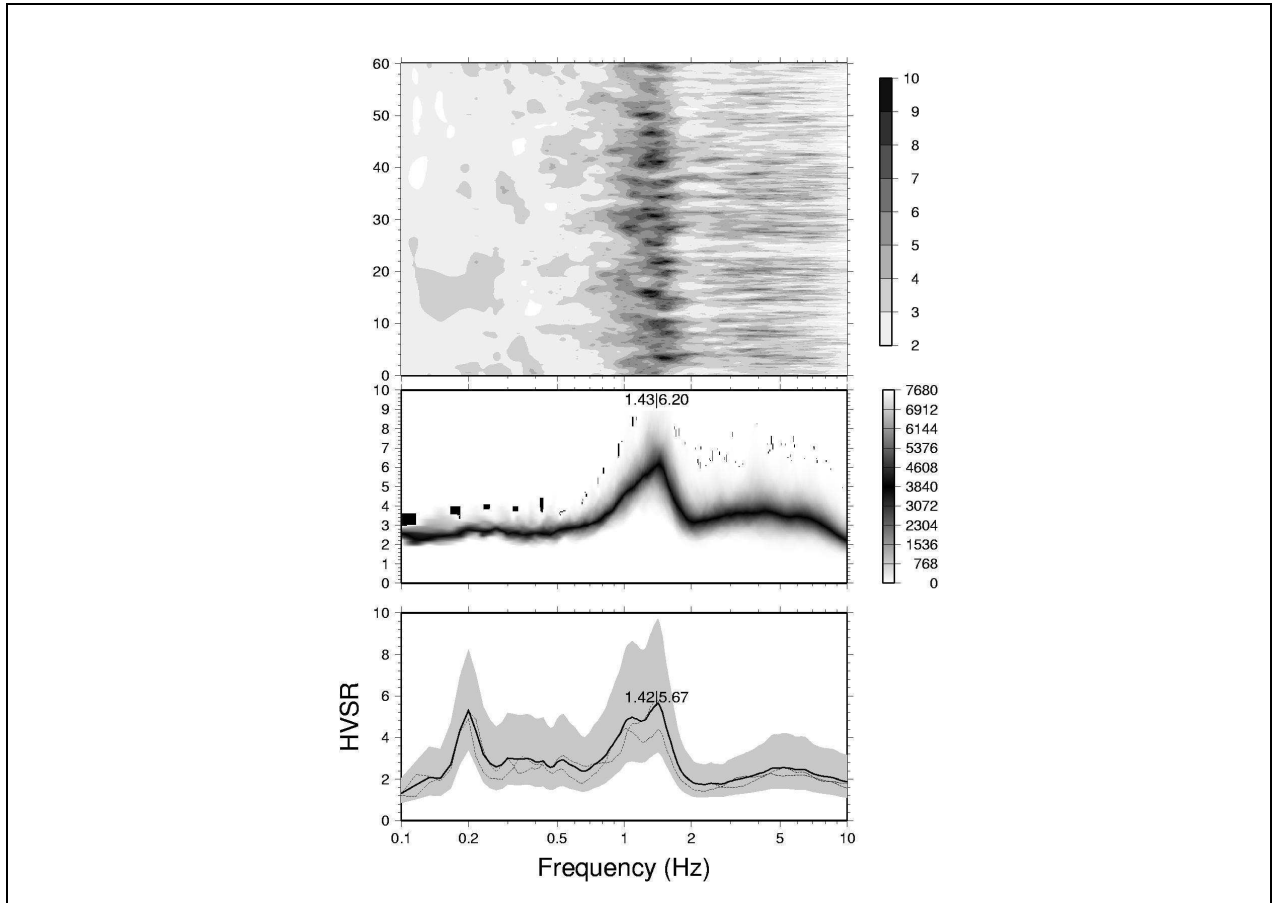


FIGURE 3.12: HVSR results for one site. The first image (bottom) shows the results of the averaged standard deviation of the H/V Spectral Ratio in each window, indicating the amplitude that the associated fundamental frequency reaches in its peak. The second image (center) is the statistic median of the spectrum, grouping the windows that have a similar frequency and eliminating those that are too far away from the average. Finally, the third image (top) indicates frequency associated to the previous 2 graphs by time window, in other words, it is an indicator of the stability of the result.

3.4. Vs profile and HVSR computation

The analysis of the obtained data was carried out through the combination of the methodologies. The number of performed analyses is shown in table 3.1. As may be seen, the numbers of each type of analysis is very varied, this is due to the quality of the results of each procedure, in other words, in many cases the dispersive characteristics obtained from the analysis were very scattered and a proper dispersion curve could not be obtained. Another important reason is the space restrictions during field work, particularly, in Iquique it was very hard to conduct 2-D arrays, therefore,

mostly linear arrays were carried out for this city.

Once the acquisition has finished, the data is processed through 3 softwares: the open source

TABLE 3.1: Number of analysis carried out in each city.

	Arica	Iquique	Alto Hospicio
Linear SPAC	23	35	3
Circular SPAC	21	12	2
Active F-K	45	52	5
Passive F-K (2D)	32	14	3
MASW RoadSide	30	48	4

Geopsy, which is able to perform SPAC and active/passive F-K analysis. The commercial software SeisImager/SW[®], able to perform MASW RoadSide analyses, and a script developed by Leyton (2010) to carry out the HVSR. Once all the results are obtained, they are combined to obtain a reliable description of the explored site's dispersive properties, as is depicted in Figure 3.13.

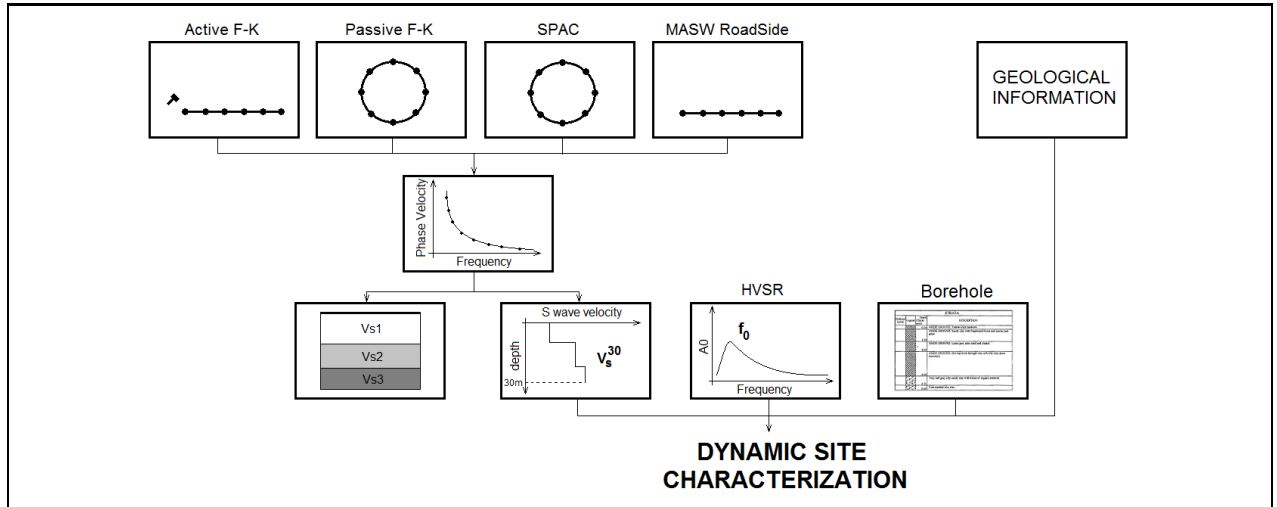


FIGURE 3.13: Flowchart of the procedure followed to obtain a final S wave velocity profile.

3.5. Combination of dispersion curves and surface wave velocity profile inversion

All of the dispersion curves that have been obtained through the varied methodologies can be incorporated in the software Geopsy to construct a broad curve that will extend its range from low to high frequencies. It is important to note that this range may vary based on the type of soil, the

arrays used and the quality of the acquired data, but generally, a combined curve should have a range between 4.5 and 45 Hz, as geophones of natural frequency of 4.5 Hz were used in this study, dispersive data below this value is not reliable. For very rigid soils (gravel, bedrock), the lower limit of this range does not normally extend lower than 10 Hz.

Typical results of this combination are shown in Figure 3.14, which shows the union of curves of a circular SPAC, a circular passive F-K analysis, a MASW Roadside and a linear active F-K analysis. It may be noticed that the union between these curves is almost continuous, this trend is evident in most cases and it has proven to be effective by Humire (2013). In several cases, a limited combination of analyses is used, not including all the available dispersion curves because of the lack of information from one or more tests, as it is evident in Table 3.1.

Once a final dispersion curve has been obtained, an inversion process is executed through the neighbourhood algorithm (Wathelet, 2008), implemented in Geopsy. It allows to compute a 1-D horizontally layered profile of the soil, which elastic properties are adjusted to its dispersive characteristics. The adjustment of this model is measured through a misfit, computed by Geopsy as shows Equation 3.6:

$$\text{Misfit} = \sqrt{\sum_{i=1}^{n_F} \frac{(x_{r,i} - x_{c,i})^2}{\sigma_i^2 n_F}} \quad (3.6)$$

where n_F denotes the total number of sampling frequencies for the dispersion curve, $x_{r,i}$ the value of the phase velocity in that point, σ_i the standard deviation in that point calculated by Geopsy, and $x_{c,i}$ the value of the phase velocity of the adjusted model. Generally, a misfit below 0.2 is taken as an acceptable model, however, this may vary and a visual inspection of the adjusted dispersion curve is necessary in order to accept or reject an inversion.

A typical inversion model with its adjusted dispersion curve is shown in Figure 3.15. Note that when a SPAC analysis is included in the inversion model, the autocorrelation curve is directly used to perform the inversion. The case in Figure 3.15 has a misfit of 0.035, and the adjusted curve is very close to the one calculated by the methodologies previously explained.

This process was carried out in all 102 sites, and a 1-D surface wave velocity profile was obtained for each. Besides this profile, at least 3 HVSr measurements were performed in each site in order to get its predominant frequency F_0 , and be able to combine all of this data to get a more

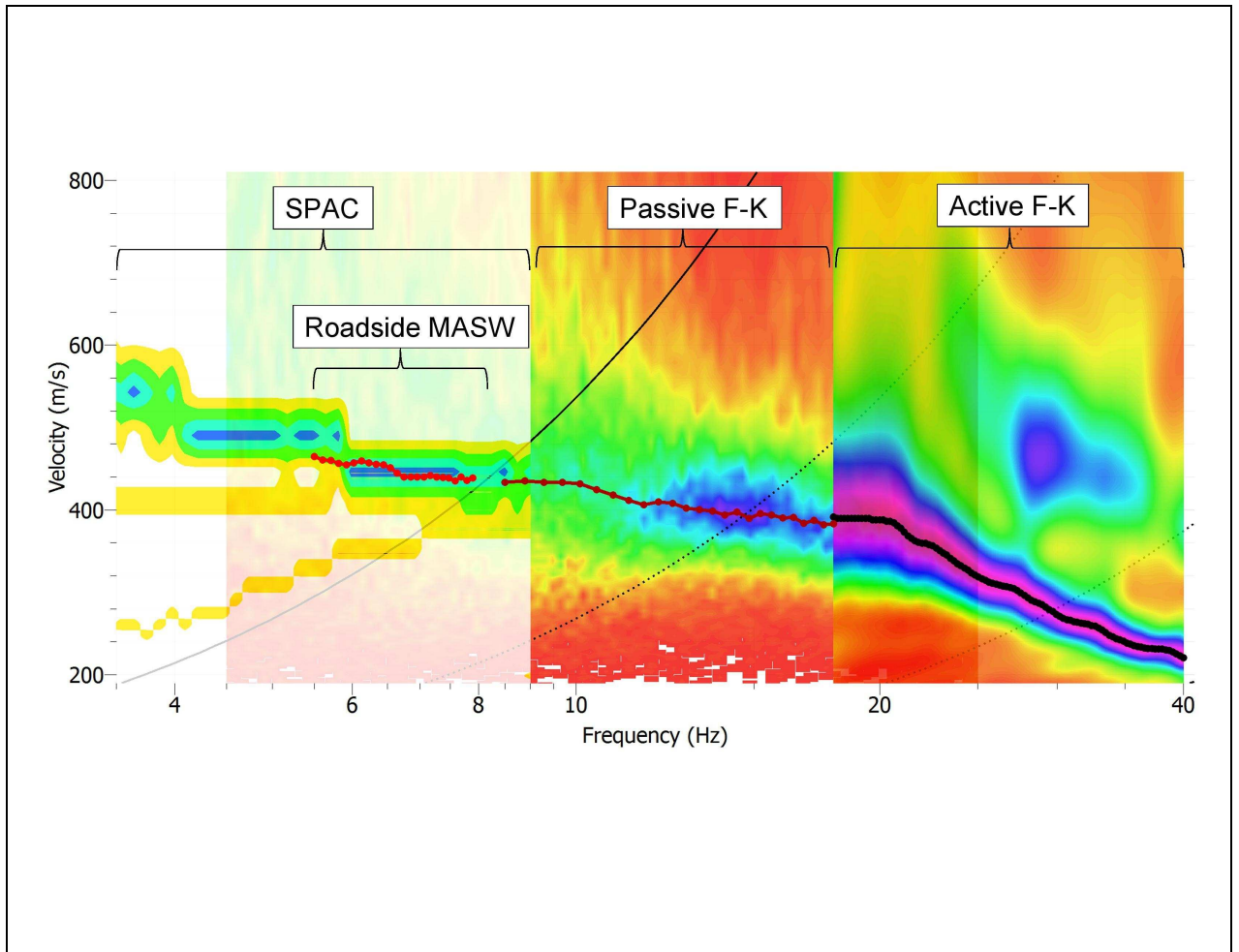


FIGURE 3.14: Combination of dispersion curves for one site. From left to right: in green the curve obtained from the autocorrelation coefficients, then in orange the dispersion curve obtained through the MASW RoadSide method implemented in SeisImager. In the middle the dispersion curve of a passive circular F-K method, and to the right, the dispersion curve obtained from an active linear test, analysed also through the F-K methodology.

complete representation of the explored site.

3.6. Limitations of surface wave methods

The limitations associated to the methodologies previously explained must be taken into account when the interpretation of the results is performed. They are related to the hypothesis of the assumed model, and may be enumerated as follows:

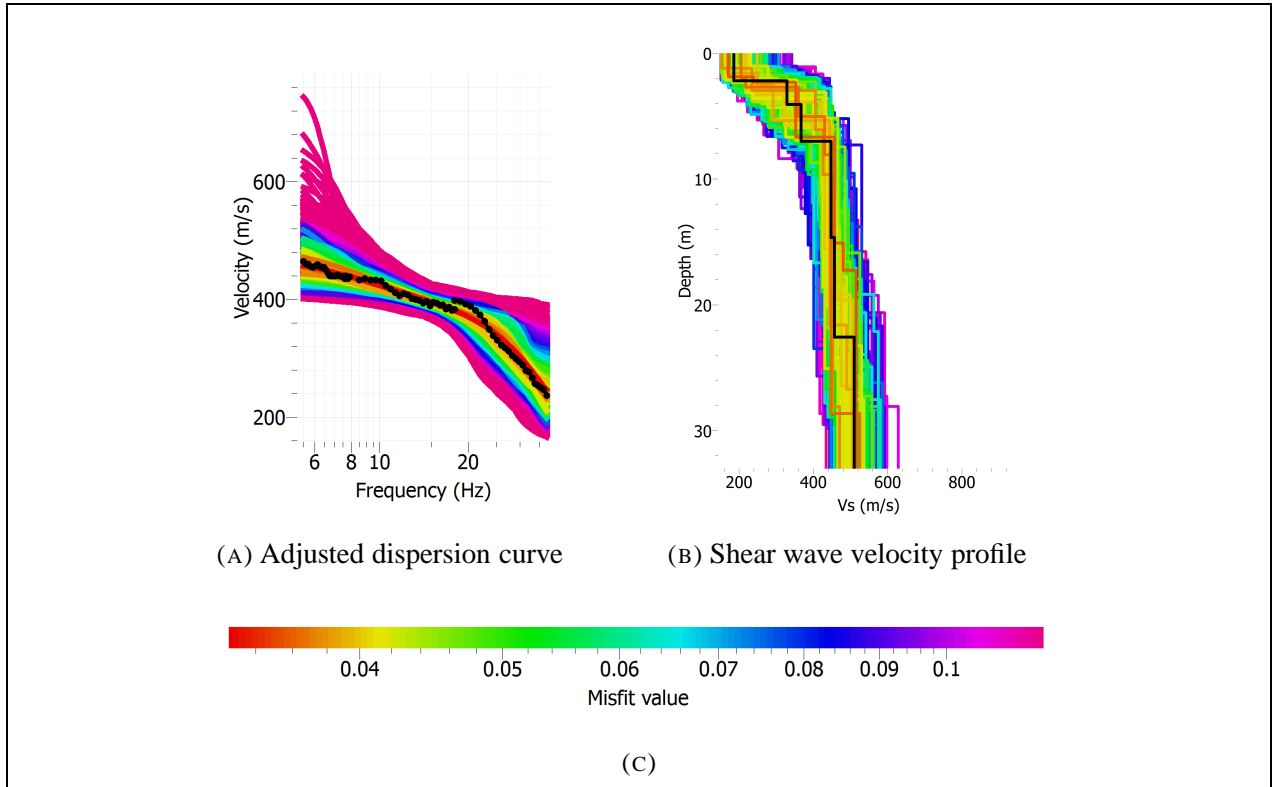


FIGURE 3.15: Inversion process carried out from the experimental data, the figures show all the possible combinations of proposed dispersion curves (a) and shear wave velocity profile (b), based on the adjustment value to the previously obtained dispersion curve. Usually a misfit that is considered acceptable should be below 0.2.

1. The inversion methodology assumes that the layers underneath the seismic array are parallel and horizontal. This must be treated carefully when the surveys are performed near hills or with a complex topography.
2. The dynamic characterization of soils through this method is performed assuming small strains, that means, keeping the elastic range of the material. For higher strains, the soil's behaviour stops being linear and the shear modulus is reduced, a feature that is not able to be analysed or discriminated with these methodologies.
3. The range of frequencies in which each method provides reliable information is limited in each case, therefore limiting the exploration depth that can be assessed. Typically, the resolution of the dispersion curve will decrease as the depth increases. The results of the

current investigation indicate that the minimum wavenumber (k_{min}) or maximum wavelength (λ_{max}) that the array is able to record are:

$$\frac{\pi}{D_{max}} \leq k_{min} \leq \frac{2\pi}{D_{max}} \quad \text{or} \quad D_{max} \leq \lambda_{max} \leq 2D_{max}$$

where D_{max} denotes the maximum opening of the considered array. This result is in agreement with the limits suggested by the Geopsy's developers (Wathelet, 2005b).

4. DATA ACQUISITION

4.1. Geophysical surveys

Two phases of fieldwork were designed in order to properly characterize the observed geological soil units of each city (Figure 2.2). First, using available satellite images a series of sites were identified that would offer enough space to perform the tests. In each city, about 45 sites met the requirements to perform geophysical surveys. Afterwards, fieldwork took place in Iquique and Alto Hospicio during December 2012 and Arica during January 2013. In all three cities, two types of geophysical surveys were carried out for the seismic characterization of each site. The first one consists of the use of a single Micromed[®] Tromino three-component data-acquisition system, designed for HVSr measurements Nakamura (1989). The second one is a Geometrics[®] Geode-12 seismograph with 12 channels. Vertical sensors (geophones) with a natural frequency of 4.5 Hz were used.

In every site three measurements were performed using the 12 channel device. The first consists of a linear array with an active source at different distances from the first geophone, with a sampling rate of 0.125 ms and a recording duration of 2 seconds. The second also uses a linear array, but records only ambient noise, and the third one uses a 2-D array (usually a circle) and also records ambient vibrations, both use a sampling rate of 16 ms and a recording duration of 16 minutes (because of the internal memory limitations of the device, four files of 4 minutes each were recorded). The geometry of the arrays are restricted to the wire spacing between geophone connections (5 meters maximum) and the space restrictions of the site itself. Figure 4.1 shows the largest array sizes for each survey.

For the active source, a 18 lb sledgehammer is used to induce the perturbation, at a distance of 5 to 25 meters from the first geophone, this hammer has been shown effective for obtaining a suitable dispersion curve in a range of 8 to 40 Hz (Humire, 2013). This may vary depending on the stiffness of the soil, the ambient noise, the depth to bedrock and the arrays size.

Furthermore, at least three surveys were executed with the Tromino for HVSr computation in every site. Each survey had a duration of 20 minutes, and a sampling rate of 7.8 ms (128 Hz).

Forty-five sites in Arica and forty-seven sites in Iquique were selected to perform geophysical

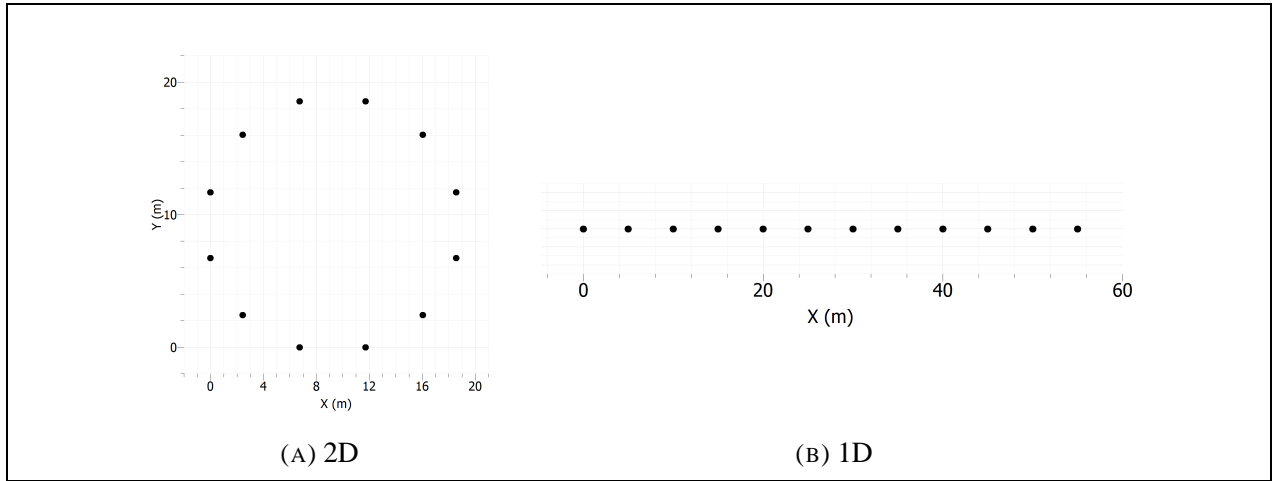


FIGURE 4.1: Geometry of the seismic arrays for its maximum size, circles (left) have a maximum radius of 9.56 m, and lines (right) can be as long as 55 meters.

tests. The selection of the sites was based on the different geological units and the availability of space in the zone. Figure 4.2 shows the sites selected in both cities.

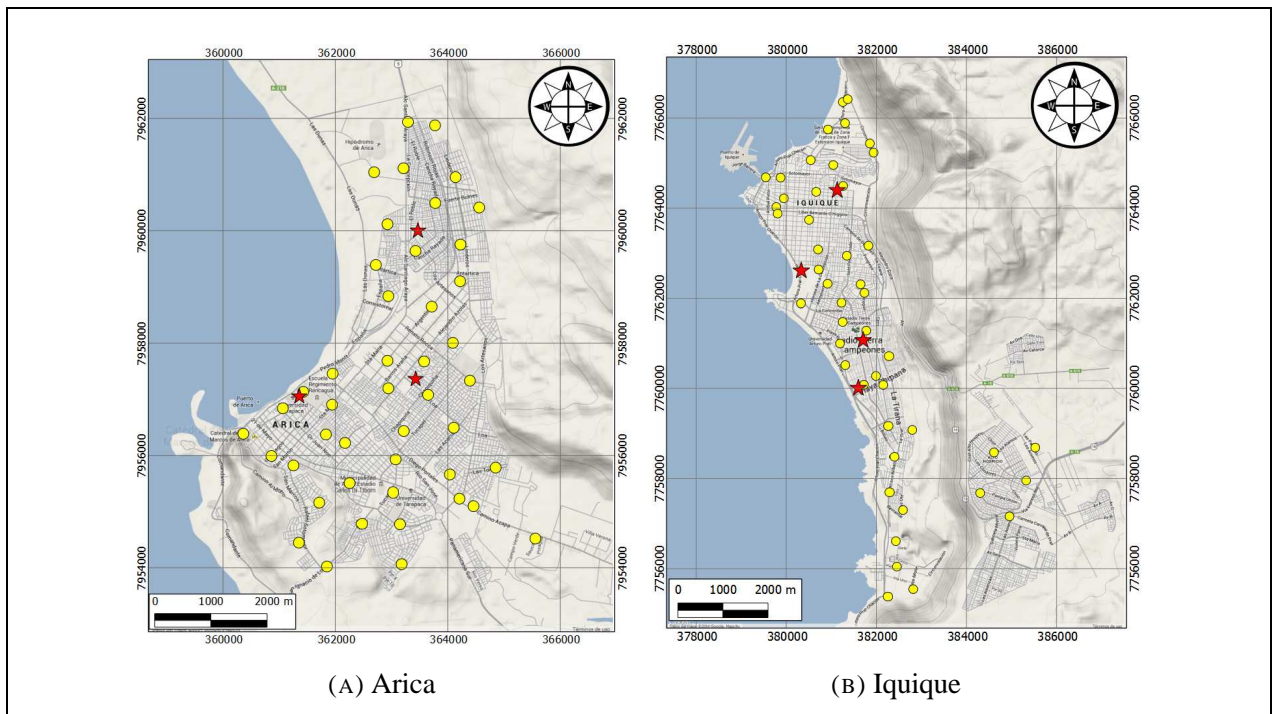
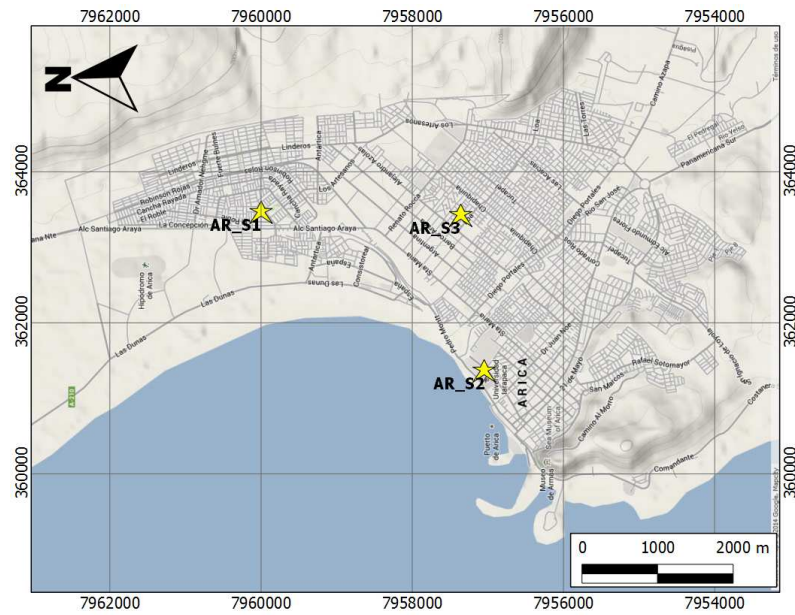


FIGURE 4.2: Spatial distribution of the explored sites in Arica, Iquique and Alto Hospicio. HVSR and Vs surveys are shown in yellow circles, while drilled boreholes are shown in red stars.

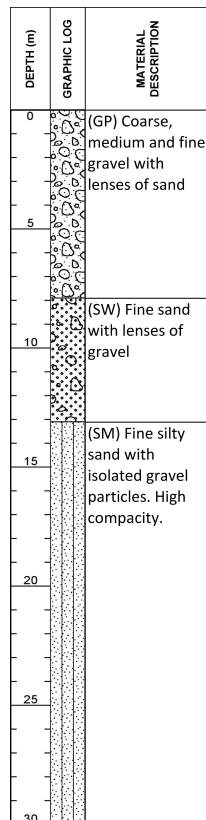
4.2. Boreholes

Additionally, seven boreholes were drilled to further investigate the physical properties of the soil. They reached a maximum depth of 30 meters unless bedrock were found at shallower levels. Figure 4.2 shows the location of the boreholes in each city.

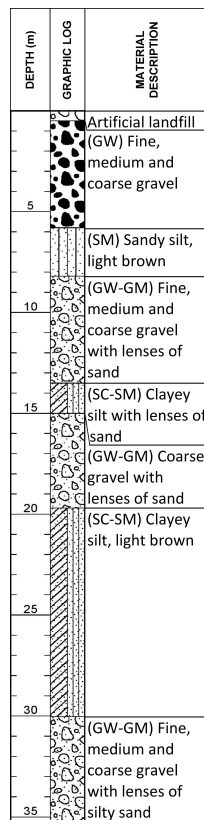
Drilling samples were extracted every one meter, and they were sent to the Ministry of Public Works Laboratories for performing a USCS soil classification. Unfortunately, no further tests were carried out because the samples were heavily perturbed, due to their transportation to the laboratories in Santiago. Nonetheless, the information obtained from them was highly useful to determine the main properties of the soils, the water table depth and the different layers of materials. The location and the borehole logs may be depicted in Figures 4.3 and 4.4.



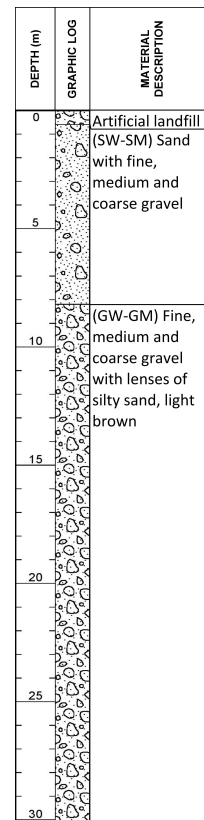
(A)



(B) AR_S_1

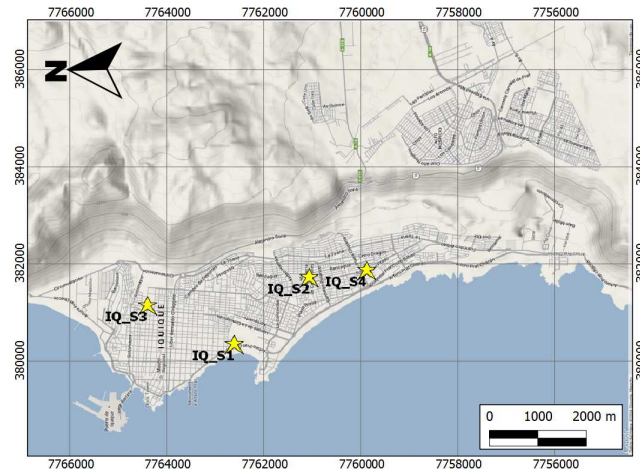


(C) AR_S_2

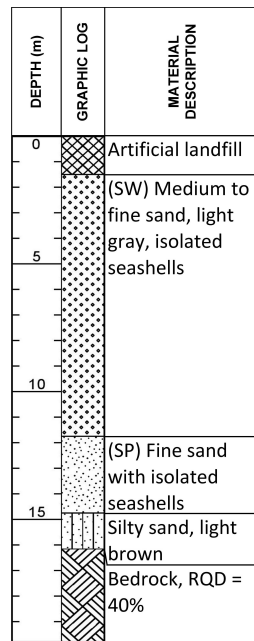


(D) AR_S_3

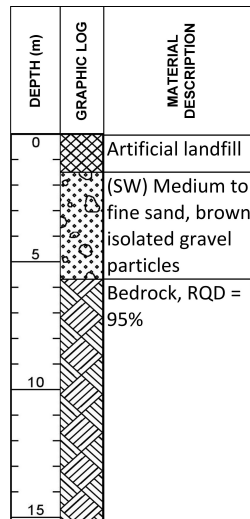
FIGURE 4.3: (a) Location of boreholes drilled in Arica. (b) to (d) Boreholes log.



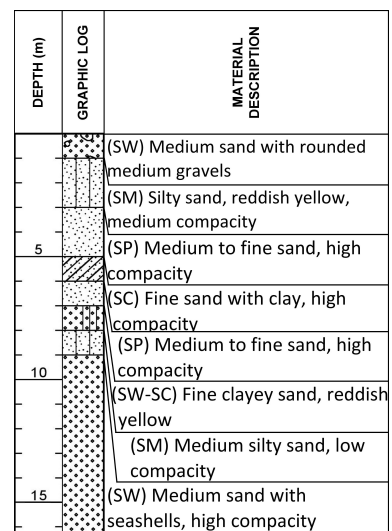
(A)



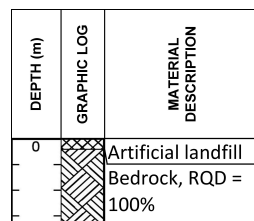
(B) IQ_S_1



(C) IQ_S_2



(D) IQ_S_4



(E) IQ_S_3

FIGURE 4.4: (a) Location of boreholes drilled in Iquique. (b) to (e) Boreholes log. Boreholes IQ_S_1 to IQ_S_3 were drilled during this investigation, whereas IQ_S_4 was provided by a local consultant.

Furthermore, downhole tests were performed for comparison purposes with the shear wave velocity profiles obtained from SWM. Figures 4.6 and 4.5 display the variations between each profiles, it can be noted that both tests are generally well correlated at least for the more shallow layers of soil. Of course, downhole tests were restricted to the drilled depth in each borehole.

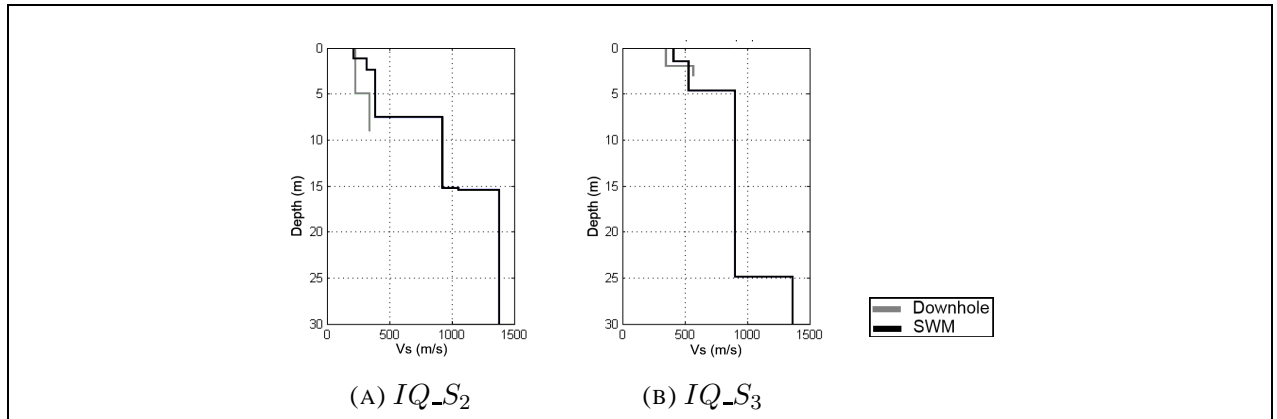


FIGURE 4.5: Comparison of shear wave velocity profiles between available downhole tests and SWM surveys in Iquique.

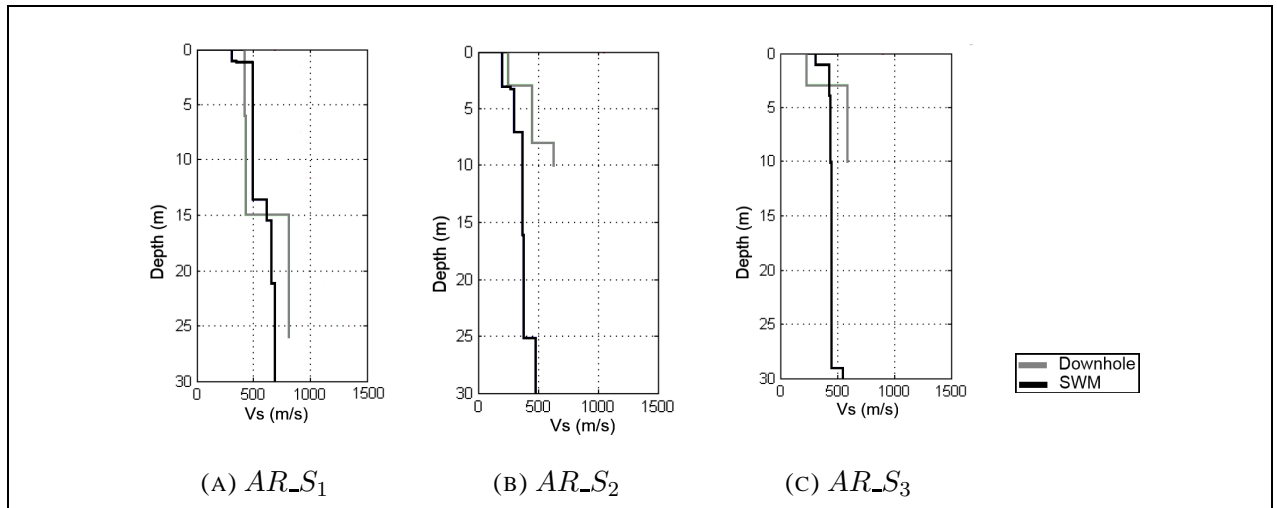


FIGURE 4.6: Comparison of shear wave velocity profiles between available downhole tests and SWM surveys in Arica.

5. MICROZONING

In the previous chapters, several methods for evaluating the dynamic properties of soils were discussed. These properties permit to characterize 1D site effects using microtremor records (Chavez-Garcia, F. J.; Lermo, 1994). All the results of V_s^{30} and F_0 may be found in Appendix A, the respective geophysical acquired data may be found in the electronic Appendix B. Based on these results, the geology and the boreholes information, the scope is to interpret and regroup this information into a map where it is possible to differentiate areas that may be more or less prone to site effects during an earthquake.

Seismic microzoning consists on the urban division of areas that may have a similar dynamic behaviour, in which it can be expected to find ground motion amplification at different scales. The project FONDEF + ANDES D10I1027, funding this research, has previously proposed a preliminary microzoning for Arica (Monetta, 2013) and for Iquique and Alto Hospicio (Podestá, 2013) with a different set of data. The purpose of the current study is to further improve the mentioned maps and propose a final microzoning.

5.1. Arica

The results of the acquired data can be seen in Figures 5.1 and 5.2. The first one displays the fundamental frequencies of Arica, with a size relative to the amplitude A_0 and the color representing the predominant frequencies, F_0 . Note that in each site three HVSR recordings were performed, but only one is shown in the map. Such selection was based on the best fitting curve to the SESAME guidelines (Bard et al., 2004).

Furthermore, Figure 5.2 depicts the value of V_s^{30} for each site, the interval classification assigned for this parameter is based on the current Chilean guidelines (DS61, 2011), that denotes V_s^{30} as a primary parameter to evaluate the dynamic stiffness of a site, and it is calculated as the harmonic average of the S-wave velocity in the first 30 meters of depth;

$$V_s^{30} = \frac{\sum_{i=1}^n h_i}{\sum_{i=1}^n \frac{h_i}{V_{s_i}}} \quad (5.1)$$

Where h_i is the height of each layer and its corresponding shear wave velocity V_{s_i} . This document classifies the soil with 2 parameters, V_s^{30} and q_u , S_u or N_1 , the former value being the unconfined compressive strength of the sample on its undrained shear resistance and the latter is the standard penetration index. Since this data is not available for every site (because of the cost associated to determine such parameters), only V_s^{30} will be used. In order to avoid confusions, lower case letters were used instead of capitals. Figure 5.2 illustrates the values of V_s^{30} and the intervals used.

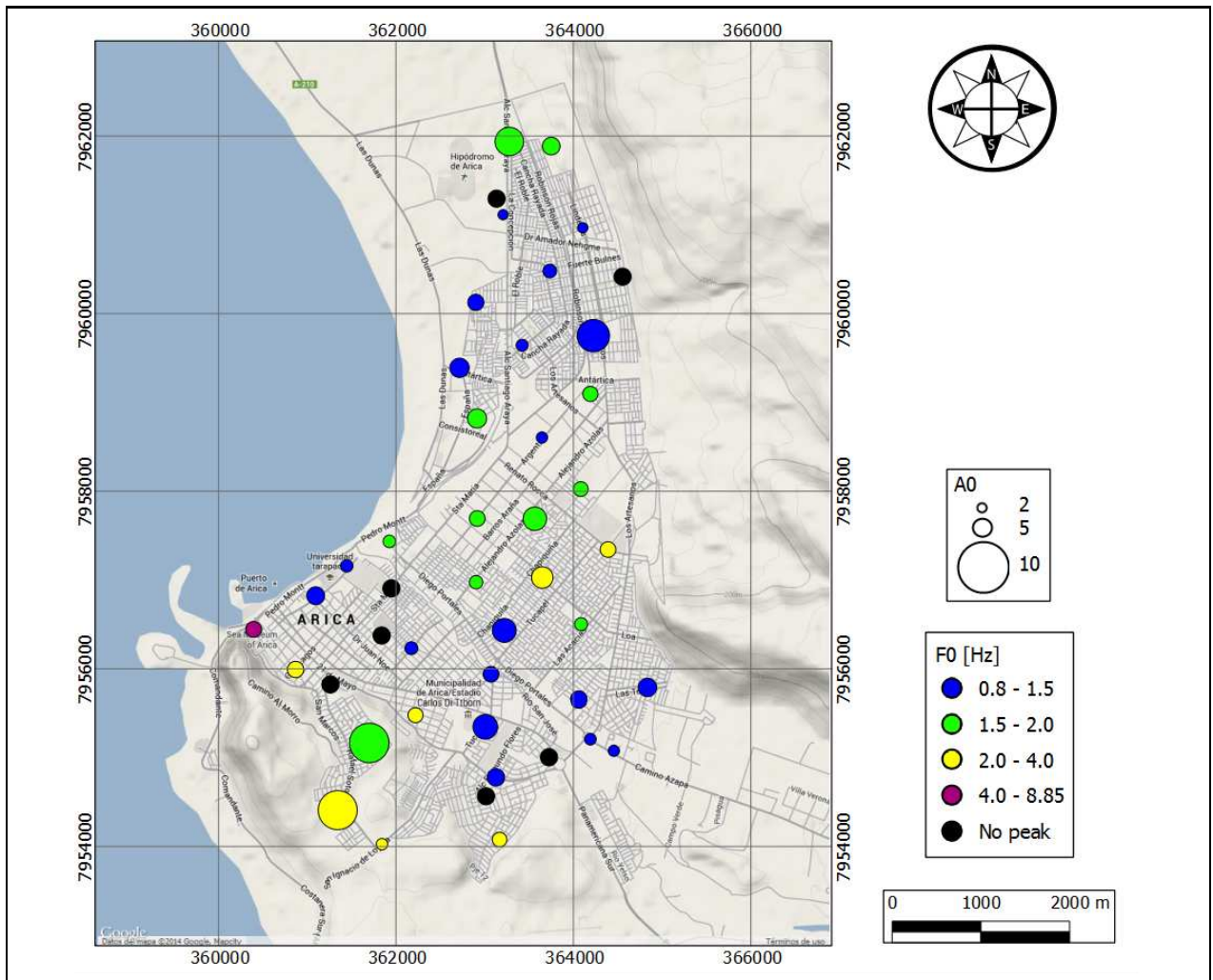


FIGURE 5.1: Map with the computed F_0 through HVSR technique in Arica, the size of the circles represents the amplitude of the result, and the colorbar denotes the fundamental frequencies of each site.

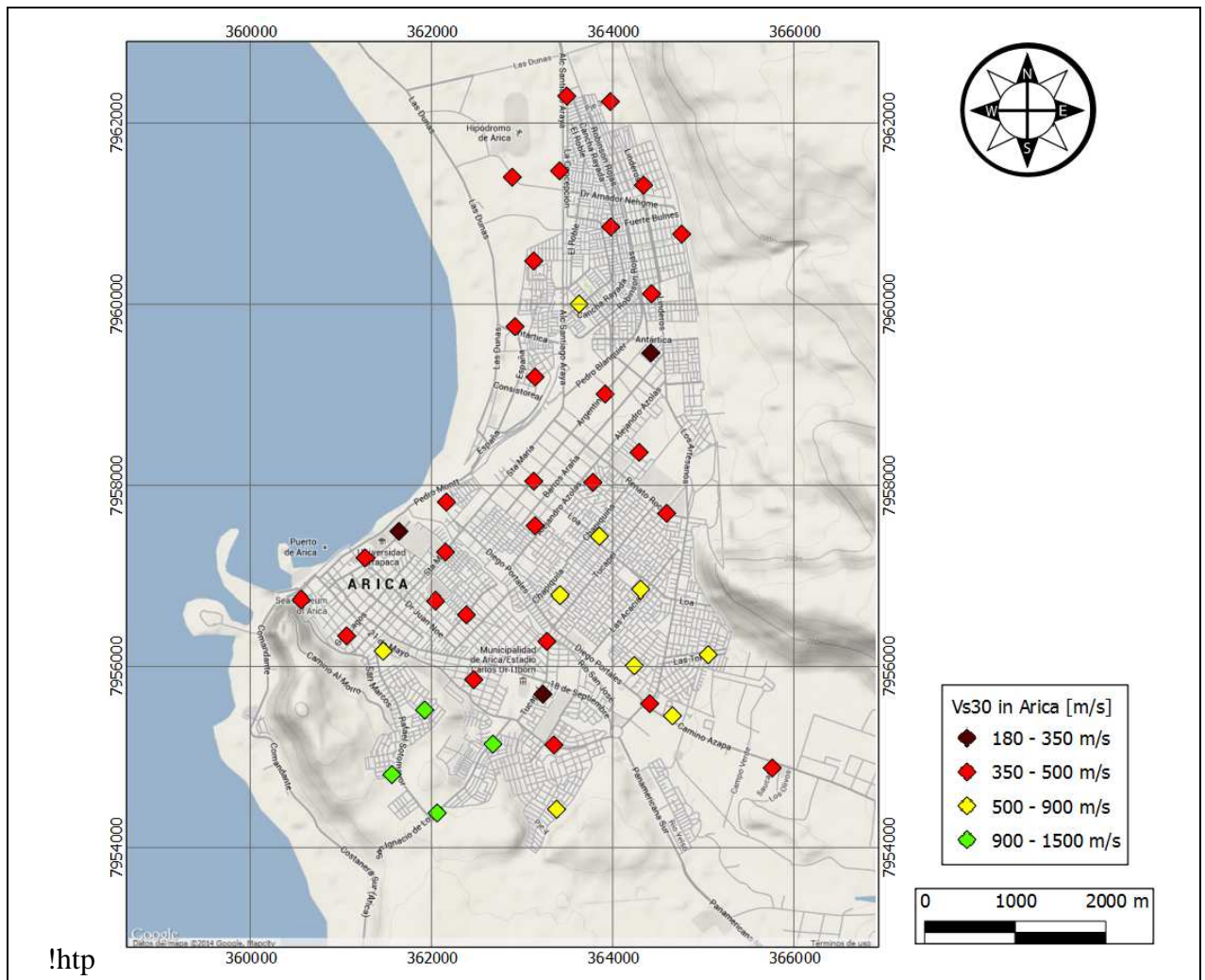


FIGURE 5.2: Map with the computed V_s^{30} in each site of study in Arica. The intervals are inspired on the current Chilean seismic guidelines.

With these results, the scope is to delimit areas within the city where the soil dynamic properties are similar, in order to relate them to seismic soil classes and define zones that could be prone to site effects during an earthquake. The interpretation of the results will be performed from south to north in the following sections.

5.1.1. El Morro Hill

In the southern limit of the urban sector of Arica, El Morro raises as a steep hill of 140 meters height, with an andesitic composition from the Camaraca formation (Figure 2.2a). Typical results in this area are shown in Figure 5.3. It may be seen in the figure the presence of very high values

of V_s^{30} all of them above 900 m/s, and a frequency range between 1.83 and 3.95 Hz, with high amplitudes, indicating the high impedance contrast between materials. These results are consistent with the geology in the region and reveal the predominance of bedrock in the zone.

In the border of the hill, at sea level, tests were performed and low velocities with high

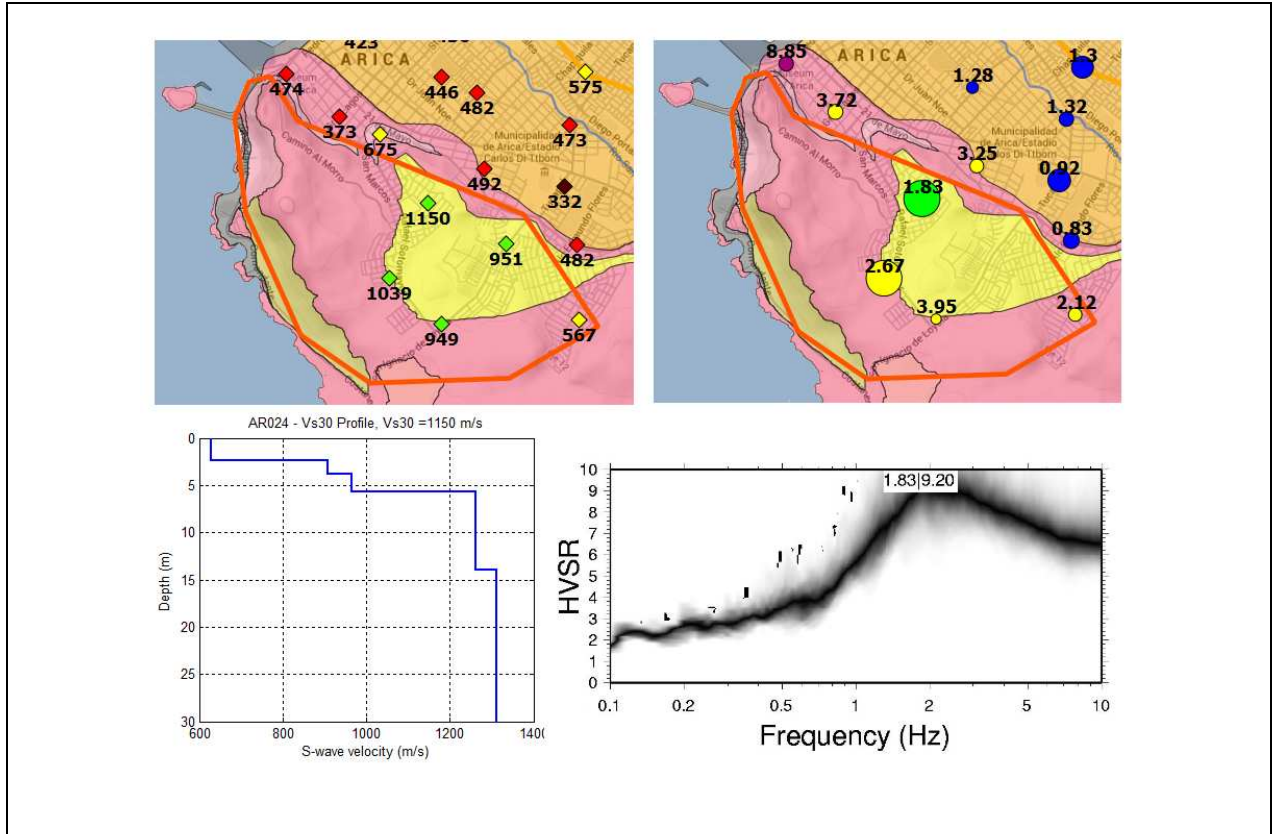


FIGURE 5.3: Values of V_s^{30} and F_0 near El Morro. Typical results of V_s profiles and HVSR computations are shown for the area marked in orange.

frequencies are identified. In this case, geometrical anomalies could affect the HVSR results, and probably the main hypothesis of Nakamura's method (horizontal layers) is not suitable in this case.

5.1.2. San Jose alluvial fan

In the ravine between El Morro and El Chuño Hills the San Jose river is situated. This river is one of the main actors in the construction of this sedimentary basin, since its fluvial deposits cover great part of the city. In this area, the frequencies range between 0.83 and 2.02 with low amplitudes around the river, which denotes no sign of shallow bedrock and a rigid layer of soil. The velocities

range between 350 and 480 m/s towards the coast. To the east, they increase, reaching values of V_s^{30} up to 575 m/s, as Figure 5.4 illustrates.

One borehole was conducted in this area (AR_{S2}). It was drilled near the coast, and it reveals

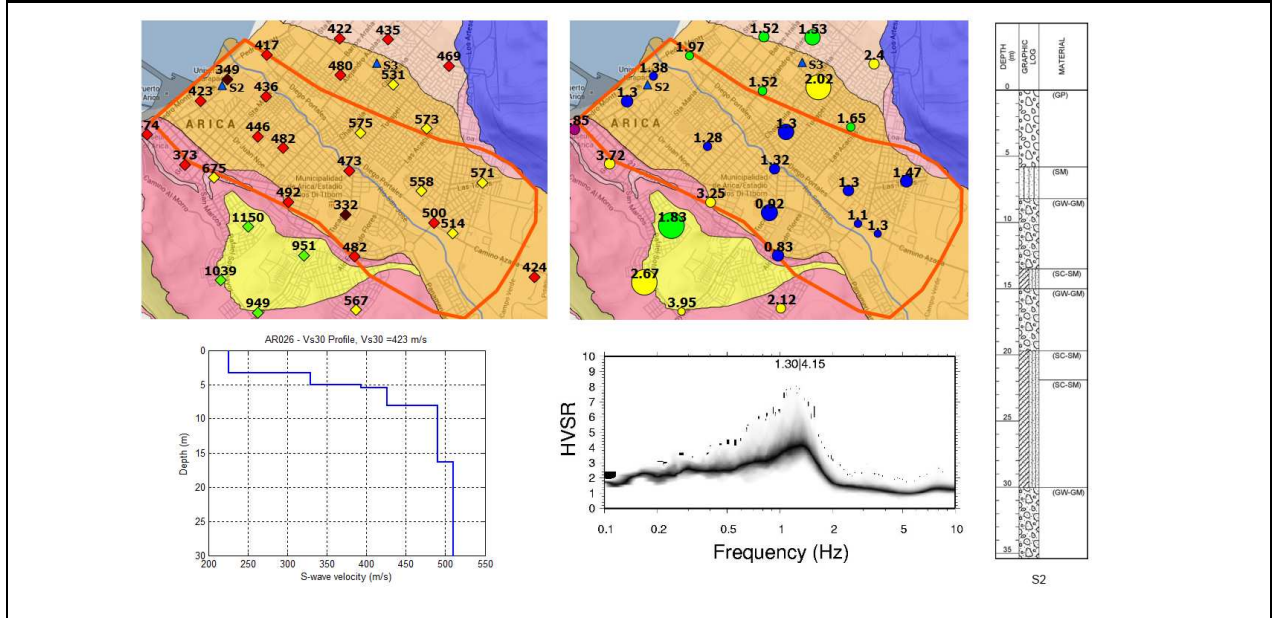


FIGURE 5.4: Values of V_s^{30} and F_0 located near the alluvial fan of the San Jose river. Typical results of V_s profiles and HVSR computations are shown for the area marked in orange.

the presence of coarse to medium rounded gravels, in a matrix of clayey silt, it reached a depth of 35 meters without reaching bedrock. Tests performed on the samples classified the soil as a mix of clay, silt and medium gravel down to 25 meters. Most of the samples were classified as SM (silty sand) and SC (clayey sand).

5.1.3. El Chuño Hill

Towards the north-east section of the delta, near el Chuño hill, the frequencies range between 1.47 and 2.4 Hz, whereas velocities raise up to 575 m/s, indicating the presence of a more rigid soil.

The borehole (AR_{S3}) drilled in this section exhibits layers of a stratified mixture of sand and coarse gravel, reaching a depth of 30 meters with no sign of bedrock. In this area, a combination of the San Jose's alluvial fan and colluvium-covered slopes from the El Chuño hill probably exist,

explaining the higher density of the soil compared to areas closer to the river.

In this zone, it is expected that geometrical anomalies are present because of the slope of the

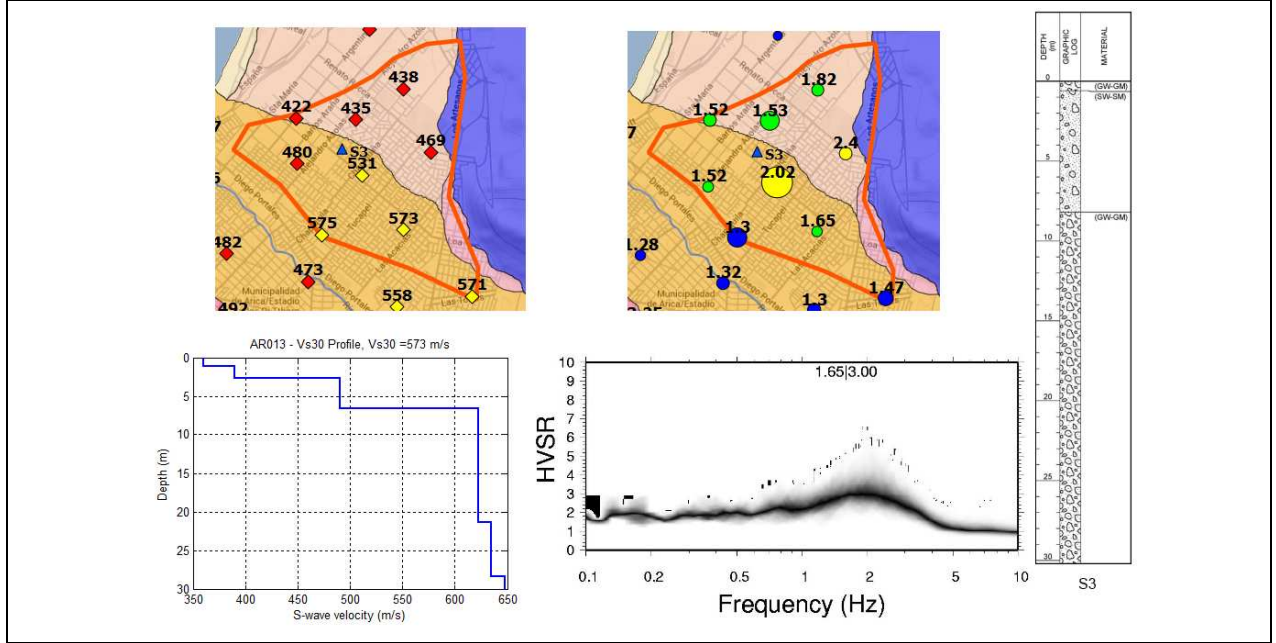


FIGURE 5.5: Values of V_s^{30} and F_0 in the outskirts of the El Chuño Hill. Typical results of V_s profiles and HVSR computations are shown for the area marked in orange.

hill. These irregularities could affect the results in the area and it must be treated with caution.

5.1.4. Northern Side

In the north of the city a residential zone is placed, occupying the whole coastal plain up to the Chuño hill. In this area, the frequency range is fairly homogeneous, fluctuating between 1.2 and 1.6 Hz, with a maximum amplitude of 7.5. The value of V_s^{30} varies between 326 and 565 m/s, but the majority of the studied sites in the zone are close to 400 m/s. The marked area and typical results are illustrated in Figure 5.6.

It is important to note that several HVSR computations in this zone display two peaks, hence, a detailed study of the velocity profile combined with the HVSR results must be carried out, to find which of the peaks represent the predominant mode of the 1-D soil profile.

The borehole drilled in the area shows the predominance of dense sands, down to 30 meters deep. It was not possible to identify the depth of the bedrock with this borehole. Tests performed in all the obtained samples classified the soil as a silty sand (SM).

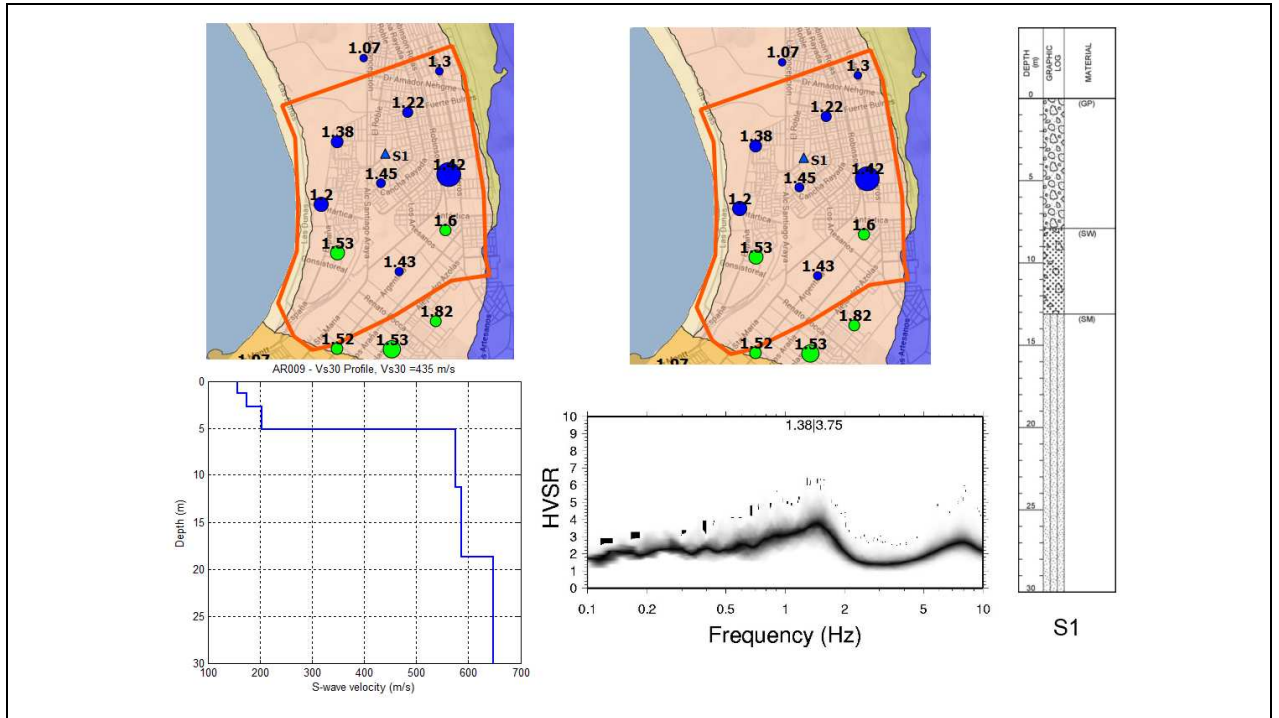


FIGURE 5.6: Values of V_s^{30} and F_0 in the northern suburbs of Arica. Typical results of V_s profiles and HVSR computations are shown for the area marked in orange.

The results are consistent with the geology, that suggests the main actors of this formation are eolian deposition and sea transgressions and regressions, combined with colluvium-covered slopes from the El Chuño hill, which implies the presence of sand and not gravels from the San Jose's river deposition. This also explains the relative low velocities in the area.

5.1.5. Urban Northern Limit

In the northern limit of Arica relative low velocities are detected, with a V_s^{30} varying between 381 and 481 m/s. Nevertheless, frequencies are more heterogeneous, with a wide range of amplitudes (Figure 5.7).

No boreholes were drilled in this area and velocity profiles were not able to reach the bedrock. As geology shows, in this area the existence of El Lluta's alluvial fan and the presence of diatomite deposits may incide in the soil conditions in the area, making this region slightly different to the south.

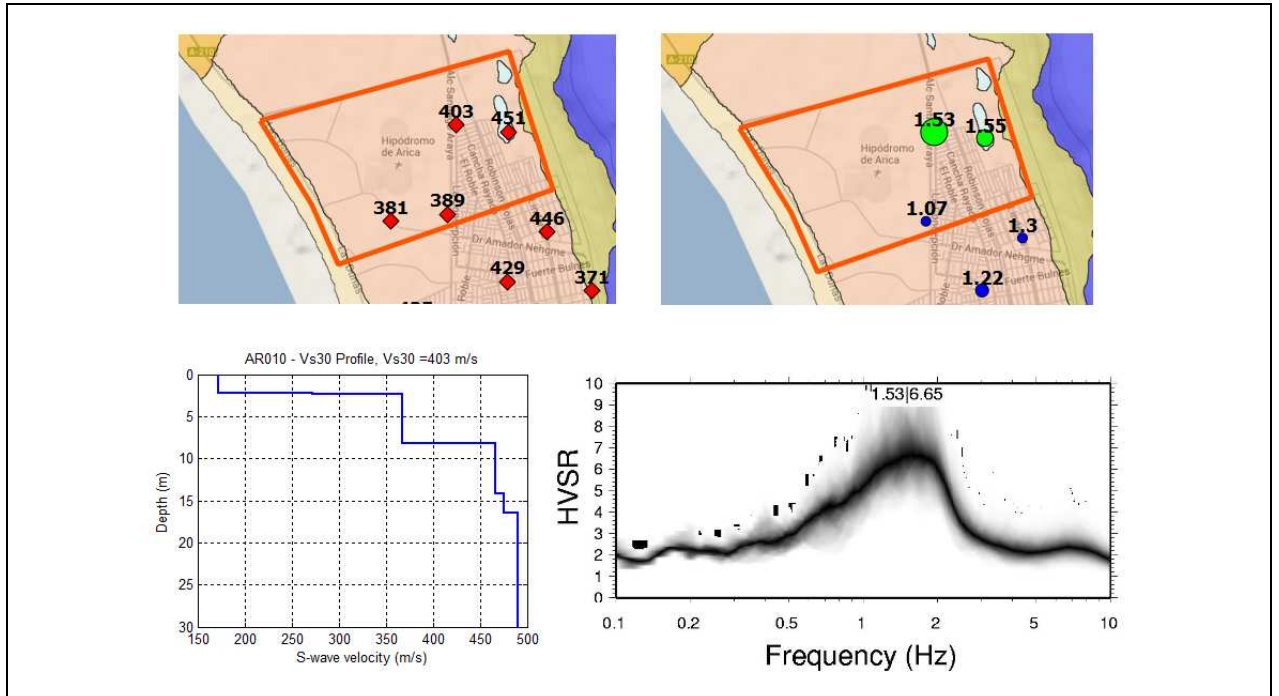


FIGURE 5.7: Values of V_s^{30} and F_0 towards the northern limit of Arica. Typical results of V_s profiles and HVSR computations are shown for the area marked in orange.

5.1.6. Microzoning Definition

Once the main units have been identified, a map differentiating the areas previously described is constructed. A preliminary seismic microzonation was already performed by Monetta (2013) through geology background and geophysical surveys. Figure 5.8 displays the different areas defined by this author. As it can be seen, the delimitation of the areas is fairly similar to the ones described in this research. An improvement to the existing map of Monetta with the obtained data from geophysics, geology and boreholes is proposed.

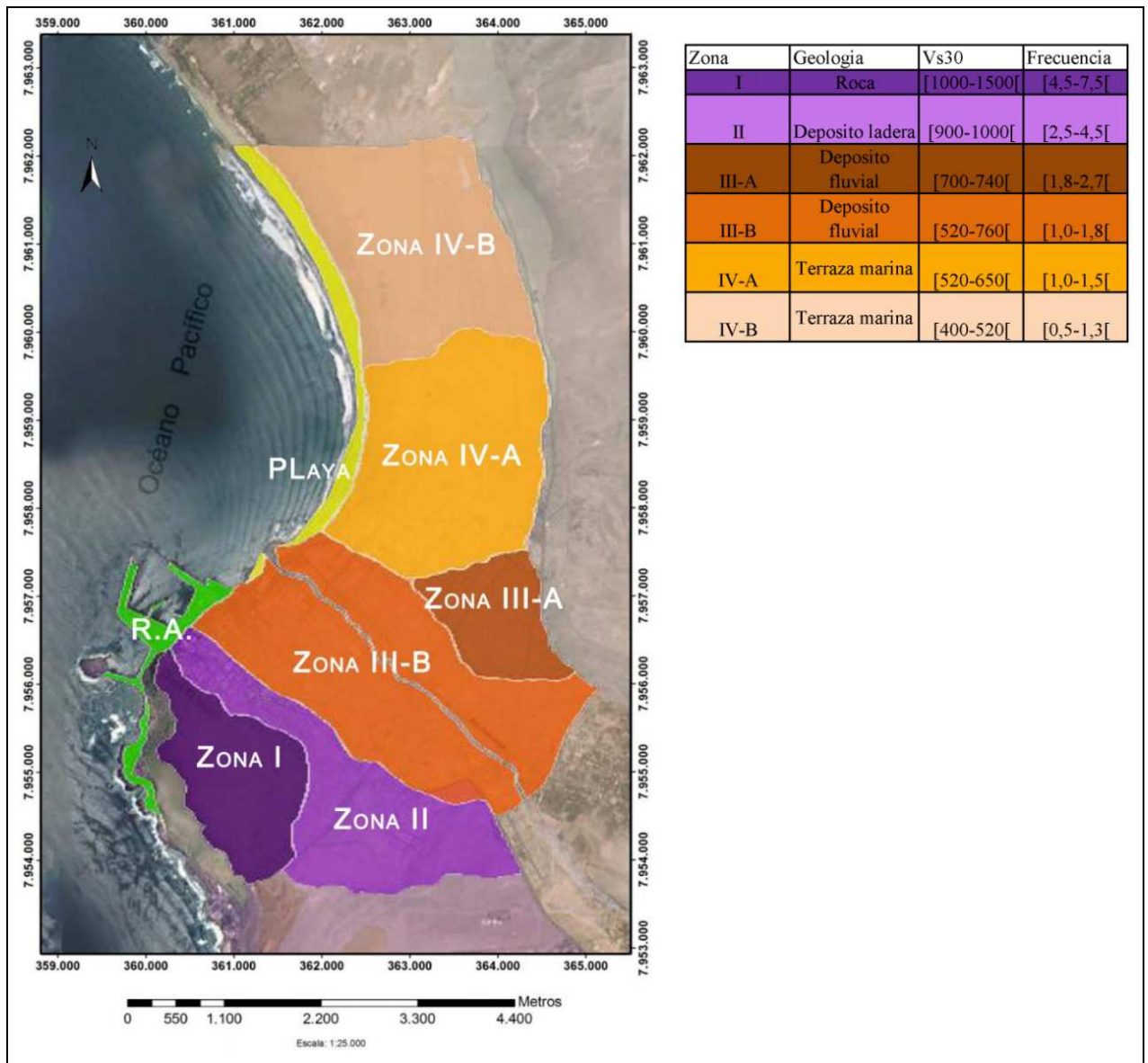


FIGURE 5.8: Preliminary microzonation of Arica defined by Monetta (2013).

Essentially, one of the main modifications would be to extend the area near El Chuño hill, since according to the HVSR results this zone seems to be larger towards the west and north. Another area of interest is north of Arica where anomalies in terms of HVSR are noticed, nonetheless, this is noticeable a bit more to the north than the delimitation defined by Monetta. Also, the peninsula west of the El Morro hill is now defined by the same unit as the hill, the evidence of bedrock in the area was seen during fieldwork and is rectified by the geological map defined by Maldonado

(2014).

Another significant modification is the elimination of the zone denoted as "beach", since this is not a proper definition of a dynamic site characteristics and its composition should be the same as to the east. Finally, most of the limits are redefined in order to follow streets or milestones within the urban area, while maintaining the consistence of the maps. Figure 5.9 illustrates the new identified zones with their description, the colors were chosen in order to visualize the areas more prone to exhibit site effects in red colors. As it can be seen, the north area of Arica is the one most susceptible to be affected by soil amplification, because of the lack of gravels, low velocities, and depth of bedrock based on HVSR technique.

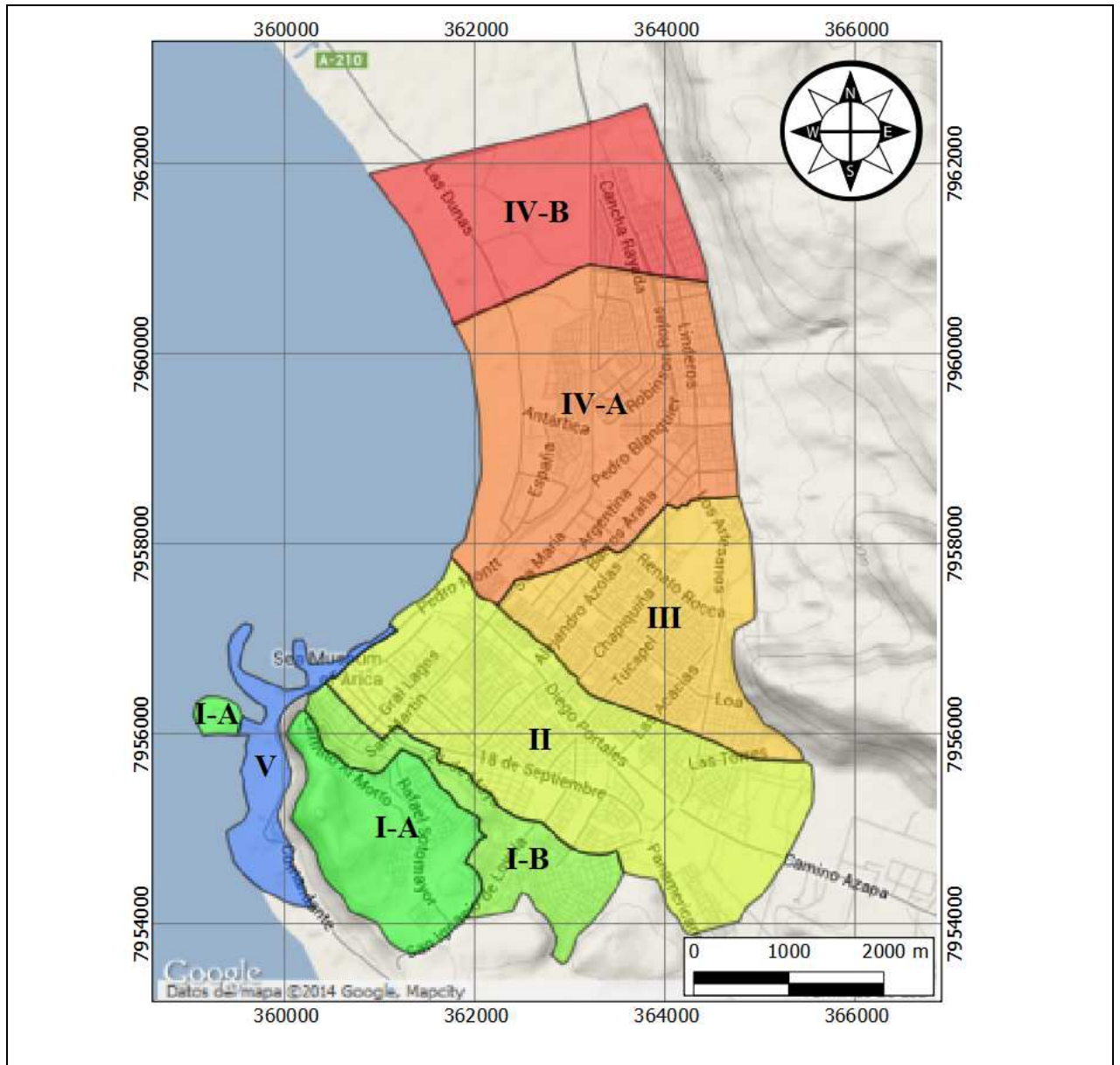

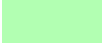







FIGURE 5.9: Final seismic microzoning of Arica. The colors indicate the susceptibility of soil amplification in the area, from green denoting no or low amplification, yellow is medium site-effects and red indicating high expected site effects. The blue represents artificial landfills, where a more detailed study should be performed.

5.2. Iquique

The results of the geophysical surveys in Iquique are shown in Figures 5.10 and 5.11. In the same way as Arica, F_0 is classified by color and size based on its value and amplitude, respectively,

TABLE 5.1: Detailing of the zones delimited by Figure 5.9.

Color	Zone	Avg. V_s^{30} [m/s]	Freq. range [Hz]	Description
Arica				
	I-A	1093 ± 118	$[1.83 - 5.32]$	Predominance of bedrock, composed of andesite and limestone deposits.
	I-B	623 ± 202	$[2.12 - 8.85]$	Foot of the hill composed of alluvial deposits. Bedrock is located between 5 to 20 meters deep.
	II	462 ± 65	$[0.92 - 1.97]$	Fluvial deposits, consisting of rounded coarse gravel in a matrix of sand and silt, bedrock at deep levels.
	III	530 ± 89	$[1.3 - 2.4]$	Foot of el Chuño Hill, mixture of river deposits and gravels from the hill, bedrock at deep levels.
	IV-A	409 ± 55	$[0.91 - 1.6]$	Marine deposits, composed of mostly fine sand. Bedrock at deep levels.
	IV-B	423 ± 38	$[1.07 - 5.43]$	Mixture of marine deposits and diatomite, bedrock at deep levels.
	V	—	—	Artificial landfill from the port of Arica.

while V_s^{30} is categorized according to the Chilean seismic guidelines. Following sections will describe each recognizable zone in detail. Figure 5.10 includes some data collected during a post-even survey performed after Iquique $M_w = 8.2$ earthquake, while Figure 5.11 includes additional surveys performed in the port of Iquique on the framework of the SATREPS-Chile project.

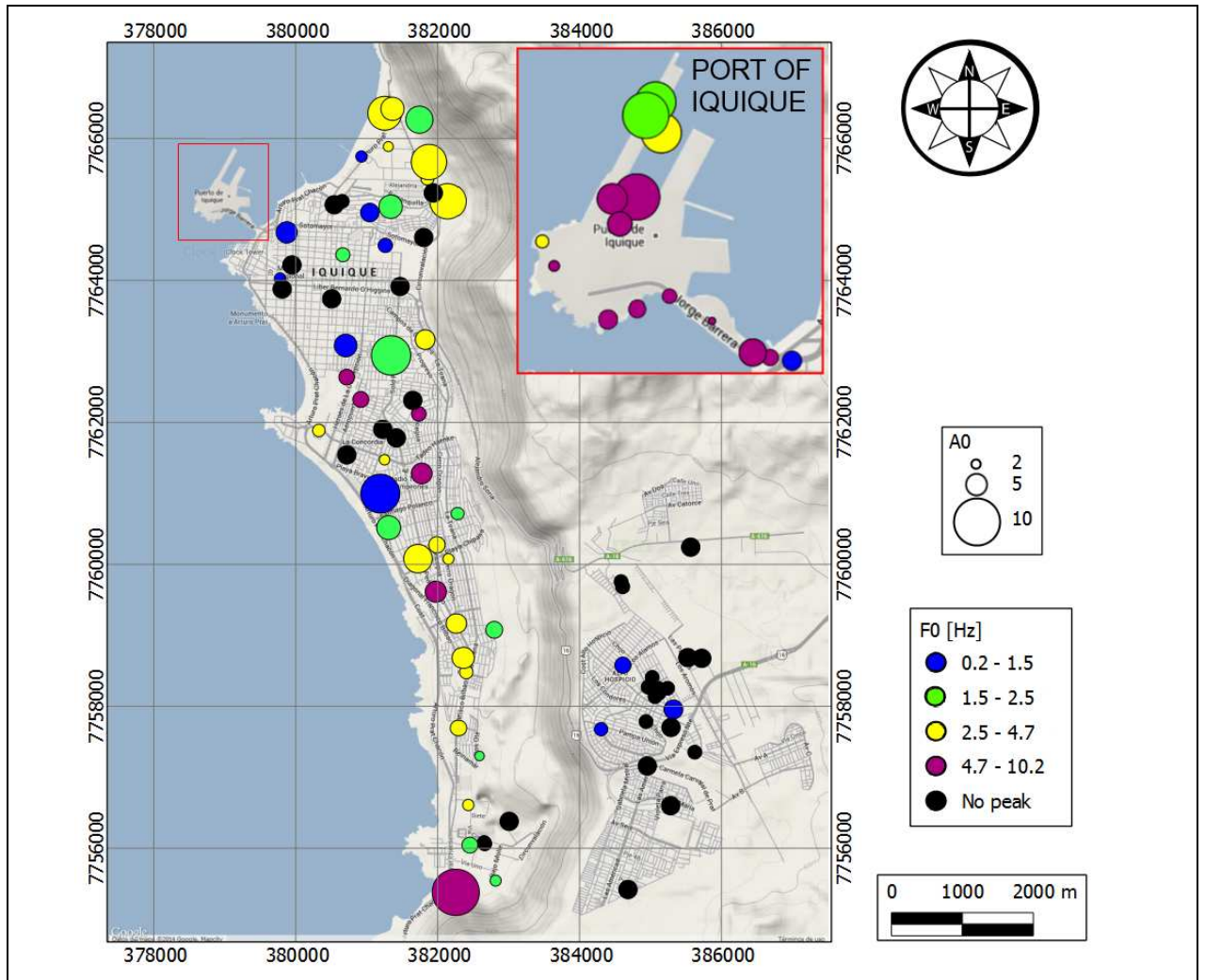


FIGURE 5.10: Map with the computed F_0 through HVSR technique in Iquique, the size of the circles represents the amplitude of the result, and the colorbar denotes the fundamental frequencies of each site.

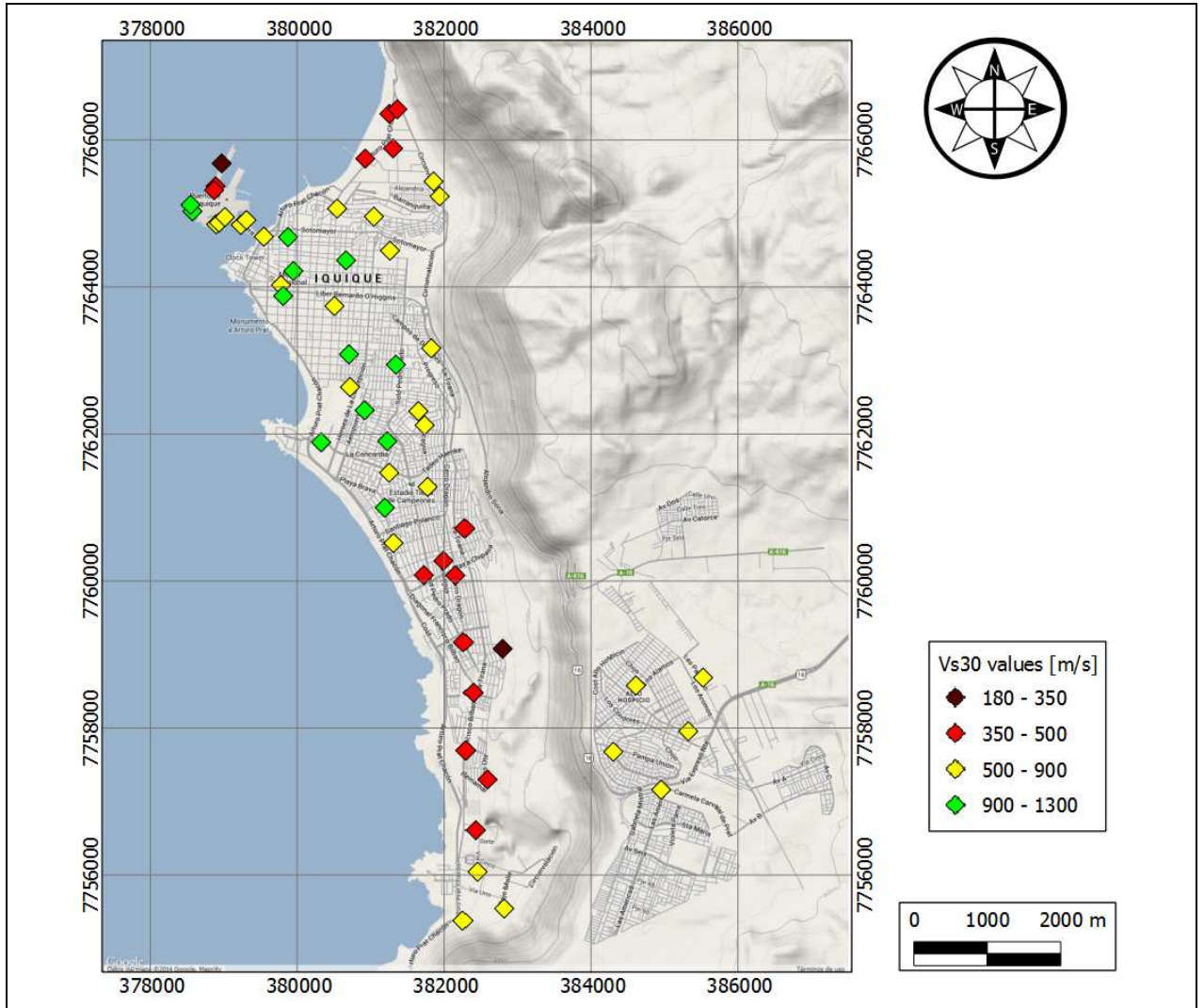


FIGURE 5.11: Map with the computed Vs30 in each site of study in Iquique. The classification is based on the DS 61.

5.2.1. ZOFRI Area

This area is situated north of the ZOFRI fault, displayed in a dotted blue line in Figure 5.12. It is characterized for being an industrial zone with a lot of commerce and warehouses. The geology identifies 2 lithological units, and hence this zone is differentiated between the east and west. The west side has lower velocities ($V_{s30} \approx 460 \text{ m/s}$) and a wide predominant frequency range, between 1.35 and 4.1 Hz. Also, no sign of bedrock is recognized in the velocity profiles. Nonetheless, towards the east the velocities increase while F_0 remains high. The velocity profiles indicate the location of bedrock at 25 meters approximately. The slope of the hill east of the zone may have

significant effects on the results in the east part, so the information must be treated with caution. In both cases, the HVSR computation show a clear peak, satisfying the SESAME criteria.

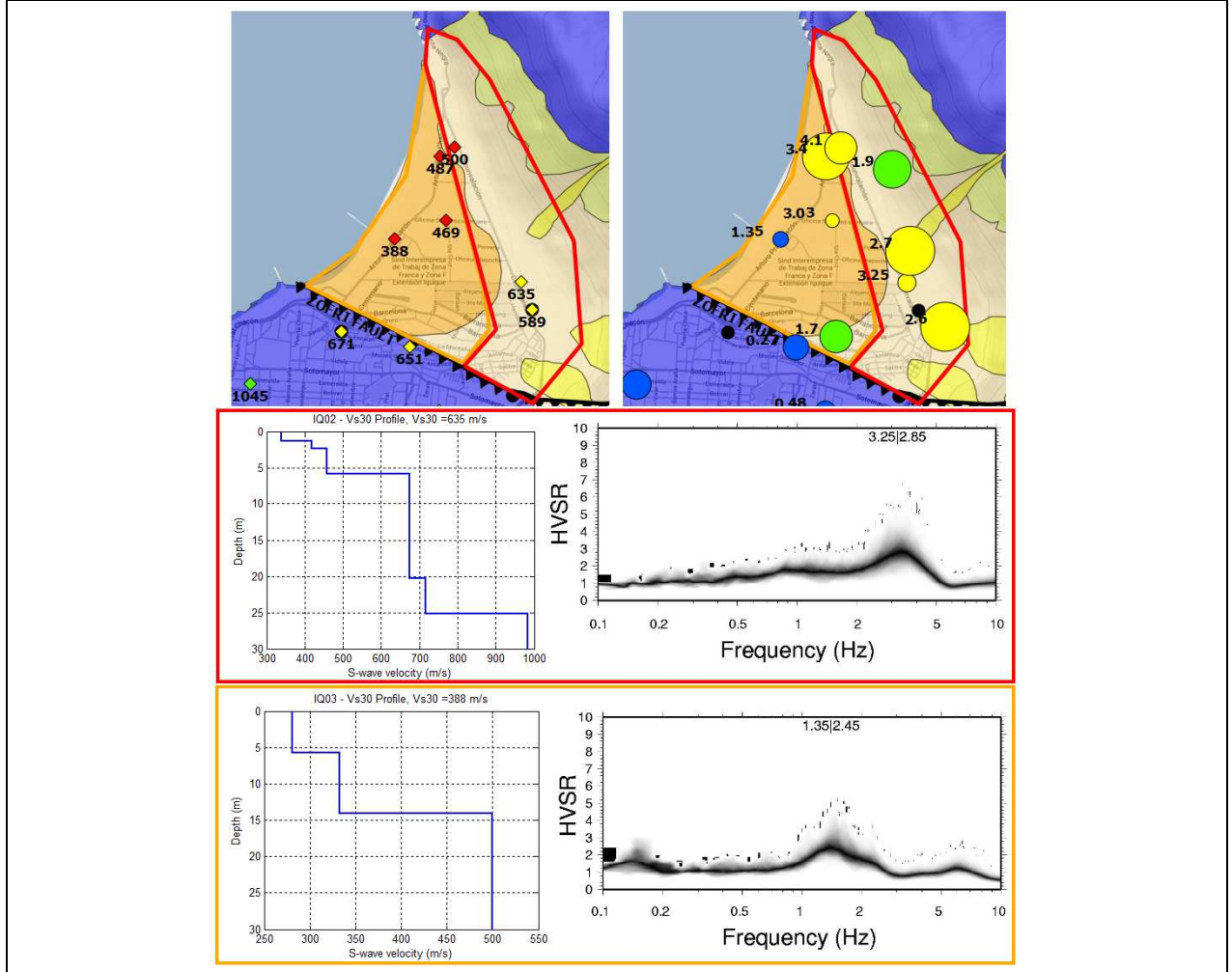


FIGURE 5.12: Values of V_s^{30} and F_0 towards the northern limit of Iquique (ZOFRI). The dotted blue line denotes the ZOFRI fault, while the orange line marks the referenced area of study

5.2.2. Town Center

The center of the city shows high velocities in general, but a very heterogeneous behaviour in terms of F_0 and hence it is important to analyse it altogether with the geology in the area, as shows Figure 5.13. The figure illustrate the values F_0 , V_s^{30} , the location of the 3 boreholes drilled in the city, and the main geological units. The geology in the area shows 2 main units, the blue one denotes shallow bedrock, composed by a volcanic rock of El Barranco Formation and the yellow

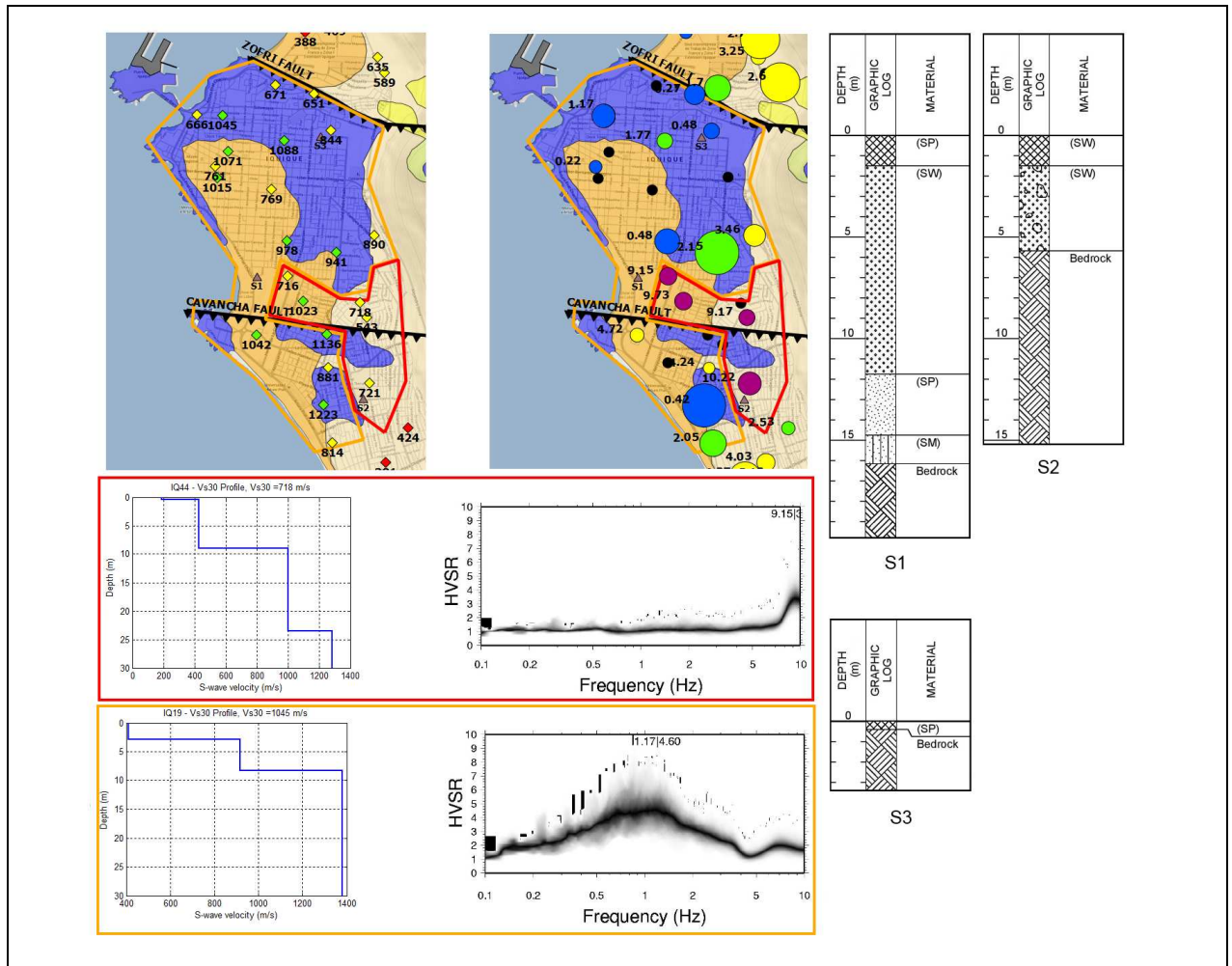


FIGURE 5.13: Values of V_s^{30} and F_0 in the town center of Iquique. Typical results are shown for the red marked area and the orange marked area. The dotted blue lines represent the existing faults, in this case, the Cavancha fault.

unit consists of marine deposits. The figure divides the center in 2 areas, based on the significant difference indicated by the frequency range. The red marked area is characterized by very high frequencies, all of them above 9 Hz, whereas the orange one has low frequencies, ranging between 0.27 to 4.72 Hz. The velocities all along the area are quite high, indicating bedrock at a very shallow depth.

All the boreholes were drilled around the center of the city, as Figure 5.13 indicates. The main characteristics of the boreholes are the following:

1. IQ_{S1} : Fine sand is found until a depth of 14 meters, then a shallow layer of silty sand appears between 14 and 16 meters deep, until bedrock is reached.
2. IQ_{S2} : The presence of fine sand predominates until reaching bedrock at a depth of 5.7 meters.
3. IQ_{S3} : Rock is found at 0.5 meters deep, the first 50 centimetres are mainly characterized by sand and gravel.

This data confirms the predominance of bedrock in the zone, but it is important to indicate the shallow layer of sand that is found in some places. The results of the geophysical surveys and the boreholes are consistent with the available geology maps defined, except for the area towards the coast, where HVSr shows mainly very stiff sites, while the geology suggests a surface consisting of marine deposits, probably of thin thickness.

5.2.3. Dragon Hill

South of the town center the existence of the Dragon Hill dominates the topography of the zone, which tends to be steep as it gets closer to the east. The values of V_s^{30} are considerably low compared to the center town area, ranging between 320 and 470 m/s, while the values of F_0 have a slight variation from east to west. In the east area, they are of about 2.5 Hz, while to the west they tend to be higher, reaching frequencies as high as 4.52 Hz. No boreholes were drilled in this area, but geophysical surveys show no sign of bedrock in the first 30 meters.

The geology of this area is characterized by eolian deposits, which is consistent with the low velocities computed on the upper part of the explored sites, typical of a loose sand. Below 5 meters in average, the velocities suggest a denser sand with probably some degree of cementation.

5.2.4. Southern limit

The southern limit is characterized by higher S-wave velocities, fluctuating between 564 and 672 m/s, and a varied range of frequencies with different amplitudes, as it can be seen in Figure 5.15. Also the Molle fault goes across the area, which could translate into geometrical anomalies that may perturb the information of the geophysical surveys, specially the HVSr results. This area is considerably more rigid than the previous one. The geological map indicates the presence of

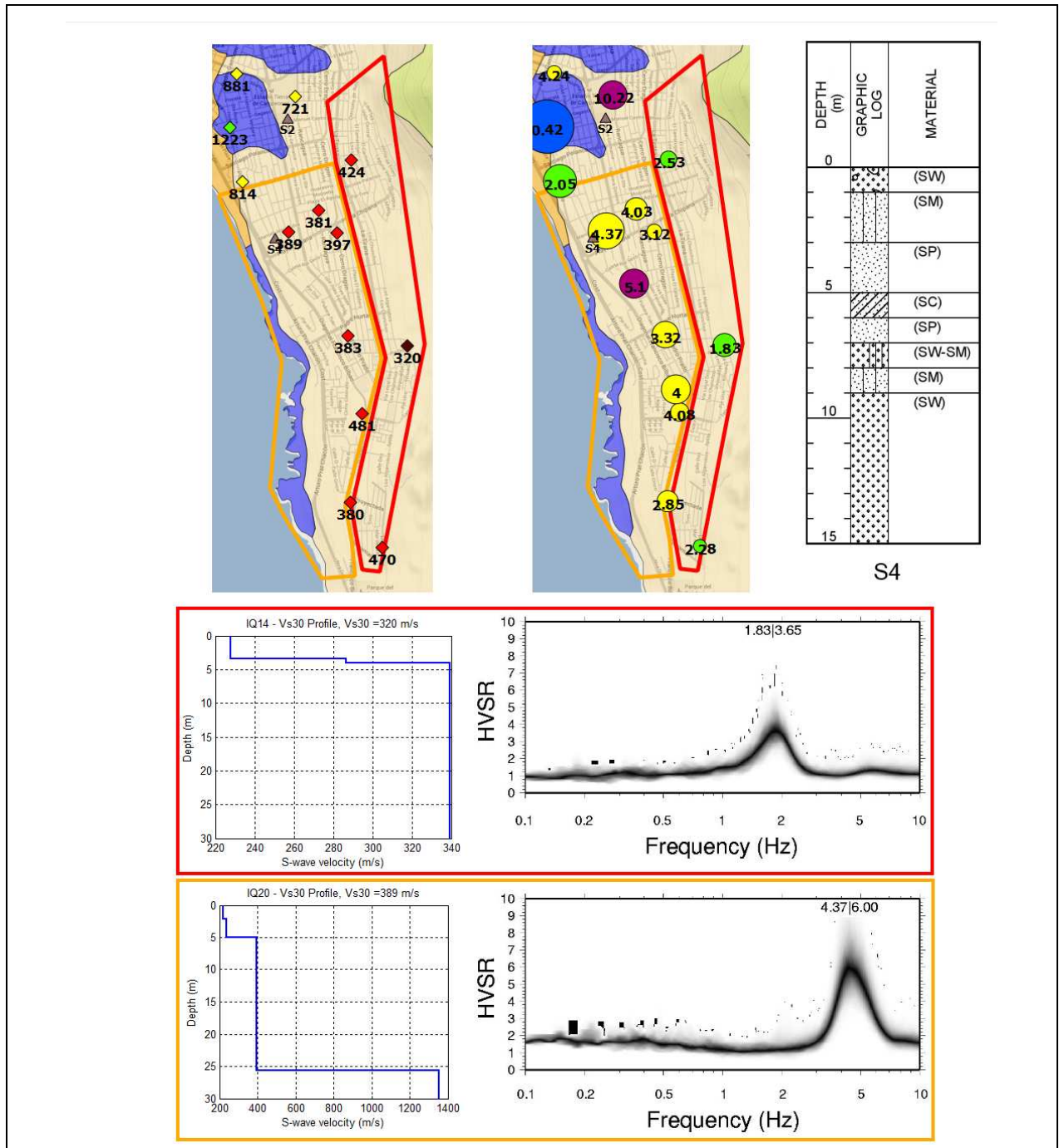


FIGURE 5.14: Values of V_s^{30} and F_0 in the southern residential area of Iquique, near the Dragon hill.

alluvial deposits, consisting of gravels, sand and silt, which are in agreement with the higher V_s^{30} found in the zone.

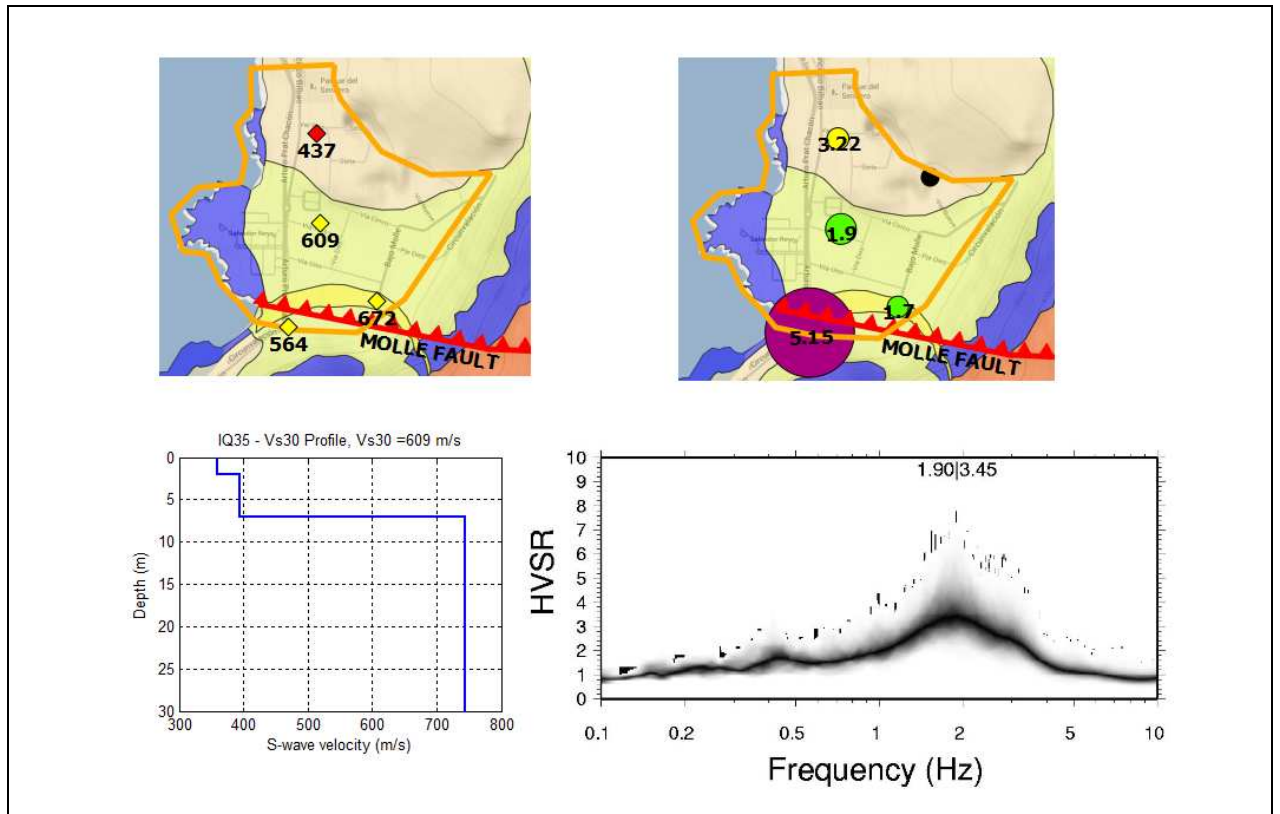


FIGURE 5.15: Map with the computed results in the southern limit of Iquique.

5.2.5. Port of Iquique

In the port of Iquique, there are significant differences in the acquired data (Figure 5.16). Towards the north side, relatively low velocities are found with a frequency range between 2.42 and 5.74 Hz. The shear wave velocity profile indicates bedrock at a depth of 10 meters approximately, whereas the geology defines this area as artificial landfill. Towards the south, the velocities increase notably, and frequencies reach values as high as 9.79 Hz. This part is defined mostly as bedrock, keeping the consistency with the available geological data.

5.2.6. Alto Hospicio

In the area of Alto Hospicio, adjacent to Iquique to the east, the results are fairly homogeneous. Generally large velocities are detected, but only in a few cases a predominant frequency was identified at around 1.2 Hz. Note that in the majority of the HVSR computations the spectrum is mainly plain or with low amplitudes, which is a sign of the low impedance contrast between the

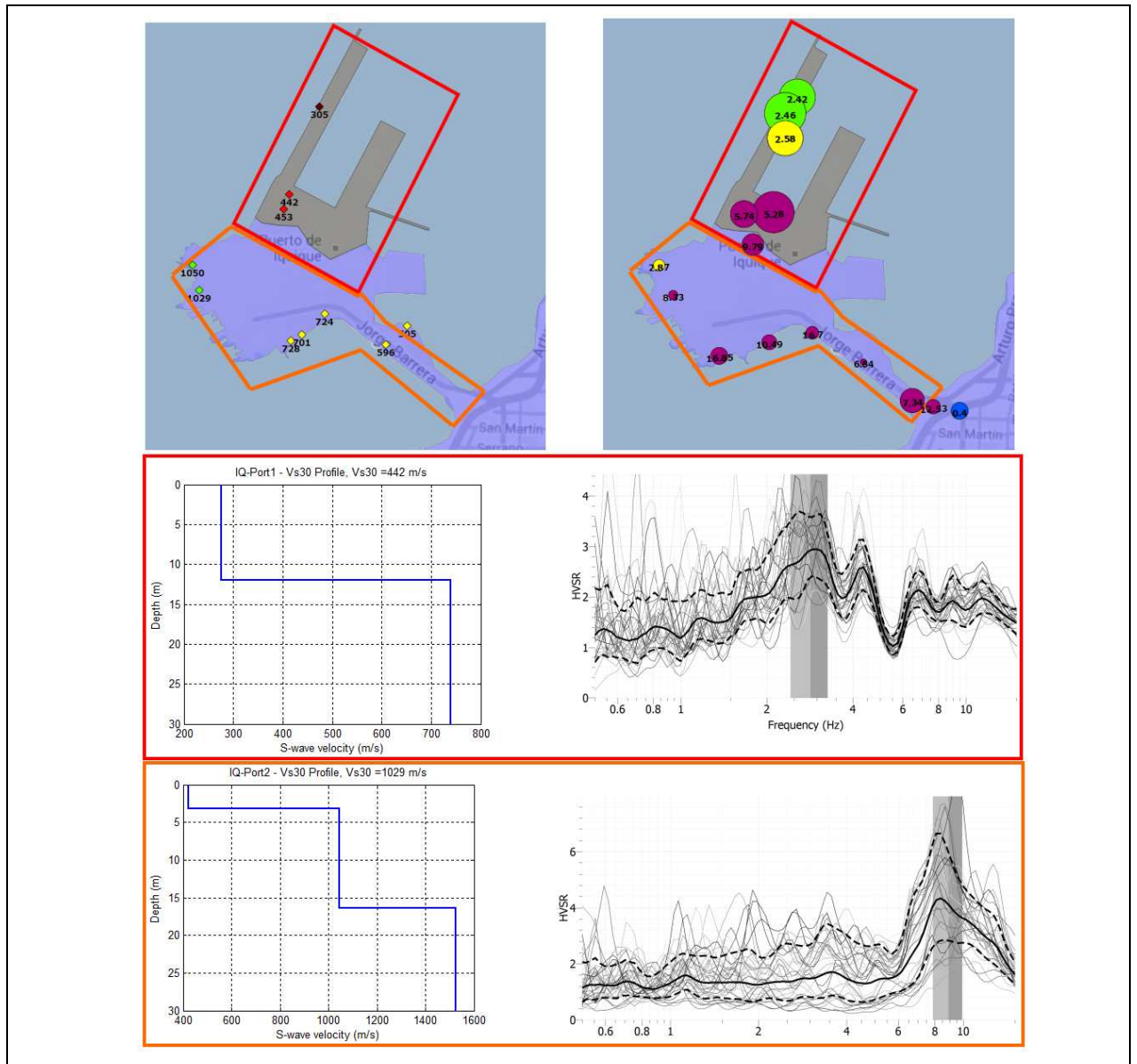


FIGURE 5.16: Map with the computed results in the port of Iquique.

Alto Hospicio rigid material and the bedrock below, hence, it can be deduced that the predominant soils in this city are mainly stiff.

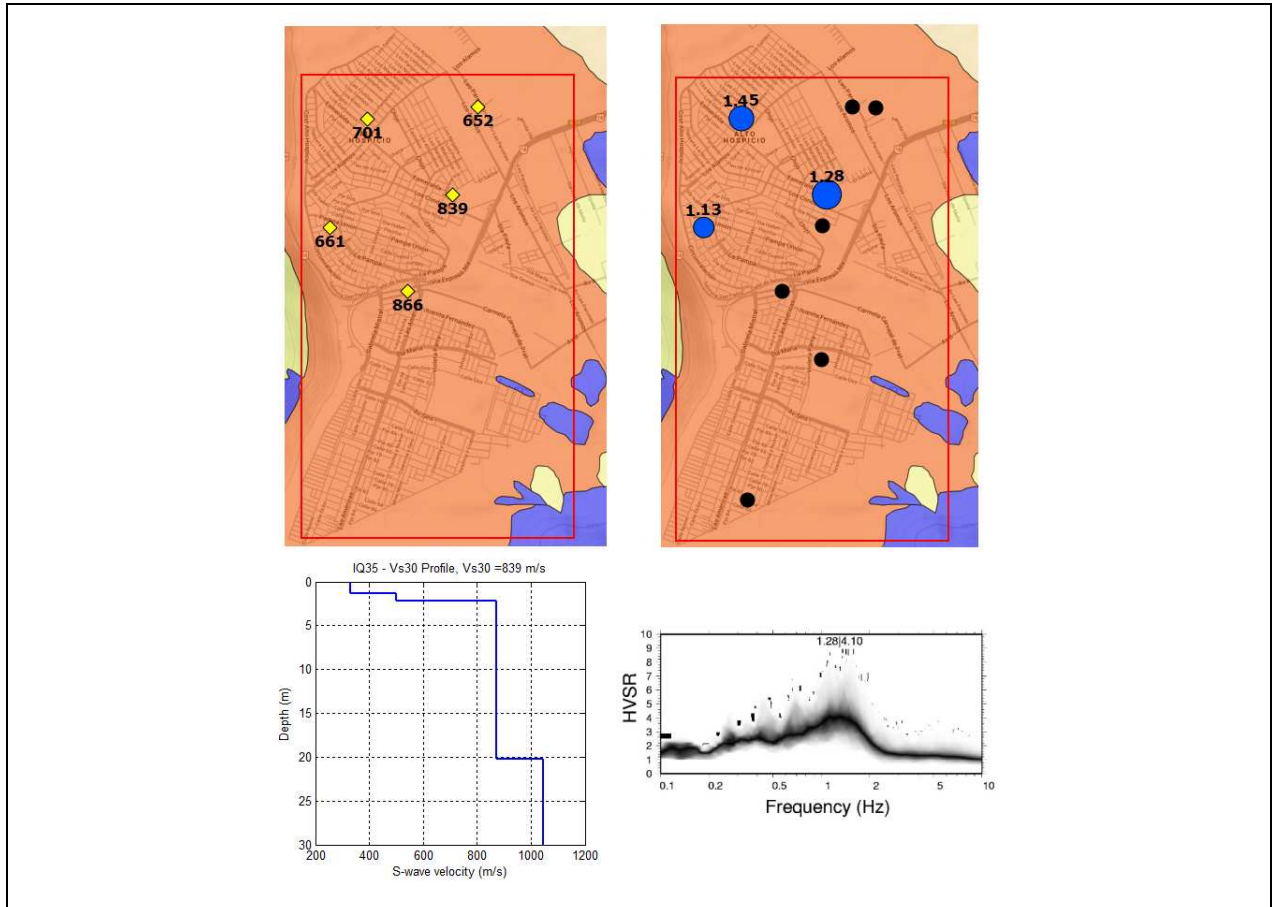


FIGURE 5.17: Map with the computed results in Alto Hospicio.

5.2.7. Microzoning Definition

The preliminary map proposed by Podestá (2013) can be seen in Figure 5.18. The situation is fairly consistent to the obtained results from this research. Nevertheless, there are some aspects that can be revised in the delimitation of the center of Iquique, based on the geological background of the city. Geology defines a sedimentary deposit to the west of the center, however, this was not identified by either the HVSR technique or the S-wave velocity profiles. Instead, the results show bedrock at 3 or 4 meters deep. Hence, this area will be defined as bedrock. One modification proposed to the map of Podestá is the extension of the southern area of bedrock (Figure 5.13), considering the high value of the V_s^{30} in the site IQ17 and a predominant frequency consistent to the others in the same area.

Another zone of interest is the border of the Dragon Hill, on the south of the city. Podestá (2013)

defines a thick fringe bordering the hill, however, the results of this research suggests a thinner perimeter, defined by the results of the HVSR technique and the geology of the zone.

Also, and like Arica, the delimitation of areas tried to follow roads or milestones within the

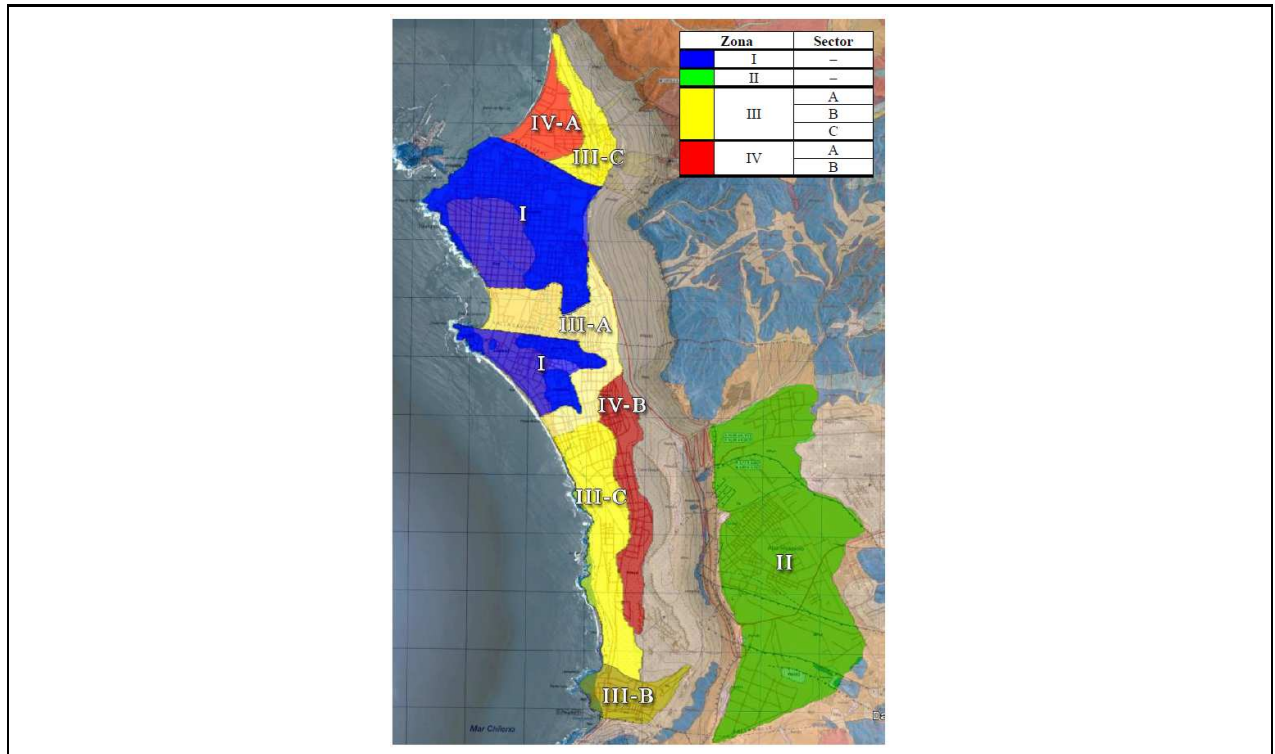


FIGURE 5.18: Preliminary microzonation performed by Podestá (2013).

city, while keeping the consistence of the results, for a better visualization of the areas and definition for public use. Consequently, a final microzonation is proposed in Figure 5.19, with the proposed modifications.

5.3. Microzoning Discussion

The previous sections displayed the subdivision of zones in the cities of Arica, Iquique and Alto Hospicio according to their susceptibility to site-effects. As it could be seen, the areas that are most prone to soil amplification are:

1. The ZOFRI area in Iquique, identified by the zones III-A and III-B in Table 5.2. This case is interesting because zone III-B has a higher V_s^{30} and high amplitudes, suggesting the presence of bedrock at a moderate depth. However, it is classified as more prone to

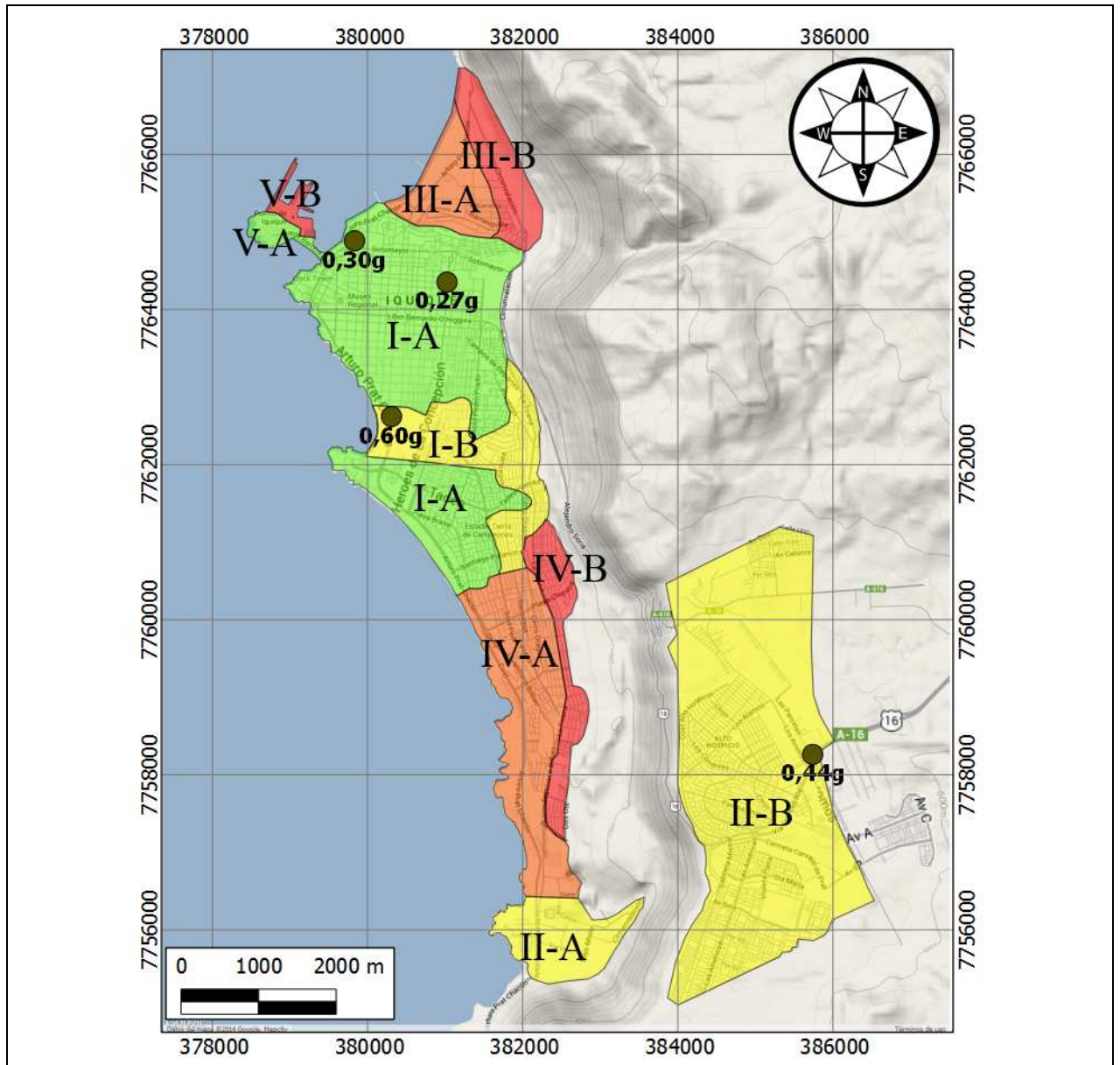












FIGURE 5.19: Proposed microzonation of Iquique. The colors indicate the susceptibility of motion amplification in the area, from green denoting no or low amplification, yellow is medium expected site effect and red indicating high susceptibility to site effects. The peak ground accelerations (PGA) of the A01-2014 event are also displayed.

site effects because the layer overlying the bedrock has lower shear wave velocities in average than zone III-A, and the steep slope characterizing this zone makes this area more susceptible to landslides and topographic effects due to focusing and/or scattering effects around crests and hills (Pilz et al., 2010). It is interesting to note that in these cases the

TABLE 5.2: Detailing of the zones delimited by Figure 5.19.

Color	Zone	Avg. V_s^{30} [m/s]	Freq. range [Hz]	Description
Iquique				
	I-A	872 ± 183	$[0.22 - 1.77]$	Andesite outcrop.
	I-B	768 ± 166	$[3.46 - 10.22]$	Marine and eolian deposits, bedrock located at 5 to 15 meters deep.
	II-A	577 ± 86	$[1.7 - 5.15]$	Colluvial deposits, bedrock located at 5 to 15 meters deep.
	II-B	709 ± 108	$[1.13 - 1.45]$	Gravels from Alto Hospicio, stiff layer of gravels of about 15 meters until bedrock.
	III-A	461 ± 50	$[1.2 - 7.6]$	Marine deposits, bedrock at deep levels.
	III-B	612 ± 35	$[3.25 - 4.1]$	Eolian and marine deposits, bedrock is located about 25 meters deep.
	IV-A	403 ± 38	$[3.03 - 4.68]$	Eolian deposits of over 30 meters deep.
	IV-B	379 ± 48	$[1.83 - 2.86]$	Eolian and alluvial deposits from El Dragon hill, consisting mostly of fine sand, bedrock at deep levels.
	V-A	762 ± 205	$[6.84 - 16.85]$	Andesite outcrop in the port of Iquique.
	V-B	393 ± 78	$[2.46 - 5.74]$	Artificial landfill from the port of Iquique.

sole use of V_s^{30} may not always be descriptive enough regarding the site amplification of a site.

2. The southern area in Iquique, by El Dragón Hill, identified as IV-A and IV-B, composed of a deep layer of sediments, since bedrock was not identified in any of the profiles, it is possible that its depth surpasses the 50 meters. Hence, it would be interesting to further analyse this zone in order to find the real thickness of the deposits in this area.
3. North of the port of Iquique, composed mainly of artificial landfills of low compacity, tagged as V-B (Figure 5.19). Since these fillings are probably saturated, dynamic compaction or even liquefaction could take place for major events in this area.
4. North of Arica is identified in Table 5.1 as the zones IV-A and IV-B. Note that zone IV-B contains a wide range of frequencies, this may suggest the existence of singularities. Also note that the available geology (Figure 2.2a) shows isolated deposits of diatomite, that may affect the evaluation of the results. Hence, it is possible that local studies are required in zone IV-B to properly assess site amplification susceptibility.

These areas were chosen based on the evaluation of geophysical data combined with geological background and boreholes to validate the acquired information and to complement the sites' description. The dynamic response of these zones can be further studied in terms of numerical simulations of the soil motion amplification. The following chapter will detail the procedures required for this analysis.

5.3.1. Comparison to A01-2014 earthquake

The latest earthquake that occurred in the north of Chile on April 1st 2014 (A01-2014) provided useful information regarding the site effects in the cities of interest. The current section uses the recorded ground motions of the A01-2014 event in Iquique to compare the observed and expected site amplification, in order to evaluate the consistency of the scientific rationale adopted.

The records and the peak ground accelerations are displayed in Figure 5.20, they show a good correlation with the expected effects from the microzoning (Figure 5.19). The records show a minimum PGA (0,26g) in bedrock, and the maximum PGA (0,6g) is registered where sedimentary deposits of moderate thickness was found, which indicate the effects of relatively soft soil layers on the ground amplification. In the case of Alto Hospicio area, the recorded acceleration has a PGA of 0.44g in agreement with the stiff soils detected in the present study.

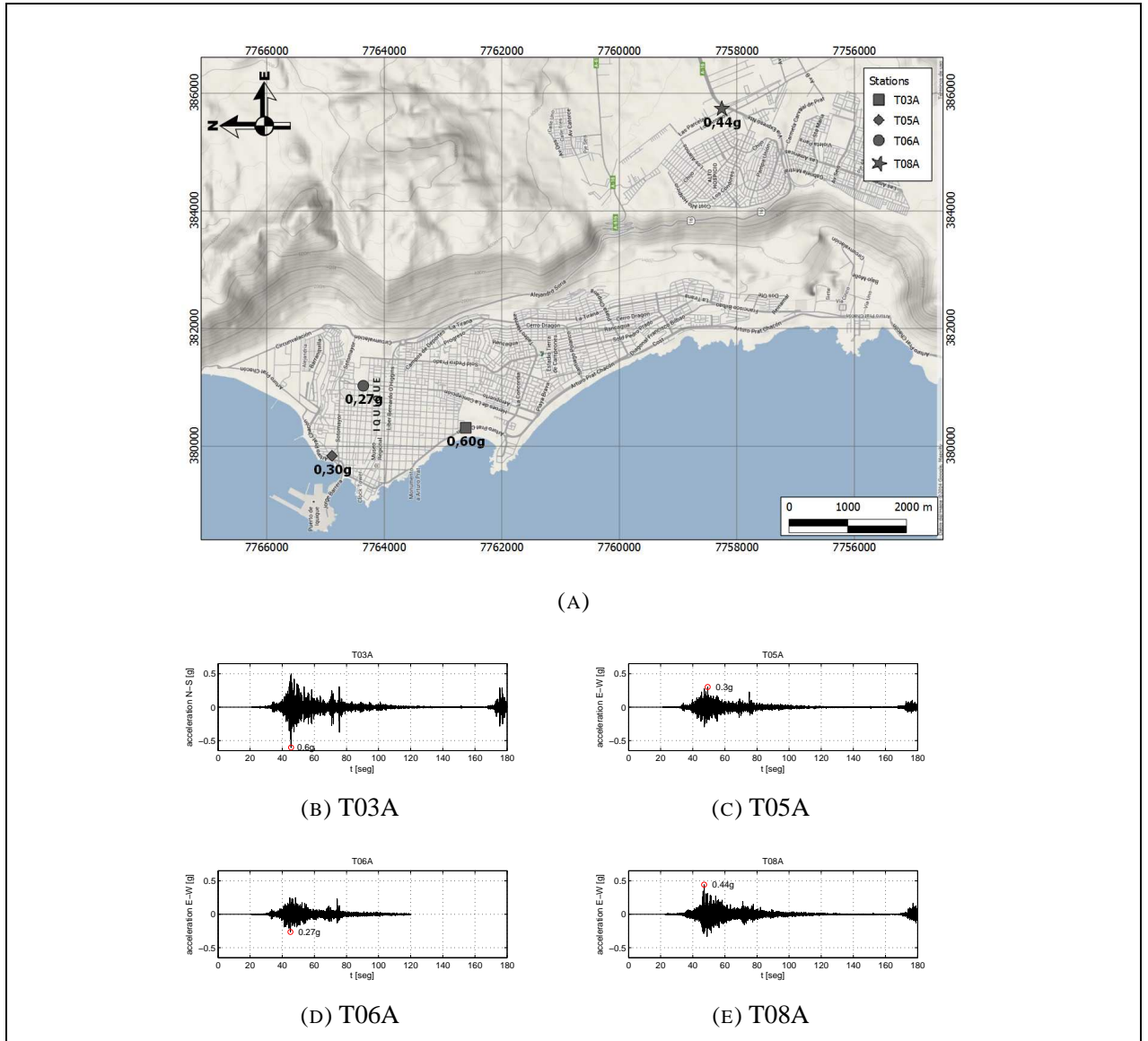


FIGURE 5.20: Acceleration records for the 01A-2014 Earthquake.

Furthermore, the acceleration spectra for each record was computed using a damping ratio of 5 %. The results for the stations located in bedrock are shown in Figure 5.21, where they are cross-checked with the closest HVSr result. It can be noted that the acceleration spectra has a considerably different peak for the N-S and E-W orientation. The T05A station is located at 1800 meters from the Coastal Range's escarpment. Therefore, this orientation differences could be explained through the reflected wavefield at the escarpment. However, this must be confirmed and further studies are required to confirm this hypothesis. It is also important to notice that the shape

of the acceleration spectras and the HVSR curve are quite similar (wide and with low amplitude), which is an important indicator of the presence of outcropping bedrock in this area.

On the other hand, Figure 5.22 compares the acceleration spectra for the stations located on

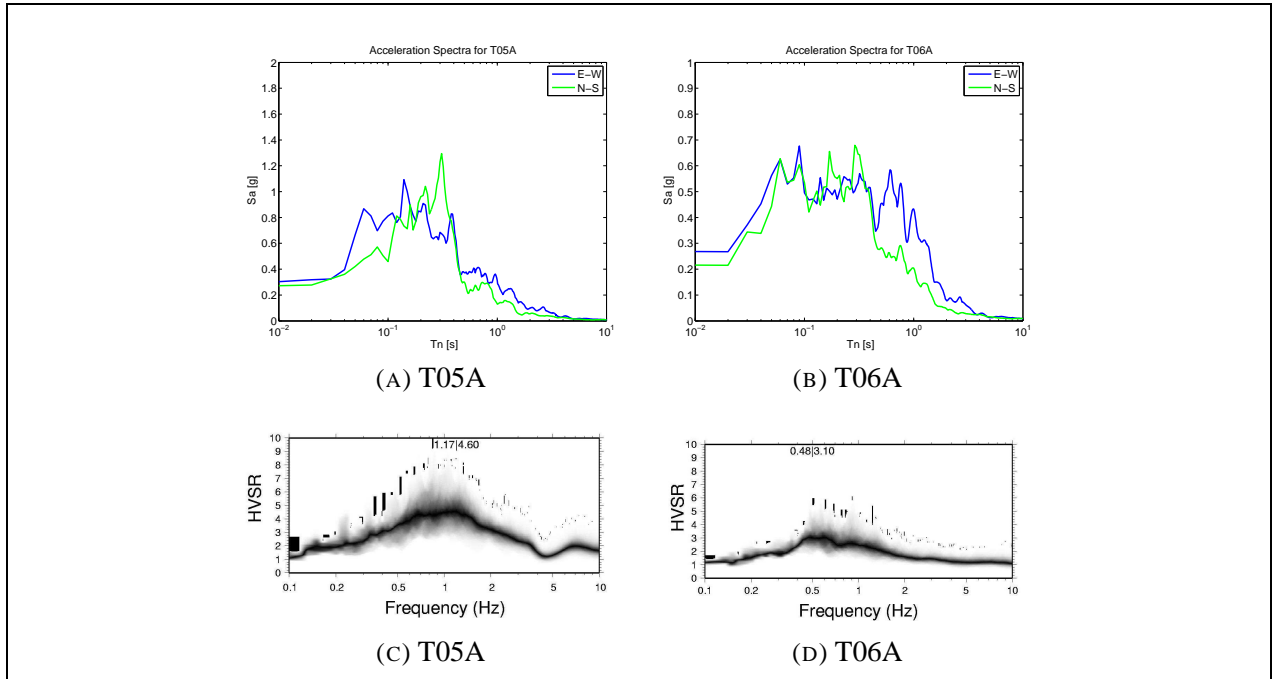


FIGURE 5.21: Acceleration spectra in stations T05A and T06A for the 01A-2014 Earthquake.

soil. Station T03A (Figure 5.22a) is located in a relative thin layer of sediments (of about 5 to 10 meters) (Figure 5.13). In this case, the peak period of the spectra is slightly higher than the predominant period obtained from a closely located HVSR measurement (about 100 meters), this could be explained through the non-linearity of the soil behaviour, that once the material stress overpasses its elastic limit, the stiffness is reduced, moderately raising its fundamental period. Of course, a HVSR measurement exactly at the same place must be performed to validate this hypothesis, because the variation on the predominant period could be also related to a local difference on the thickness of the sediments.

Nonetheless, the predominant period is not visible in station T08A (Figure 5.22b), where the results from the acceleration spectra are considerably different with respect to the HVSR data. Since Alto Hospicio is characterized by very rigid soils (Figure 5.17), it is fair to think that they behave almost as outcropping bedrock, so the recorded spectra is reasonable. Note, however, that

this case does not have any differences in the orientations of the spectra, which suggests the consistency of the hypothesis regarding topographic effects in station T05A.

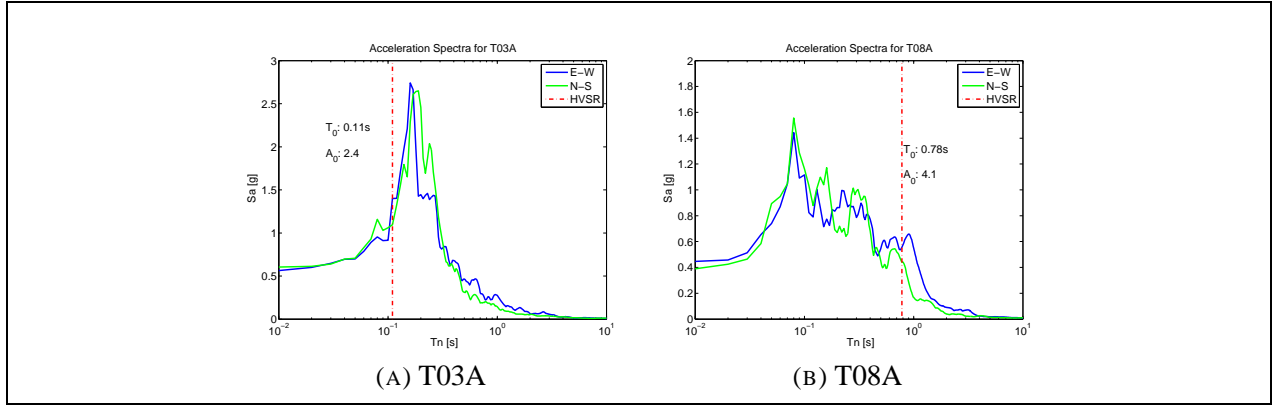


FIGURE 5.22: Acceleration spectra in stations T03A and T08A for the 01A-2014 Earthquake. The text on the Figures denote the HVSR results for the closest site.

5.4. Discussion

The earthquake response in the different stations in Iquique were in good agreement with the expected local amplification obtained from the microzoning. Unfortunately, no stations in Arica were able to record the ground motion.

It can be observed that the seismic microzoning provides a qualitative level of the site effects in the different areas of each city. However, it is not yet possible to associate this propensity to an accurate index of amplification. Based on this seismic microzoning, a need arises to transform this information into an accurate approximation of the ground amplification given an earthquake. The following section intends to transform the data provided from the microzoning into a model that could estimate the level of site effects observed, in terms of displacement or acceleration, for instance.

6. 3D MODELLING OF SITE AMPLIFICATION. THE CASE OF ARICA

The previous microzoning chapter provided useful information regarding the susceptibility to site effects in different zones of Arica and Iquique. However, this assessment is performed only at a qualitative level. It is important to transform this information into a quantitative evaluation that may provide results that are comparable with the acquired data from the 01A-2014 Pisagua earthquake. This chapter intends to guide this research into a numerical evaluation of the site effects in each city. In order to do this, a zone of interest is selected based on the site effect susceptibility and the topographic conditions that may affect the information.

Among the four zones identified where site effects are significant, the north of Arica emerges as a zone with high-density information and where the V_s^{30} indicates relatively low velocities. Furthermore, significant changes in the topography or steep escarpments are relatively absent around this area. The combination of the shear wave velocity profile and the HVSR technique gives an indicator of the depth to bedrock through the equation 3.5, which suggests that this depth ranges between 65 and 105 meters. This turns Arica into an area of interest, because of the thick layer of sediments over bedrock.

To further characterize the behaviour of this zone, numerical simulation is used to determine the level of amplification that will be registered at the surface. Given the spatial variability of the data available in the area, a 3D wave propagation model is explored in order to compare the response of the zone with a standard 1D model. Such simulations will be performed by means of the spectral element method (SEM), that has shown to be reliable in solving three-dimensional wave propagation problems in heterogeneous media (Mazzieri et al., 2013, Komatitsch et al., 1999).

6.1. Introduction to Spectral element method

The spectral element method (SEM) was first introduced by Patera (1984) in fluid dynamics, and since then it has gained interest for 2D and 3D seismic wave propagation (Komatitsch et al., 1999). The main feature of this method is the use of high-order Lagrange interpolants in the functions of the elements, so it is able to provide an arbitrary increase in accuracy by simply enhancing the algebraic degree of these functions, the so-called spectral degree (Scandella, 2007).

6.1.1. Model problem

The scope of this method is to determine the displacement field generated by a dynamic source (i.e. a seismic incident field) in a finite earth volume Ω . This volume, as shown in Figure 6.1, is composed by three main boundaries, assuming that there are no prescribed displacements: a free surface Γ_{ff} , which is stress-free, and the side and bottom boundaries, Γ_N and Γ_{NR} respectively, hence, $\Gamma = \Gamma_{ff} \cup \Gamma_N \cup \Gamma_{NR}$. The latter has a suitable and non-reflecting absorbing boundary condition that shall be described in the following discussions.

Let \underline{v} be the displacement field produced by an earthquake, which is governed by the momentum

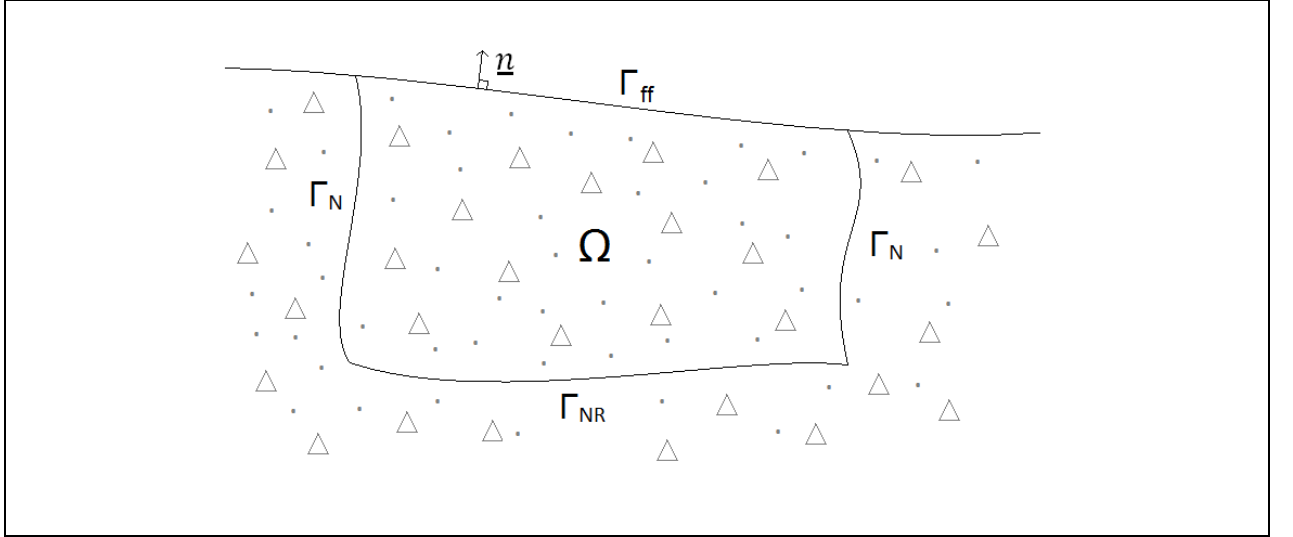


FIGURE 6.1: Finite soil model with total volume Ω . The free surface is denoted by Γ_{ff} , and the boundaries are Γ_D and Γ_{NR} . The unit outward normal to all boundaries is denoted by \underline{n} .

equation,

$$\rho \underline{v}_{tt} - \nabla \cdot \underline{\sigma}(v) = \underline{f} \quad (6.1)$$

where ρ is the density of the material, the t under-script stands for time derivative, and $\underline{\sigma}(v)$ is the Cauchy stress tensor for elastic behaviour,

$$\underline{\sigma}(v) := \lambda(\underline{\nabla v})\underline{I} + 2\mu\epsilon(v) \quad (6.2)$$

where $\underline{\underline{\epsilon}}(v) := \frac{1}{2}(\underline{\underline{\nabla}}v + \underline{\underline{\nabla}}v^T)$ is the strain tensor, λ, μ are the Lamé coefficients and $\underline{\underline{I}}$ is the identity second order tensor. To the equation 6.1, boundary conditions must be added.

$$\underline{\underline{\sigma}} \cdot \underline{n} = 0 \quad \text{on} \quad \Gamma_{ff}, \quad \underline{\underline{\sigma}}(v) \cdot \underline{n} = \underline{p} \quad \text{on} \quad \Gamma_N \cup \Gamma_{NR} \quad (6.3)$$

where \underline{n} is the unit normal vector to Γ and $\underline{p} := \underline{p}^*$ on Γ_N , while \underline{p}^* is defined as

$$\underline{p}^* := \rho(V_P - V_S)(\underline{v}_t \cdot \underline{n})\underline{n} + \rho V_S \underline{v}_t \quad \text{on} \quad \Gamma_{NR} \quad (6.4)$$

V_P and V_S are the propagation velocities of P and S waves, respectively. Note that at the boundary Γ_{NR} , a suitable absorbing condition must be able to propagate any incident wave without reflection. The approach of this investigation is the one implemented in SPEED code based on Stacey (1988), in which waves are perfectly absorbed when the incident waves reach the boundary in a perpendicular direction, but it is less effective when the wave is parallel to the boundary. For visco-elastic media, a modification of the equation of motion 6.1 may be introduced, adding a term in the form of a volume force \underline{f}^{visc} , characterized by a decay factor $\xi[s^{-1}]$,

$$\underline{f}^{visc} = -2\rho\xi\underline{v}_t - \rho\xi^2\underline{v} \quad (6.5)$$

adding this term to the equation 6.1, the following equation of motion is obtained

$$\rho\underline{v}_{tt} - \underline{\underline{\nabla}} \cdot \underline{\underline{\sigma}}(v) = \underline{f} + \underline{f}^{visc} \quad (6.6)$$

By adding these terms, it can be shown that all frequency components are equally attenuated (Mazzieri et al., 2013). This attenuation can be expressed with a quality factor

$$Q = Q_0 \frac{F}{\bar{F}_0} \quad (6.7)$$

where $Q_0 = \pi \frac{\bar{F}_0}{\xi}$, with \bar{F}_0 being a value representative of the frequency range to be propagated.

6.1.2. Weak form

One of the main features of the SEM is the fact that it is based on a weak formulation of the equations of motion, which has the advantage that it handles naturally free boundary conditions and interface discontinuities (Antonietti et al., 2012). Through the principle of virtual work, the

formulation consists in multiplying the equation 6.5 by an arbitrary test function \underline{w} , integrating by parts over the volume Ω and imposing the stress free boundary condition 6.3 on Γ_{ff} , which results in the following equation

$$\frac{\partial^2}{\partial t^2}(\rho \underline{v}, \underline{w})_{\Omega} + \underline{A}(\underline{v}, \underline{w})_{\Omega} = \underline{L}(\underline{w}) \quad (6.8)$$

with \underline{A} the bilinear form

$$\underline{A}(\underline{v}, \underline{w}) = (\sigma(\underline{v}), \epsilon(\underline{w}))_{\Omega} \quad (6.9)$$

and $\underline{L}(\underline{w})$ is referred to the boundary conditions and external forces

$$\underline{L}(\underline{w}) = (\underline{p}, \underline{w})_{\Gamma_N} + (\underline{p}^*, \underline{w})_{\Gamma_{NR}} + (\underline{f}, \underline{w})_{\Omega} + (\underline{f}^{visc}, \underline{w})_{\Omega} \quad (6.10)$$

Rewriting the previous version of the weak formulation by component N:

$$\forall t \in (0, T), \text{ find } v_N = v_N(x, t) \in V_N^{0d}, d = 1 \dots 3$$

$$\frac{\partial^2}{\partial t^2} \int_{\Omega} \rho v_N w_N d\Omega + \int_{\Omega} \sigma_{ij} v_N \epsilon_{ij} w_N d\Omega = \int_{\Gamma_N} p_N \cdot w_N d\Gamma + \int_{\Gamma_{NR}} p_N^* \cdot w_N d\Gamma + \int_{\Omega} f_N w_N d\Omega + \int_{\Omega} f_N^{visc} w_N d\Omega$$

Additional details regarding these expressions may be found in any classical book of finite element method (e.g. Zienkiewicz 1977).

6.1.3. Definition of the mesh

One of the characteristics of the SEM is the use of hexahedral elements for 3-D models and quadrangles for the surfaces in 3D and for solids in the two-dimensional case (Komatitsch et al., 1999).

The approach to the construction of the mesh goes as follows. In the first place, as in classical finite element procedures, the model volume Ω is partitioned into K number of non-overlapping regions Ω_k such that $\Omega = \cup_{k=1}^K \Omega_k$, each with its corresponding boundary Γ_k . Since the SEM in 3D works with hexahedral elements, the boundaries are divided in terms of quadrilateral surface elements.

In a second level, each element Ω_k is mapped into a reference element Ω_{ref} , corresponding to the square $[-1, 1]^2$ in 2D and the cube $[-1, 1]^3$ in 3D. Hence, there exists a suitable invertible mapping $F_k^j : \Omega_{ref} \rightarrow \Omega_k^j$ with a nonzero Jacobian J_k^j . This is then used to evaluate the integrals and derivatives of equation 6.11. The shape functions of the reference elements $N_a(\xi, \eta, \varsigma)$ are

products of Lagrange polynomials of degrees 1 or 2. The $n_l + 1$ Lagrange polynomials of degrees n_l are defined in terms of $n_l + 1$ control points $-1 \neq \xi_\alpha \neq 1, \alpha = 0, \dots, n_l$, by

$$l_\alpha^{n_l}(\xi) = \frac{(\xi - \xi_0) \dots (\xi - \xi_{\alpha-1})(\xi - \xi_{\alpha+1}) \dots (\xi - \xi_{n_l})}{(\xi_\alpha - \xi_0) \dots (\xi_\alpha - \xi_{\alpha-1})(\xi_\alpha - \xi_{\alpha+1}) \dots (\xi_\alpha - \xi_{n_l})} \quad (6.11)$$

In this formulation, hexahedral elements have up to 27 control points, while the quadrangles may have up to 8 or 9 control points, resulting in triple products of 1st degree Lagrange polynomials for the 8 control point quadrangles, and triple products of 2nd degree Lagrange polynomials for the hexahedra with 27 control points.

In the SEM, the control points $\xi_\alpha, \alpha = 1..n_l$ in equation 6.11 are the so-called Gauss-Lobatto-Legendre (LGL) points, which are the roots of

$$(1 - \xi^2)P'_{n_l}(\xi) = 0 \quad (6.12)$$

where P'_{n_l} is the derivative of the Legendre polynomial of degree n_l . These points can be computed by numerical integration of 6.12. To illustrate this approximation, Figure 6.2 shows the control points of a 2-D and 3-D elements and Figure 6.3 shows a Lagrange interpolant of degrees $N = 2$ and $N = 8$ at the LGL points on the reference element $[-1, 1]^2$.

In summary, the model is subdivided in a set of hexahedral elements. In each, the shape functions are sampled at the LGL points of integrations. Edges or vertexes of an element are shared among adjacent elements, so a need raises to ensure the continuity of the displacements across the common boundaries between the elements, in other words, one needs to define a mapping of gridpoints between the local mesh and global mesh.

6.1.4. Time integration scheme

The differential equation that governs the global system can be written as

$$[M] \{\ddot{U}\} + [A] \{U\} = \{F\} \quad (6.13)$$

where $[M]$ is the global mass matrix, $\{U(t)\}$ is the vector of nodal acceleration, $[A]$ is a matrix associated to the stiffness matrix and the absorbing boundary conditions, $\{U(t)\}$ is the vector of

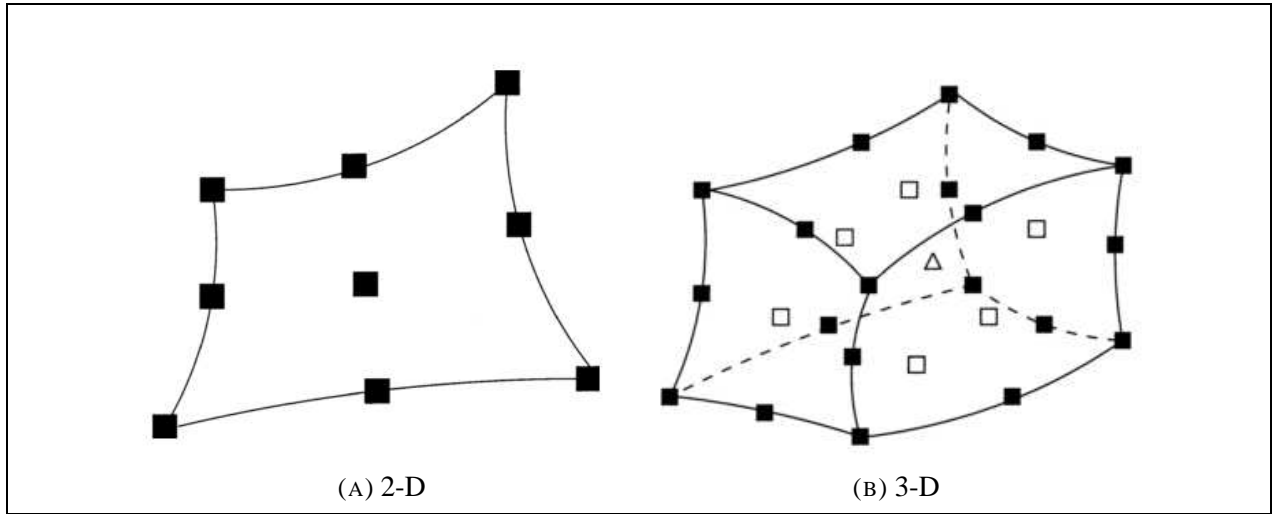


FIGURE 6.2: Control nodes for one element for a polynomial degree of 3. (a) shows the 2-D case with 9 control points while the 3-D element (b) has a total of 27 control points, the empty squares indicate the nodes that locate at the middle sides of the element's faces and the empty triangle lies at the center of the element (Komatitsch et al., 1999).

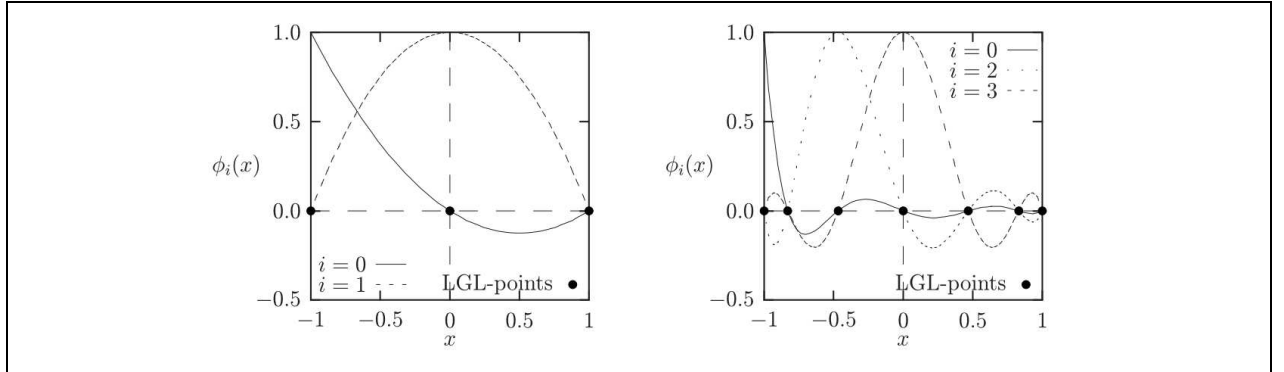


FIGURE 6.3: Lagrange interpolants through the LGL control points for $N = 2$ (left) and $N = 6$ (right). All Lagrange polynomials are equal to 1 or 0 at each point (Van de Vosse and Minev, 1996).

nodal displacements and $\{F\}$ is the vector created by the contribution of the external forces, tractions and non-reflecting boundary conditions.

Due to the use of Lagrange interpolants with LGL control points and the assumptions done through the formulation, the mass matrix M turns out into a diagonal global mass matrix (Komatitsch et al., 1999), which reduces significantly the computational cost of the problem. Equation

6.13 can also be written as:

$$\begin{bmatrix} M_1 & 0 & 0 \\ 0 & M_2 & 0 \\ 0 & 0 & M_3 \end{bmatrix} \begin{Bmatrix} \ddot{U}_1 \\ \ddot{U}_2 \\ \ddot{U}_3 \end{Bmatrix} + \begin{bmatrix} A_{11} & A_{12} & A_{13} \\ A_{21} & A_{22} & A_{23} \\ A_{31} & A_{32} & A_{33} \end{bmatrix} \begin{Bmatrix} U_1 \\ U_2 \\ U_3 \end{Bmatrix} = \begin{Bmatrix} F_1 \\ F_2 \\ F_3 \end{Bmatrix} \quad (6.14)$$

To solve equation 6.14, a classical Newmark scheme is used, since it is based upon a explicit second-order finite-difference scheme, it takes advantage of having a diagonal global mass matrix (Komatitsch and Tromp, 2002). To proceed with this scheme, the stiffness and boundary terms are moved to the right-hand side.

Initial conditions must be prescribed, that is

$$\{U(0)\} = \{U_0\} \quad \text{and} \quad \{\dot{U}(0)\} = \{V_0\} \quad (6.15)$$

Now if the model is carried out in a time T , the interval $(0, T]$ is subdivided into n_t subintervals of amplitude $\Delta t = T/n_t$. The application of Newmark method leads to

$$\begin{aligned} [[M] + \Delta t^2 \beta [A]] \{U(t_n + 1)\} &= \left[2[M] - \Delta t^2 \left(\frac{1}{2} - 2\beta + \gamma \right) [A] \right] \{U(t_n)\} \\ &\quad - \left[[M] + \Delta t^2 \left(\frac{1}{2} + \beta - \gamma \right) \right] \{U(t_{n-1})\} \\ &\quad + \Delta t^2 \left[\beta \{F(t_{n+1})\} \left(\frac{1}{2} - 2\beta + \gamma \right) \{F(t_n)\} \right. \\ &\quad \left. + \left(\frac{1}{2} + \beta - \gamma \right) \{F(t_{n-1})\} \right] \end{aligned} \quad (6.16)$$

where β and γ are the standard parameters of the Newmark method. To maintain the stability of the solution and taking advantage of the mass matrix, the values chosen for such parameters are $\beta = 0$ and $\gamma = \frac{1}{2}$. Replacing the values of the parameters in 6.16, the equation becomes:

$$[M] \{U(t_{n+1})\} = [2[M] - \Delta t^2 [A]] \{U\}(t_n) - [M] \{U\}(t_{n-1}) + \Delta t^2 \{F(t_n)\} \quad (6.17)$$

Note that once the initial conditions are known, the solution of 6.16 can be obtained provided that $\{U(t_n)\}$ and $\{U(t_{n-1})\}$ are known, for the initial step, this would look like

$$[M]\{U(t_1)\} = \left[[M] - \frac{\Delta t^2}{2}[A] \right] \{U_0\} - \Delta t[M]\{V_0\} + \frac{\Delta t^2}{2}\{F(t_0)\} \quad (6.18)$$

This scheme is also known as leap-frog (Mazzieri et al., 2013), and it will be stable as long as the time step satisfies the Courant-Friedrichs-Lewy (CFL) condition, governed by the minimum value of the ratio between the size of the grid cells and the P-wave velocity.

6.1.5. Recent approaches for non conforming domains

In the past years, different approaches for the spectral element method have been implemented in order to simulate the wave propagation problem more accurately. Among these, the Discontinuous Galerkin discretization emerges as a strategy to deal with non conforming domains, that is, a domain composed of different non-overlapping polygonal sub-domains. It was firstly introduced by Reed and Hill (1973) for the linear neutron transport equation, now-a-days it is applied in a wide range of disciplines and proven to be efficient to deal with complex seismic wave propagation problems (Mazzieri et al., 2011).

The idea behind a Discontinuous Galerkin Spectral Element Method (DGSEM) consists on replacing the exact continuity condition between the sub-domains into a weak one, writing the condition in terms of displacements and tensions across the interfaces. This formulation is not explored here, but it is very convenient to introduce, for instance, crustal fault activation or dynamic soil-structure interaction. It will be used in future stages of this investigation.

6.2. Description of zone of study

As mentioned earlier, the zone of study was selected based on the site-effects expectations after a joint analysis of geophysical and geological data. Based on this premise, an area of 1600x2000 meters in the north of Arica was selected for modelling (Figure 6.4). This zone was chosen because of the high-density geophysical information that had been gathered in the previous chapters and the availability of one borehole in the area. Furthermore, Monetta (2013) contributed with shear wave velocity profiles and predominant frequencies in 9 sites in the zone of interest, that have

shown to be consistent with the gathered data in the present study.

This domain is filled with eolian marine deposits (Figure 2.1) with an estimated thickness of

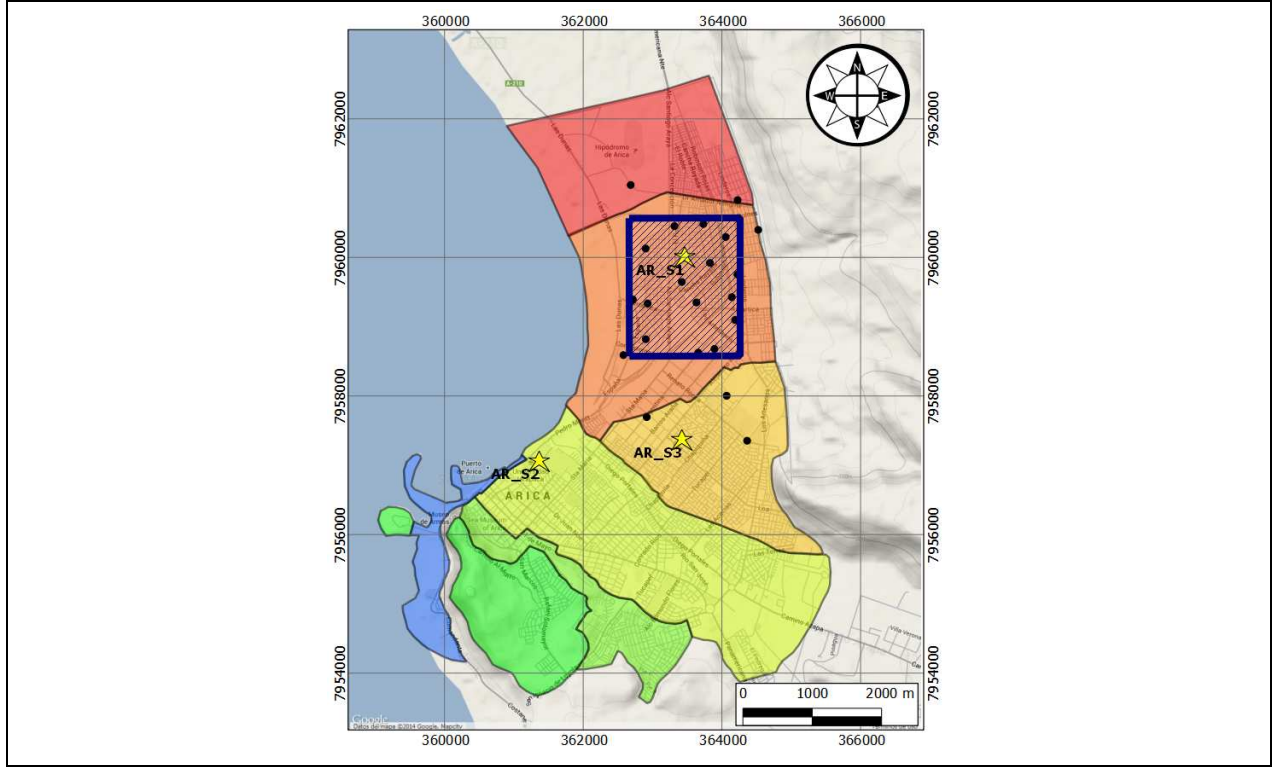


FIGURE 6.4: Selection of zone of study marked in blue. The sites where shear wave velocity profiles and predominant frequencies have been acquired are marked in black dots ("monitors"). The boreholes are displayed with yellow stars.

about 100 meters. It is characterized by relatively low shear wave velocities, the average V_s^{30} is $409 \pm 55 \text{ m/s}$ with a frequency range between 0.91 and 1.6 Hz (Figure 5.1). The V_s profiles show a thin layer (approximately 10 meters) of low V_s , following a deep layer of about 450 m/s.

The topography in the area was obtained based on a 90 meters resolution digital elevation model. It is fairly regular (Figure 6.5), increasing slightly towards the east, consequence of the Costal Range's escarpment that encompasses the city (Figure 2.2a).

Bedrock was not identified in any of the profiles. Consequently, constructing a submerged bedrock topography was made through Equation 3.5, by combining the average shear wave velocity and the predominant frequency obtained from HVSR. This was done for all the sites shown in Figure 6.4 and resulted into a surface that is shallower in the south-eastern part of the study site, that is, towards el Chuño hill (Figure 2.2a).

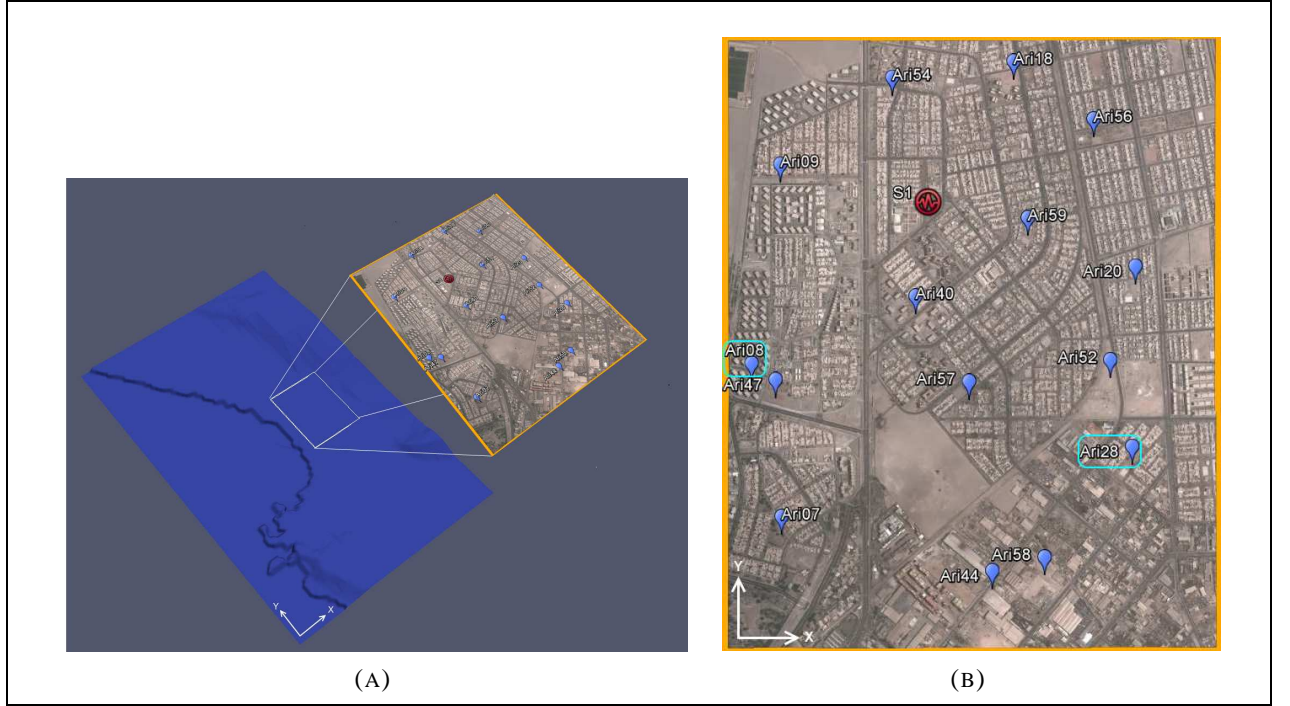


FIGURE 6.5: Topography of Arica and detail of study site.

Once the depth to bedrock was approximated through the HVSR technique, the shear wave velocity profiles were extended until given depth in each site. It is commonly known that for granular soils the shear wave velocity profile is proportional to the fourth root of the depth, that is

$$V_s(z) = k\sqrt[4]{z} \quad (6.19)$$

If V_s for $z = 30m$ is known, the parameter k can be calculated and the shear wave velocity profile extended, given that the fundamental frequency of the profile matches the predominant frequency obtained from the HVSR. This led to an iterative process for every control point, extending the shear wave velocity profile for each one until the estimated depth to bedrock, as shows Figure 6.4.

Once the 1D V_s profiles have been extended for all the control points, a 3D S-wave velocity model is derived through linear interpolation with a spatial resolution of 5 meters. For this procedure it is required to take into account the information outside the site of study, hence Figure 6.4 displays control points outside the limits of the zone of interest. The model contains a detailed

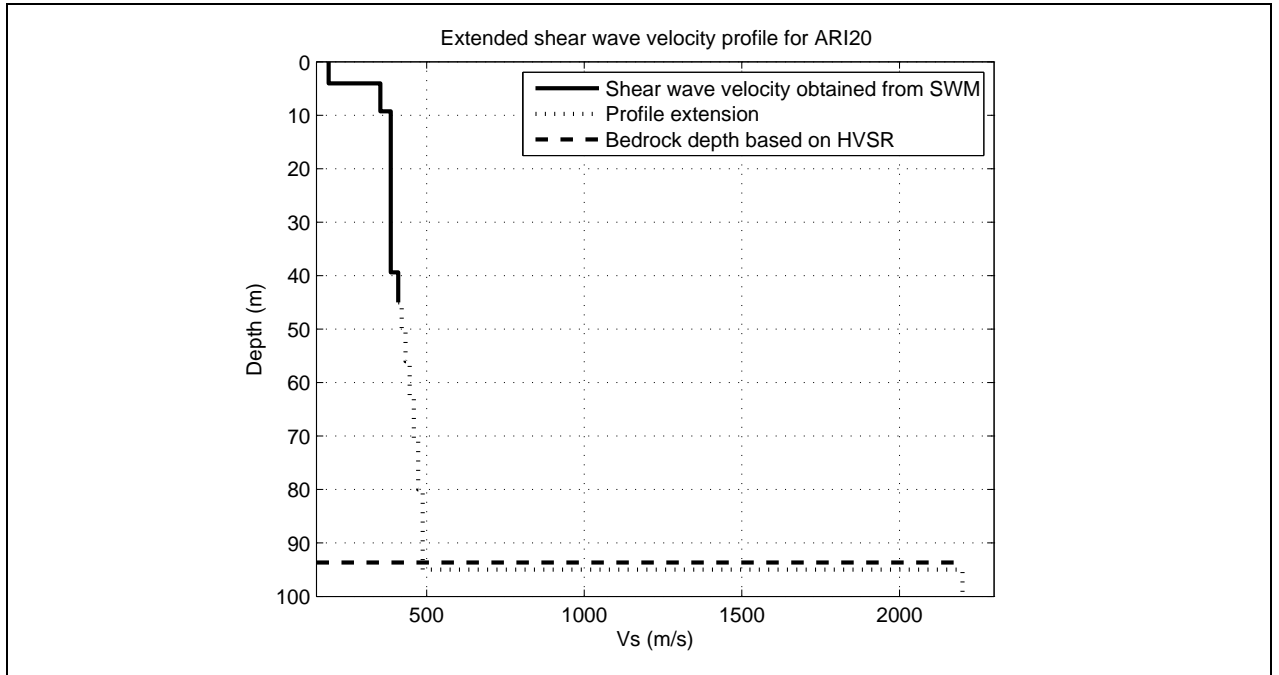


FIGURE 6.6: V_s profile for one site, the figure shows the extension of the profile until the estimated depth to bedrock.

description of the sediments shape defined by the contact between the sediment's shear wave velocity and the bedrock's velocity.

The final model may be seen in Figure 6.7. In this case, the contact between soil and bedrock was assumed stepped, for future meshing purposes. As it may be noted, the bedrock becomes more shallow towards the south-east, where El Chuño hill is located (Figure 2.2a), and shear wave velocities are fairly stable, with a first layer of about 200 m/s and a continuous increase up to 800 m/s towards the north of the model (Figure 6.4). Other elastic properties are derived from the V_s profiles and the USCS classification (Poisson's modulus). Using the estimations proposed by Kulhawy (1990) it was possible to approximate an average density of about $1800 \frac{kg}{m^3}$ for the deposits. With these parameters the other required values, such as V_p and the Lamé parameters, are obtained directly.

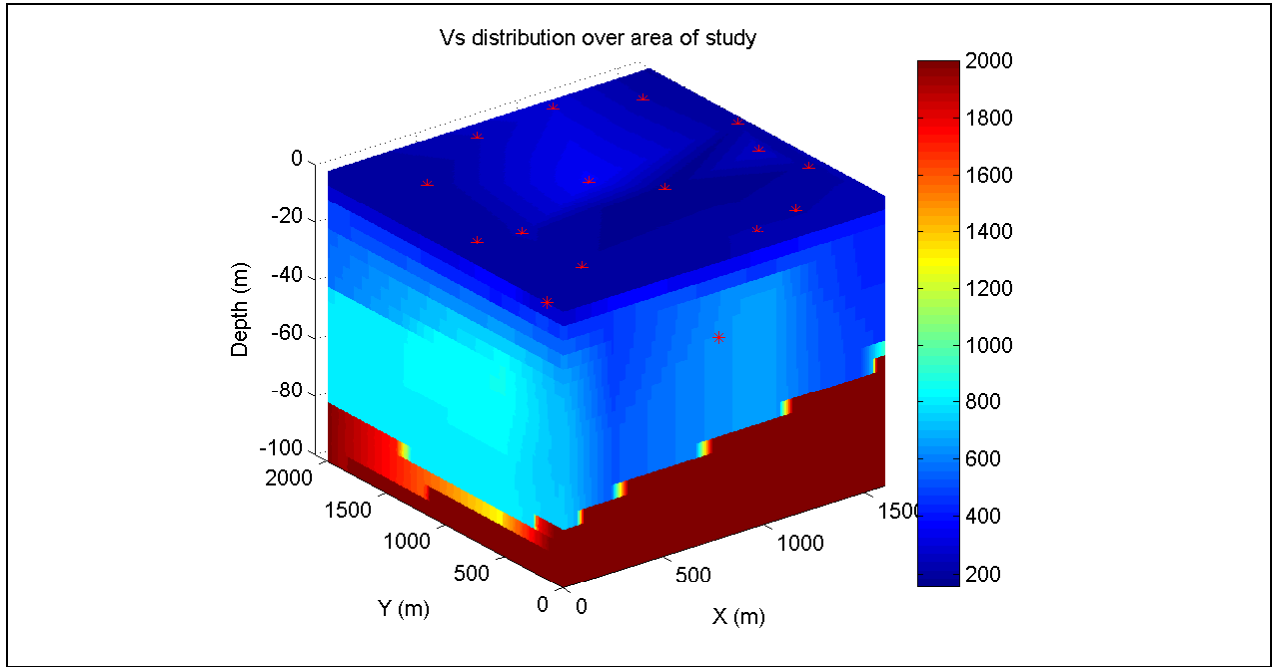


FIGURE 6.7: 3-D shear wave velocity model for the site of study in Figure 6.4.

6.3. Homogeneous soil mesh

The mesh is built using the software Trelis developed by Csimsoft[®], which incorporates a set of powerful and advanced meshing schemes, specifically for hexahedral unstructured meshing problems, such as algorithms of automatic refinement and handling of irregular surfaces.

The entire volume consists of a body with an extension based on the site study, that is, 1600x2000 meters. The depth of the model reaches 250 meters, relative to the sea level, so the total vertical extension ranges between 250 and 300 meters.

Based on the available geological and geophysical data, an acceptable trade-off was made between the spatially heterogeneous results from the in-field investigations (Figure 6.7) and the practical need to build a simplified mesh. Consequently, the volume was subdivided in three sub-horizontal layers, the first defined by the soil between the free surface and the bedrock contact. The second and third layer represent the basement submerged under the deposits. The initial elastic properties of each material are defined in Table 6.1. Note that second and third layers are differentiated because the source input will be induced in the bottom material.

The final mesh obtained is displayed in Figure 6.8. It consists of about 53.000 elements, the

TABLE 6.1: Elastic properties of each material. ρ denotes the density of the material, λ and μ are the Lamé parameters, and γ is the damping ratio.

Material	Subdomain	$\rho[\frac{kg}{m^3}]$	$\lambda[\frac{kgf}{m^2}]$	$\mu[\frac{kgf}{m^2}]$	$\gamma[\%]$
Soil	1	1800	$5.47E + 08$	$3.64E + 08$	1
Bedrock1	2	2500	$1.82E + 10$	$1.21E + 10$	1
Bedrock2	3	2500	$1.82E + 10$	$1.21E + 10$	0

grid size h for each element is related to the spectral degree p that will determine the amount of control points per element, hence, h is chosen such that the average number of points per minimum wavelength λ_{min} is about 5 (Komatitsch et al., 1999). Using a polynomial degree of 4, the size of the element ranges of about 5 meters (soil) up to 50 meters (bedrock). The mesh is designed to propagate frequencies of up to 15 Hz with $p = 4$, with a total of 3.500.000 spectral nodes.

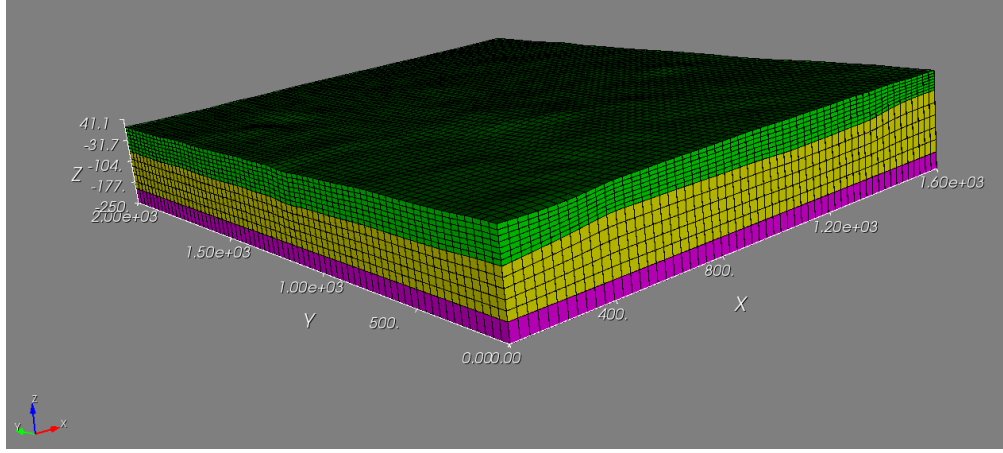
Finally, boundary conditions are imposed in all the faces defined in Equation 6.3. An absorbing boundary is imposed at the bottom of the mesh, while on the sides only Dirichlet boundary conditions are set. For a plane wave in X direction, the Dirichlet boundary conditions are imposed in the directions Y and Z ($v_y = v_z = 0$).

6.4. Source and Time scheme definition

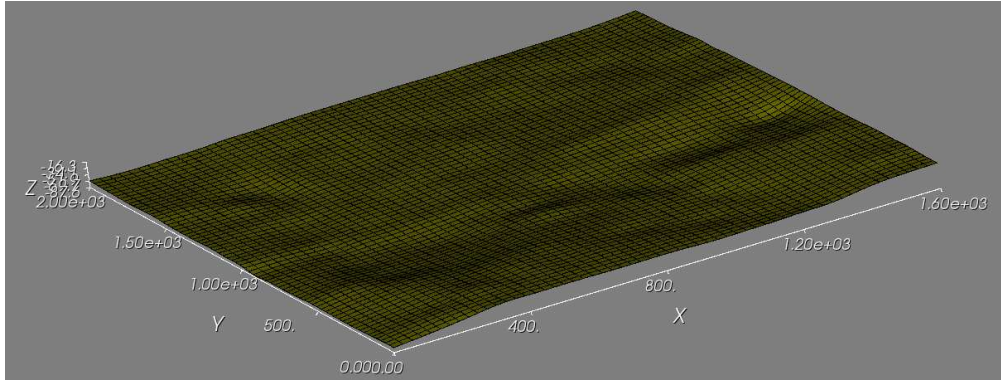
The numerical simulation was constructed based on a Ricker wavelet source of parameters $f_0 = 3.5Hz$ and $t_0 = 0.4s$, the waveform is depicted in Figure 6.9. This input was induced in material 4 of Table 6.1, assuming the input reaches the bottom at the same time. This assumption is reasonable given that the volume size is not large enough to detect significant arrival time differences for the source.

The SPEED code introduces a force time history able to generate a displacement time history with the Ricker wavelet shape, introducing an amplitude scale factor to adjust a target displacement, velocity or acceleration.

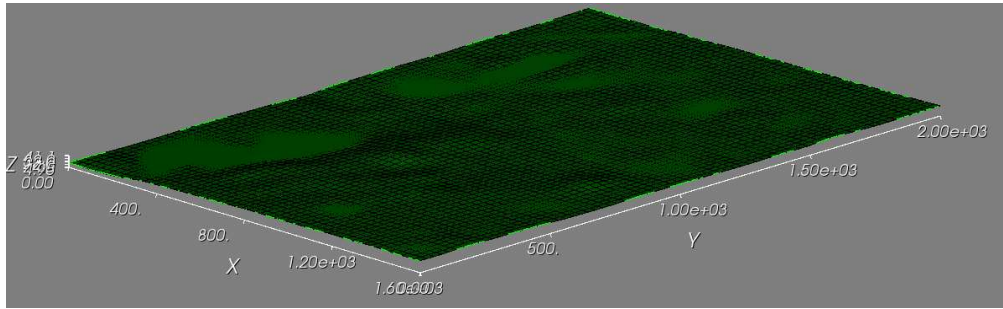
The time scheme used for the simulation is the one adopted in SPEED, based on a leap-frog



(A) Homogeneous soil Mesh



(B) Bedrock surface



(C) Topography surface

FIGURE 6.8: Homogeneous soil mesh for the proposed problem. Note that the North-South and East-West directions coincide with the axis Y and X, respectively.

method. The simulation runs for 3 seconds with a time step Δt that satisfies Courant-Friedrichs-Lewy (CFL) condition, given by

$$\Delta t \leq C_{CFL} \frac{\Delta x}{V_p} \quad (6.20)$$

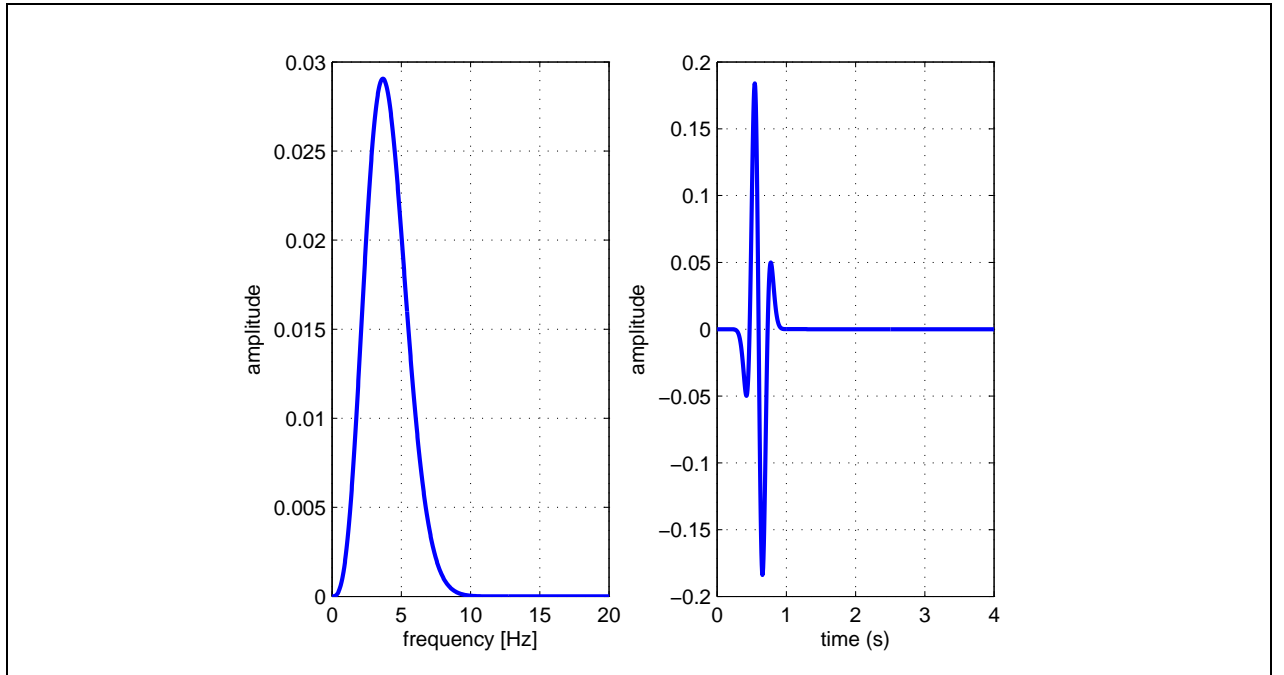


FIGURE 6.9: Ricker wavelet with $f_0 = 3.5\text{Hz}$ and $t_0 = 0.4\text{s}$.

where Δx is the shortest distance between two LGL nodes, C_{CFL} is a constant depending on the dimensions and V_p is the P-wave velocity of the material. For this simulation, a Δt of 0.1 msec was adopted, corresponding to 9.56 % of the critical time-step from Equation 6.20.

6.5. Results

The results of the simulation are recorded in the monitored points where empirical information of the shear wave velocity and predominant frequency has been acquired. The scope is to compare the observed motion using a standard 1D horizontally stratified model against 3D features.

6.6. Validation of the model

In order to validate the model, a 3D horizontally layered is modelled (layer cake model) and the transfer function is compared to an equivalent 1D profile of the soil. For the 3D simulation an average horizontal topography of 25 meters was assumed, plus an averaged bedrock level of -53 meters, meaning a layer of soil of 72 meters thick.

The computation of transfer functions for 3D and 1D may be seen in Figure 6.10 . It can be

noted that the first peak matches almost perfectly, whereas towards the upper modes the 1D function is slightly displaced because of the damping variations among the model. The 1D profile is analysed in time domain with DeepSoil code (Park and Hashash, 2004), that considers a concentrated external damping (damper between lumped masses representing soil layers) that is slightly different to the 1 % damping ratio considered in SPEED, so it is reasonable to see such slight variations on amplitudes and higher frequencies. The 1D model reaches a maximum frequency of 13 Hz while the 3D reaches 11 Hz, which makes the 3D simulation pretty accurate in the frequency range of interest.

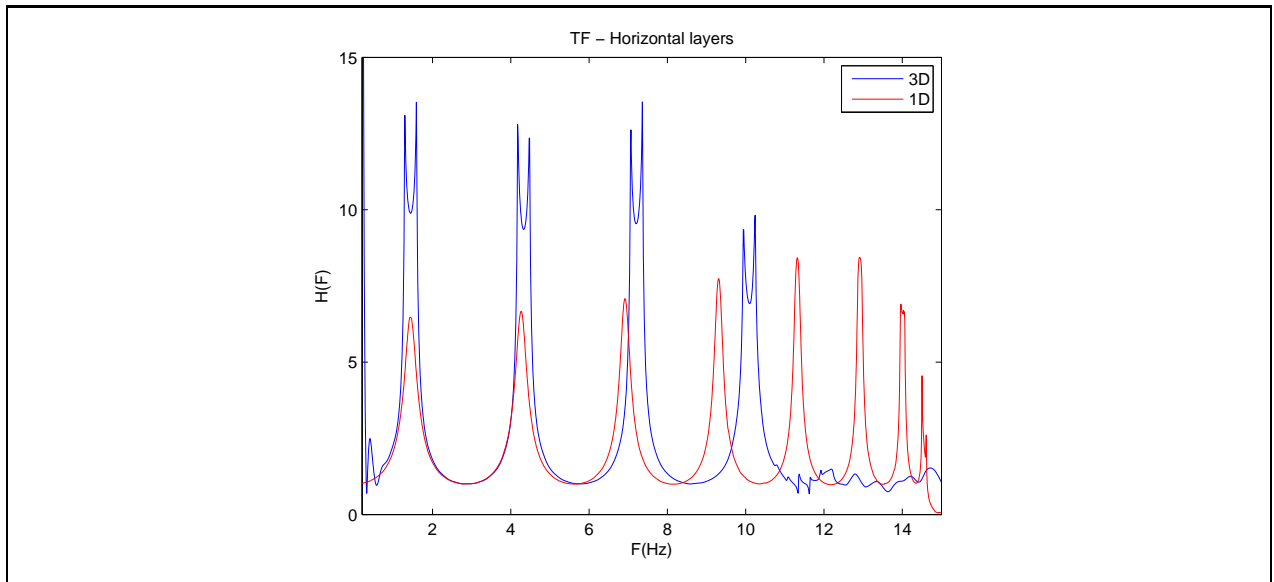


FIGURE 6.10: Comparison of transfer functions between a 3D horizontally layered model and an equivalent 1D profile computed in time domain.

6.7. Evaluation of 3D effects

The results from the simulation including the 3D effects of the topography and bedrock levels are shown in Figure 6.11. In terms of displacements, the maximum recorded displacement in the X direction was 30 centimeters, with a maximum strain of 3 % in the surface. This is relatively high given the assumption of linear behaviour. However, the proportion of the displacement between the bedrock level and the surface is consistent to the 1D case. The displacements in the Y and Z directions are caused by the adopted Poisson's coefficient.

Additionally, the comparison between the 3D and 1D transfer functions have shown some

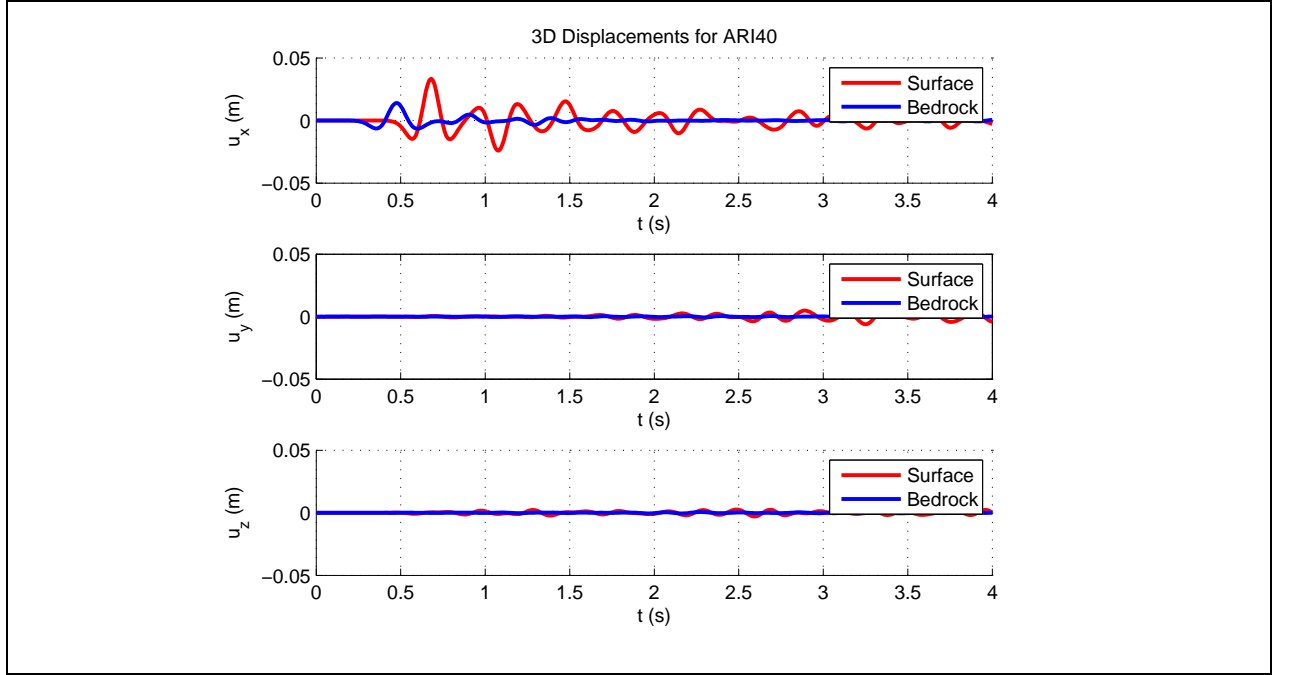


FIGURE 6.11: Comparison between displacements for ARI40 control point (Figure 6.5) between surface and bedrock.

variations towards the west side of the study zone (A08), whereas they are quite similar towards the east (A28). This could be related to the relative larger size of the elements towards the western zone, that reduces the resolution of the propagation. Indeed, as the vertical number of elements in soil layers is fixed, thinner soil layers are relatively more refined than thicker ones. This limitation is due to the computational cost of refining the mesh or increasing the polynomial degree of the elements function around the A08 control point. As this point is closely located to the boundary where Dirichlet conditions were imposed, possibly spurious waves reflections may take place, affecting the clearness of the results.

On the other hand, the first peak of the transfer function (Figure 6.12) is consistent with the results of the HVSr technique (Figure 5.6, for ARI08 and ARI28 the predominant frequencies are 1.2 and 1.6 Hz respectively, whereas the first peak of the transfer functions in Figure 6.12 result in frequencies of 1.3 and 1.8 Hz. This frequency variation is consistent with the bedrock surface level in the different control points (Figure 6.8b).

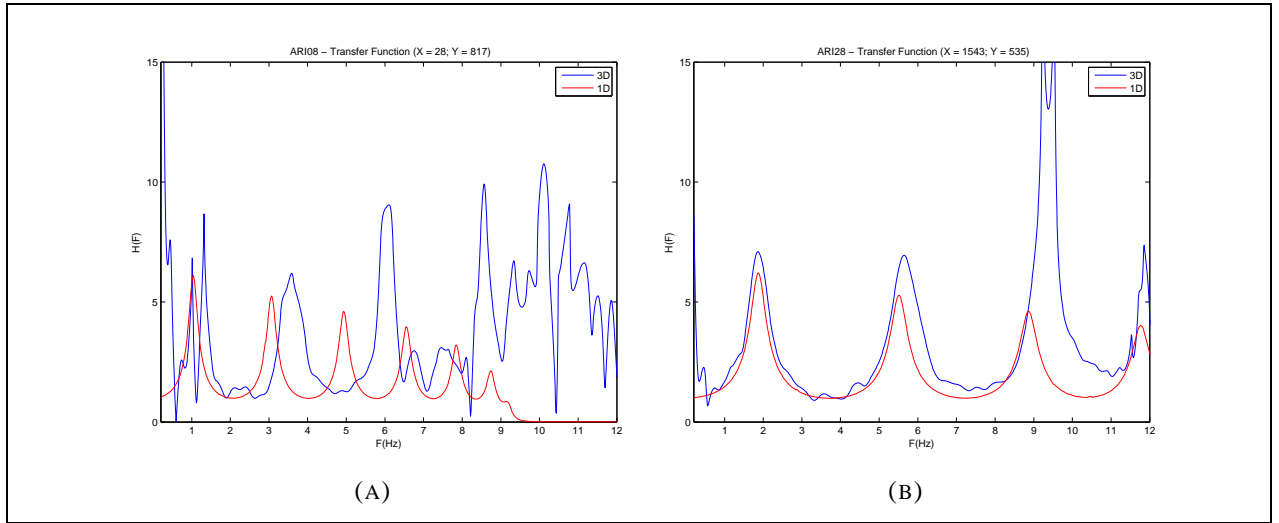


FIGURE 6.12: Transfer functions for 2 control sites using the 3D Homogeneous soil model. (a) ARI08 control point (west); (b) ARI28 control point (east).

The 3D model seems to accurately estimate the amplification levels considering an homogeneous soil model for a frequency range between 0.5 and 8 Hz, however, the resolution is reduced at higher frequencies, mainly due to the computational limitations and the use of idealised boundary conditions. As local irregularities of bedrock level and topography alters the idealised situation of a vertical and reflected SH wave field, spurious reflections, specially of surface waves, on mesh boundaries cannot be avoided. Future work will focus on including spatial heterogeneity of the soil properties, non-linearity of the soil's behaviour, and identification of the most appropriate strategy to treat boundaries for SH incoming waves, in order to accurately represent the ground motion amplification and compare it to the recorded motions from the A01-2014 earthquake.

7. CONCLUSIONS

The geophysical and geotechnical data acquisition and geological background of the north of Chile have provided information to properly characterize the dynamic response of the soils in the cities of Arica and Iquique. This data comprises the shear wave velocity profiles and predominant frequencies of 102 sites of interest. In addition, six boreholes were drilled to verify the reliability of the results. A seismic microzoning was proposed before the A01-2014 earthquake that provides an empirical observation of the ground motion amplification. Furthermore, a 3D wave propagation model simulated the motion in a zone in Arica where The results have shown the following:

1. The density of the surveys was sufficient in principle to generate a proper seismic microzoning of the soil along each area. A few exceptions may be noted when the topography of the site or possible bedrock level irregularities take a predominant role.
2. The areas in Iquique that are susceptible to site effects are; (1) the south of the city, along El Dragon hill, where a shallow layer of eolian deposits over a deep layer of sandy soil is identified; (2) to the north of the ZOFRI fault, where a marine deposit layer of approximately 15 meters deep was identified; and (3) the north of the port, consisting mainly of a thick layer of artificial landfill.
3. In the case of Arica, the main zone that is susceptible to site effects is the north of the city, where a deep layer of fine sand (over 35 meters) was located.
4. The characterized shear wave velocity profiles reached a maximum depth of 80 meters in the north of Arica, this is probably enough to properly assess the ground motion amplification susceptibility, but in most of cases the information was not enough to identify a reliable depth of bedrock in most of the city.
5. The acquired data during field work is consistent with the geological context of both cities.
6. A joint analysis between F_0 and V_{s30} is necessary to properly characterize the site response, in this study they have proven to be complementary and consistent between each other.
7. The peak ground accelerations registered for the A01-2014 Iquique earthquake agrees with the expected site effects from the proposed microzoning.

8. The use of 3D numerical simulations for amplification effects provides useful information regarding the effects of geometrical anomalies in the ground motion.
9. The comparison between the results from geophysical tests and boreholes have shown the reliability of using surface waves-based surveys. We recommend their use as they are reliable, low-cost and easy to implement.
10. Given the fact that the expected seismogenic energy accumulation of the Nazca-Southamerica plate coupling in the north of Chile was not entirely released by the A01-2014 earthquake, the microzoning approach and results obtained in this research have proven to be a valuable tool for preventive actions within northern Chile seismotectonic segment, still under high seismic risk.

7.1. Future work

The studies based on surface wave methods have shown consistency with the empirical evidence obtained in the cities of Arica and Iquique. However, it is recommended to perform local studies in the zones where the topography is irregular or where it is suspected to find complex 3D effects of the submerged bedrock, such as the center of Iquique, where the existing faults (Figure 2.2c) may have significant effects on the basement level. Additionally, it would be useful to combine the obtained data in the present research with gravimetry tests, in order to further characterize the magnitude of the sedimentary basin in Arica, and compare the depth to bedrock obtained from gravimetry data and from surface wave methods.

Regarding the wave propagation model, non-linearity of the materials is yet to be added, in order to evaluate more accurately the ground motion amplification in the zone of Arica. Furthermore, it would be appropriate to extend the model to the whole sedimentary basin, so a study of the motion effects can be carried out in the different zones delimited by the microzoning (Figure 5.9) and evaluate the potential effects that may come with the addition of bedrock from the escarpment of the surrounding hills.

Bibliography

- Aki, K. (1957). Space and Time Spectra of Stationary Stochastic Waves, with special Reference to Microtremors.
- Antonietti, P., Mazzieri, I., Quarteroni, A., and Rapetti, F. (2012). Non-conforming high order approximations of the elastodynamics equation. *Computer Methods in Applied Mechanics and Engineering*, 209212(0):212 – 238.
- Bard, P.-y., Duval, A.-m., Koehler, A., and Rao, S. (2004). Guidelines for the Implementation of the H / V Spectral Ratio Technique on Ambient Vibrations Measurements , Processing and Interpretation. 169(December):1–62.
- Bonnefoy-Claudet, S., Baize, S., Bonilla, L. F., Berge-Thierry, C., Pasten, C., Campos, J., Volant, P., and Verdugo, R. (2009). Site effect evaluation in the basin of Santiago de Chile using ambient noise measurements. *Geophysical Journal International*, 176(3):925–937.
- Chavez-Garcia, F. J. and Cuenca, J. (1998). Site effects and microzonation in acapulco. *Earthquake Spectra*, 14(1):75–93.
- Chávez-García, F. J., Rodríguez, M., and Stephenson, W. (2006). Subsoil structure using spac measurements along a line. *Bulletin of the Seismological Society of America*, 96(2):729–736.
- Chavez-Garcia, F. J.; Lermo, J. (1993). Site Evaluation using Spectral Ratios with only one station. 83(5):1574–1594.
- Chavez-Garcia, F. J.; Lermo, J. (1994). Are Microtremors Useful in Site Response Evaluation ? 84(5):1350–1364.
- Chlieh, M., Perfettini, H., Tavera, H., Avouac, J.-P., Remy, D., Nocquet, J.-M., Rolandone, F., Bondoux, F., Gabalda, G., and Bonvalot, S. (2011). Interseismic coupling and seismic potential along the central andes subduction zone. *Journal of Geophysical Research: Solid Earth (1978–2012)*, 116(B12).
- Comte, D. and Pardo, M. (1991). Reappraisal of great historical earthquakes in the northern chile and southern peru seismic gaps. *Natural Hazards*, 4(1):23–44.

- David, C. (2013). Tectonic and shallow seismic activity around the Arica Bend. Tesis para optar al grado de Doctor en Ciencias con mención Geología, Facultad de Ciencias Físicas y Matemáticas, Universidad de Chile, Santiago, Chile.
- Foti, S., Lancellotta, R., Sambuelli, L., and Socco, L. (2000). Notes on fk analysis of surface waves. *Annals of Geophysics*, 43(6).
- García, M., Gardeweg, M., Clavero, J., Hérail, G., and de Geología y Minería, S. N. (2004). Hoja arica, región de tarapacá. *Serv. Nac. de Geol. y Minería, Santiago, Chile*.
- Humire, F. (2013). Aplicacion de Metodos Geofisicos Basados en Ondas Superficiales para la Caracterización Sísmica de suelos. Aplicación a la microzonificación sísmica del Norte y Poniente de Santiago. Tesis para optar al grado de Magíster en Ciencias de la Ingeniería. Pontificia Universidad Católica de Chile.
- Kendrick, E., Bevis, M., Smalley Jr, R., Brooks, B., Vargas, R. B., Lauria, E., and Fortes, L. P. S. (2003). The nazca–south america euler vector and its rate of change. *Journal of South American Earth Sciences*, 16(2):125–131.
- Komatitsch, D. and Tromp, J. (2002). Spectral-element simulations of global seismic wave propagation-I. Validation. *Geophysical Journal International*, 149(2):390–412.
- Komatitsch, D., Tromp, J., and Sciences, P. (1999). Introduction to the spectral element method for three-dimensional seismic wave propagation. pages 806–822.
- Kulhawy, F. H. and Mayne, P. W. (1990). Manual on estimating soil properties for foundation design. Technical report, Electric Power Research Inst., Palo Alto, CA (USA); Cornell Univ., Ithaca, NY (USA). Geotechnical Engineering Group.
- Kvaerna, T. and Ringdahl, F. (1986). Stability of various fk estimation techniques. *Norsar semi-annual technical summary*, 1:1–86.
- Lacoss, R., Kelly, E., and Toksöz, M. (1969). Estimation of seismic noise structure using arrays. *Geophysics*, 34(1):21–38.
- Leyton, F., Sepúlveda, S., Astroza, M., Rebolledo, S., González, L., Ruiz, S., Fonca, C., Herrera, M., and Lavado, J. (2010). Zonificación sísmica de la cuenca de santiago, chile. In *Congreso Chileno de Sismología e Ingeniería Antisísmica, X Jornadas*, pages 22–27.

- Louie, J. N. (2001). Faster, better: shear-wave velocity to 100 meters depth from refraction microtremor arrays. *Bulletin of the Seismological Society of America*, 91(2):347–364.
- Maldonado, G. (2014). *Caracterización geológica de los suelos de fundación de la ciudad de Arica. XV región de Arica y Parinacota*. PhD thesis, Universidad Católica del Norte.
- Marquardt, C., Marinovic, N., and Muñoz, V. (2008). Geología de las ciudades de Iquique y Alto Hospicio, región de Tarapacá. *Carta Geológica de Chile, Serie Geología Básica*, 113:33.
- Mazzieri, I., Smerzini, C., Antonietti, P. F., Rapetti, F., Stupazzini, M., Paolucci, R., Quarteroni, A., and Ele, M. S. (2011). Non-conforming spectral approximations for the elastic wave equation in heterogeneous media. (May):1–17.
- Mazzieri, I., Stupazzini, M., Guidotti, R., and Smerzini, C. (2013). SPEED : SPectral Elements in Elastodynamics with Discontinuous Galerkin : a non-conforming approach for 3D multi-scale problems. (July):991–1010.
- Monetta, R. (2013). *Estudio de la microzonificación sísmica, de la ciudad de Arica. XV Región de Arica y Parinacota*. PhD thesis, Universidad Diego Portales.
- Nakamura, Y. (1989). A method for dynamic characteristics estimation of subsurface using microtremor on the ground surface. *Q.R. Rail. Tech*, (30):25–30.
- Ohrnberger, M., Wathélet, M., and Cornou, C. (2012). Using ambient vibrations techniques for site characterization.
- Okada, H. and Suto, K. (2003). *The microtremor survey method*, volume 12. Society of Exploration Geophysicists with the cooperation of Society of Exploration Geophysicists of Japan [and] Australian Society of Exploration Geophysicists.
- Park, C. B. and Miller, R. D. (2008). Roadside passive multichannel analysis of surface waves (masw). *Journal of Environmental & Engineering Geophysics*, 13(1):1–11.
- Park, C. B., Miller, R. D., and Xia, J. (1999). Multichannel analysis of surface waves. *Geophysics*, 64(3):800–808.
- Park, D. and Hashash, Y. M. (2004). Soil damping formulation in nonlinear time domain site response analysis. *Journal of Earthquake Engineering*, 8(2):249–274.
- Patera, A. T. (1984). A spectral element method for fluid dynamics: Laminar flow in a channel expansion. *Journal of Computational Physics*, 54(3):468 – 488.

- Pilz, M., Parolai, S., Picozzi, M., Wang, R., Leyton, F., Campos, J., and Zschau, J. (2010). Shear wave velocity model of the santiago de chile basin derived from ambient noise measurements: a comparison of proxies for seismic site conditions and amplification. *Geophysical Journal International*, 182(1):355–367.
- Podestá, L. (2013). *Microzonificación Sísmica de las ciudades de Iquique y Alto Hospicio, Región de Tarapacá*. PhD thesis, Universidad Diego Portales.
- Reed, W. H. and Hill, T. (1973). Triangular mesh methods for the neutron transport equation. *Los Alamos Report LA-UR-73-479*.
- Sauter, F. (1989). *Fundamentos de ingeniería sísmica*. Tecnología de Costa Rica.
- Scandella, L. (2007). Numerical evaluation of transient ground strains for the seismic response analysis of underground structures.
- Scholz, C. H. and Campos, J. (2012). The seismic coupling of subduction zones revisited. *Journal of Geophysical Research: Solid Earth (1978–2012)*, 117(B5).
- Scott, J. B., Rasmussen, T., Luke, B., Taylor, W. J., Wagoner, J., Smith, S. B., and Louie, J. N. (2006). Shallow shear velocity and seismic microzonation of the urban las vegas, nevada, basin. *Bulletin of the Seismological Society of America*, 96(3):1068–1077.
- Seed, H. B. and Idriss, I. M. (1969). *Influence of soil conditions on ground motions during earthquakes*. University of California, Institute of Transportation and Traffic Engineering, Soil Mechanics Laboratory.
- Stacey, R. (1988). Improved transparent boundary formulations for the elastic-wave equation. *Bulletin of the Seismological Society of America*, 78(6):2089–2097.
- Tokimatsu, K. (1997). Geotechnical site characterization using surface waves.
- Tuladhar, R., Yamazaki, F., Warnitchai, P., and Saita, J. (2004). Seismic microzonation of the greater bangkok area using microtremor observations. *Earthquake engineering & structural dynamics*, 33(2):211–225.
- Van de Vosse, F. and Mineev, P. (1996). Spectral elements methods: Theory and applications. Technical report, EUT Report 96-W-001 ISBN 90-236-0318-5, Eindhoven University of Technology.
- Wathelet, M. (2005a). Array recordings of ambient vibrations: surface-wave inversion. *Liège University (Belgium)*.

- Wathelet, M. (2005b). Geopsy geophysical signal database for noise array processing. *Software, LGIT, Grenoble, France*.
- Wathelet, M. (2008). An improved neighborhood algorithm: Parameter conditions and dynamic scaling. *Geophysical Research Letters*, 35(9):L09301.
- Zienkiewicz, O. C. (1977). *The finite element method / O. C. Zienkiewicz*. McGraw-Hill London ; New York, 3d expanded and rev. ed. edition.
- Zywicki, D. J. (1999). *Advanced Signal Processing Methods Applied to Engineering Analysis of Seismic Surface Waves*.

8. APPENDIX A

TABLE 8.1: Results of V_s^{30} and HVSR in Arica and their corresponding coordinates. The coordinate system is UTM WGS84.

Name	X	Y	V_s^{30}	F_0	A_0
AR001	360365	7956379	474	8,85	3,7
AR002	361946	7956897	436	0	0
AR003	362935	7957188	480	1,52	3,1
AR004	363211	7956427	575	1,3	5,55
AR005	363645	7957072	531	2,02	8,9
AR006	361956	7957450	417	1,97	2,9
AR007	362936	7958831	388	1,53	4,45
AR008	362714	7959388	381	1,2	4,5
AR009	362921	7960113	435	1,38	3,75
AR010	363286	7961935	403	1,53	6,65
AR011	361837	7956366	446	0	0
AR012	363022	7955338	332	0,92	5,75
AR013	364101	7956487	573	1,65	3
AR014	364202	7955234	500	1,1	2,7
AR015	364453	7955100	514	1,3	2,6
AR016	364389	7957325	469	2,4	3,65
AR017	364085	7957999	438	1,82	3,45
AR018	363772	7960490	429	1,22	3,2
AR019	363574	7957667	435	1,53	5,45
AR020	364221	7959750	396	1,42	7,55
AR021	363173	7954067	567	2,12	3,4
AR022	363143	7954778	482	0,83	4,05

TABLE 8.2: Results of V_s^{30} and HVSR in Arica and their corresponding coordinates. The coordinate system is UTM WGS84.

Name	X	Y	V_s^{30}	F_0	A_0
AR023	362470	7954787	951	0	0
AR024	361717	7955164	1150	1,83	9,2
AR025	362258	7955499	492	3,25	3,5
AR026	361069	7956833	423	1,3	4,15
AR027	362177	7956215	482	1,28	3
AR028	364214	7959097	326	1,6	3,5
AR029	363767	7961874	451	1,55	4,1
AR030	364133	7960951	446	1,3	2,4
AR031	361854	7954026	949	3,95	2,65
AR032	361354	7954450	1039	2,67	9,1
AR033	364847	7955775	571	1,47	4,3
AR034	365555	7954523	424	0	0
AR035	364031	7955654	558	1,3	3,8
AR036	361258	7955814	675	0	0
AR037	360866	7955983	373	3,72	3,8
AR038	363066	7955922	473	1,32	3,65
AR039	362921	7957680	422	1,52	3,65
AR040	363421	7959637	565	1,45	2,8
AR041	363206	7961109	389	1,07	2,35
AR042	362683	7961039	381	0	0
AR043	364554	7960410	371	0	0
AR044	363709	7958643	388	1,43	2,6
AR045	361432	7957126	349	1,38	2,9

TABLE 8.3: Results of V_s^{30} and HVSR in Iquique and their corresponding coordinates. The coordinate system is UTM WGS84.

Name	X	Y	V_s^{30}	F_0	A_0
IQUI001	381946	7765238	589	0	0
IQUI002	381863	7765441	635	3,25	2,85
IQUI003	380932	7765752	388	1,35	2,45
IQUI004	380548	7765071	671	0	0
IQUI005	379550	7764689	666	0,4	4,15
IQUI006	379952	7764222	1071	0	0
IQUI007	379783	7764029	761	0,22	2,49
IQUI008	379813	7763882	1015	0	0
IQUI009	380670	7764366	1088	1,77	3,05
IQUI010	381269	7764498	844	0,48	3,1
IQUI011	380710	7763086	978	0,48	4,9
IQUI012	380724	7762640	716	9,15	3,4
IQUI013	382395	7758478	481	4,08	2,9
IQUI014	382790	7759076	320	1,83	3,65
IQUI015	382281	7760715	424	2,53	2,6
IQUI016	381997	7760274	381	4,03	3,55
IQUI017	381316	7760516	814	2,05	5,2
IQUI018	382159	7760075	397	3,12	2,35
IQUI019	379879	7764682	1045	1,17	4,6
IQUI020	381730	7760079	389	4,37	5,7
IQUI021	381782	7761281	721	10,22	4,49
IQUI022	381741	7762121	543	9,17	3,15
IQUI023	382294	7757690	380	2,85	3,35
IQUI024	382425	7756604	437	3,22	2,45
IQUI025	381350	7762946	941	2,15	8,55
IQUI026	381261	7766362	487	3,4	7,35
IQUI027	381370	7766425	500	4,1	5,05
IQUI028	381311	7765892	469	3,03	2,15
IQUI029	381050	7764962	651	0,27	4
IQUI030	384951	7757155	866	0	0
IQUI031	384299	7757673	661	1,13	2,9

TABLE 8.4: Results of V_s^{30} and HVSR in Iquique and their corresponding coordinates. The coordinate system is UTM WGS84.

Name	X	Y	V_s^{30}	F_0	A_0
IQUI032	384606	7758576	701	1,45	3,5
IQUI033	385320	7757952	839	1,28	4,1
IQUI034	385522	7758683	652	0	0
IQUI035	382448	7756038	609	1,9	3,45
IQUI036	382811	7755552	672	1,7	2,4
IQUI037	381232	7761903	1136	0	0
IQUI038	381258	7761474	881	4,24	2,27
IQUI039	381831	7763169	890	3,46	4,26
IQUI040	380512	7763744	769	0	0
IQUI041	381198	7760997	1223	0,42	8,45
IQUI042	380331	7761888	1042	4,72	2,71
IQUI043	382264	7759164	383	3,32	4,2
IQUI044	381656	7762312	718	0	0
IQUI045	380923	7762324	1023	9,73	3,45
IQUI046	382256	7755387	564	5,15	10
IQUI047	382584	7757295	470	2,28	2,05
PORT1A	378975,12	7765686,68	305	2,58	8,71
PORT1B	378991,007	7765744,913	0	2,42	8,75
PORT1C	378950,636	7765690,396	0	2,46	10
PORT2	378575,92	7765033,92	1029	8,33	2,3
PORT3	378900,4	7764858,82	728	16,85	4,16
PORT4	378939,39	7764880,43	701	10,49	3,68
PORT5	379235,46	7764849,29	596	6,84	1,54
PORT6	378891,73	7765375,17	442	5,28	10
PORT7	378551,39	7765122,64	1050	2,87	2,8
PORT8A	378871,38	7765321,59	453	5,74	6,57
PORT8B	378844,027	7765245,802	0	9,79	5,3
PORT9	379312,13	7764914,84	505	0	0
PORT10	379019,18	7764955,87	724	16,7	3,13

9. APPENDIX B

The acquired data during fieldwork may be found in the attached memory stick.